UC Santa Barbara
UC Santa Barbara Electronic Theses and Dissertations

Title

Engineering Haptic Technologies for Interaction in Virtual and Augmented Reality

Permalink

https://escholarship.org/uc/item/6322f0b7

Author

Dandu, Bharat Chandrahas

Publication Date

2022

Peer reviewed|Thesis/dissertation

University of California
Santa Barbara

Engineering Haptic Technologies for Interaction in Virtual and Augmented Reality

A dissertation submitted in partial satisfaction
of the requirements for the degree

Doctor of Philosophy
in
Electrical and Computer Engineering

by

Bharat Chandrahas Dandu

Committee in charge:

Professor Yon Visell, Chair
Professor B.S. Manjunath
Professor Hua Lee
Professor Tobias Hollerer

March 2022

The Dissertation of Bharat Chandrahas Dandu is approved.

_____

Professor B.S. Manjunath

_____

Professor Hua Lee

_____

Professor Tobias Hollerer

_____

Professor Yon Visell, Committee Chair

January 2022

Engineering Haptic Technologies for Interaction in Virtual and Augmented Reality

To Amma and Nanna

Acknowledgements

First and foremost, I would like to thank my PhD advisor, Yon Visell, for the guidance and support he has given me over the course of my doctoral program. I have really appreciated working with him, and learning from his insights on framing and tackling research questions have truly made me the researcher I am today.

I would like to express my thanks to Profs. Tobias Hollerer, Hua Lee and B.S. Manjunath for serving on my doctoral committee, and providing valuable feedback during our discussions.

I am deeply grateful for the contributions of my collaborators who helped shape the various research projects presented within thesis : Yitian Shao, Irene Kuling, Niko Kastor, Shantonu Biswas, Gregory Reardon, Dustin Goetz and Vedad Bassari. I would also like to thank fellow lab members within the RE Touch Lab for their constant support : Mengjia Zhu, Anzu Kawazoe, Neeli Tummula, Stejara Dinulescu, Mare Hirsch, Taku Hachisu, Simone Fani, Adrien Ferstera, Harald Schafer, and Shrinivas Patwardhan. It has been an absolute pleasure working with these excellent researchers. I would like to thank Cesare Parise, who provided valuable guidance on the study of human psychophysics during the course of my internship. I would also like to thank all the faculty and teachers who've taught me throughout my education.

I would like to thank my close friends here in Santa Barbara; Bharath, Kruthika, Ravi, Akshar, and Manhar, you've helped keep me sane, and have made my stay here in Santa Barbara a memorable and happy time. I would also like to thank my aunt Padmaja Vutukury for her support and advice throughout the course of my graduate program.

Finally, I express my sincerest gratitude to my parents for all their unconditional love and support, without which I would not be where I am today.

Curriculum Vitæ
Bharat Chandrahas Dandu

Education

2022   **Ph.D.** in Electrical and Computer Engineering (Expected), University of California, Santa Barbara.
- *Research Topics:* Haptic Engineering, Perception, HCI, AR/VR

2016   **M.S.** in Electrical and Computer Engineering, University of California, Santa Barbara.
- *Major:* Communications, Control and Signal Processing

2015   **B.Tech** in Electrical Engineering, Indian Institute of Technology, Madras, India

Publications

Journal articles:-

1. S. Biswas*, **B. Dandu***, Y. Shao, D. Goetz, Y. Visell "Stretchable Optoelectronic Skin for Haptic Feedback via Light Fields", in preparation.

2. N. Kastor*, **B. Dandu***, V. Bassari, G. Reardon, Y. Visell, "A Fluidic Electromagnetic Actuator for High-Fidelity Haptic Feedback", submitted to Sensors and Actuators A: Physical.

3. G. Reardon, **B. Dandu**, Y. Shao, Y. Visell, "Shear Shock Waves Constrain Haptic Holography via Focused Ultrasound", submitted to Proceedings of the National Academy of Sciences.

4. **B. Dandu**, Y. Shao, Y. Visell, "Rendering Spatiotemporal Haptic Effects via the Physics of Waves in the Skin" **IEEE Transactions on Haptics**, 14.2 (2020): 347-358.

5. **B. Dandu**, I. Kuling, Y. Visell, "Proprioceptive Estimates of Finger Location Are Coarse, Biased, and Context-Sensitive" **IEEE Transactions on Haptics**, 13.2 (2019): 259-269.

Peer-reviewed conference papers:-

1. S. Dinulescu, N. Tummula, G. Reardon, **B. Dandu**, D. Goetz, S. Topp, Y. Visell,"A Smart Bracelet Supporting Tactile Communication and Interaction", Accepted for presentation at **IEEE Haptics Symposium, 2022**

2. **B. Dandu***, Y. Shao*, A. Stanley, Y. Visell, "Spatiotemporal Haptic Effects from a Single Actuator via Spectral Control of Cutaneous Wave Propagation", **Proc. IEEE World Haptics Conference, 2019**.

3. G. Reardon, Y. Shao, **B. Dandu**, W. Frier, B. Long, O. Georgiou, Y. Visell, "Cutaneous Wave Propagation Shapes Tactile Motion: Evidence from Air-Coupled Ultrasound", **Proc. IEEE World Haptics Conference, 2019**.

4. **B. Dandu**, I. Kuling, Y. Visell, "Where Are My Fingers? Assessing Multi-Digit Proprioceptive Localization." **Proc. IEEE Haptics Symposium, 2018**.

5. Sudha, N., and **D. Bharat Chandrahas**. "A pipelined memory-efficient architecture for face detection and tracking on a multicore environment." **VLSI Design and Test (VDAT), 2015 19th International Symposium on**. IEEE, 2015.

Patents

1. Keller, S.J., Trutna, T.T., Benko, H., King, R., Stanley, A.A., Di Luca, M., Shao, Y., **Dandu, B.**, Visell, Y., Methods, devices, and systems for creating localized haptic stimulations on a user. U.S. Patent Application 16/241,900, filed July 11, 2019.

2. Keller, S.J., Trutna, T.T., Benko, H., King, R. and Lou, Y., Shao, Y., **Dandu, B.**, Visell, Y., Methods, devices, and systems for creating haptic stimulations and tracking motion of a user. U.S. Patent Application 16/241,871, filed July 11, 2019.

Awards

1. **Best Paper Award**: 2020 IEEE Transactions on Haptics, presented at IEEE World Haptics Conference 2021.

2. Awarded the UC Santa Barbara ECE Dept. **Ph.D. Dissertation Fellowship**, 2021

3. **Best Technical Demonstration Award** at the IEEE World Haptics Conference 2019.

4. **Best Paper Award Finalist** at the IEEE World Haptics Conference 2019.

5. **Best Paper Award Nomination** at the IEEE Haptics Symposium 2018.

Research Intern, Facebook Reality Labs-Research, Audio team, July-Sept 2019

Abstract

Engineering Haptic Technologies for Interaction in Virtual and Augmented Reality

by

Bharat Chandrahas Dandu

A longstanding goal in engineering research has been to realize haptic displays for virtual reality that allow their users to touch and manipulate virtual objects which feel realistic. Despite decades of research, this goal remains far from being achieved. Motivated by the challenges involved, this PhD contributes new research findings on perceptual and physical mechanisms of human touch perception, and applies this knowledge for the engineering of efficient haptic technologies for virtual and augmented reality.

The first part of the PhD is motivated by the active nature of haptic perception. During haptic exploration of objects, proprioceptive information about movements of the hands and fingers is integrated with tactile sensory information elicited via touch contact in order to facilitate perceptual judgements about object properties or events. Surprisingly little is known about human abilities to spatially localize the fingers via proprioception. The first part of the dissertation presents findings from perceptual investigations using a novel virtual reality paradigm. The results reveal that errors in spatial localization of the fingers are surprisingly large, averaging several centimeters per finger, but are strongly refined by even partial visual cues about the positions of adjacent fingers. The results also provide critical information that is needed in order to specify performance requirements for virtual reality technologies, including hand tracking systems.

The next part of this PhD addresses another key aspect in engineering haptic interactions: that of furnishing touch sensations to the skin. A central challenge in haptic engineering is that the skin is an extended sensory medium with high spatial resolution. While many prior haptic

devices have been designed to use numerous actuators, such devices are too bulky, costly, and complex for practical application. This PhD proposes a new design strategy that exploits the physics of waves in the skin. First, findings from a study on the mechanics of the vibration transmission in the skin reveal how the viscoelasticity of skin causes vibrations to attenuate in a highly frequency-dependent manner with distance. This motivated the design of a new spectral method for controlling the spatial transmission of haptic feedback. This method enables even a single actuator to elicit spatially varying haptic sensations, as revealed in perceptual experiments. These new effects also proved effective for enhancing engagement in virtual reality interactions.

These findings motivated a next stage of PhD research aimed at engineering compact haptic actuators with sufficient frequency bandwidth and control to reproduce haptic effects like those described in the preceding section. Achieving this goal is challenging, due to fundamental limitations arising from actuator mechanics and thermal processes. Overcoming these challenges required the development of new fluidic electromagnetic actuators that encapsulate ferrofluid, a functional material, within a multimaterial device. These actuators can outperform all existing compact haptic actuators in several respects. They are capable of controlled reproduction of mechanical signals over a frequency bandwidth from 0 Hz to more than 1000 Hz, spanning the full range of human tactile sensitivity.

The final part of the PhD presents a new approach to providing haptic feedback to extended areas of the skin via practical devices, with applications in augmented and virtual reality. It proposes a new technique for delivering spatially programmable haptic feedback via projected light, mediated by a novel optoelectronic layer worn on the skin. The resulting devices represent the first haptic virtual reality technology for enabling one to "see" optical patterns via the skin. The efficiency of these devices could one day enable their practical application in extended reality systems.

Contents

List of Figures

List of Tables

Chapter 1

Introduction

The sense of touch is our primary mode of physically interacting with and perceiving our surroundings, and plays an essential role in many day-to-day activities. For example, the simple act of grasping and manipulating an object relies on tactile sensory input from the hand in order to appropriately modulate grip forces to ensure grasp stability and accomplish task goals [8]. Internal body maps, alongside position sensors within our joints, are essential in the planning and control of the movement of our hands and feet [9]. Similarly, using the hands to identify the shapes, materials, and textures of objects requires input from several tactile sub-modalities that provide information about forces, displacements, and contact vibrations [10]. The term haptics, derived from the Greek $\dot{\alpha}\pi\tau\iota\kappa\acute{o}\varsigma$ (haptikos, "able to grasp or perceive") is today used to refer to the science and engineering of technologies related to the sense of touch.

During our interactions with the world, information from the sense of touch is used in close conjunction with that obtained from other sensing modalities such as vision and audition, to generate a more robust and holistic understanding of the environment. Despite significant engineering efforts spanning several decades, current haptic technologies are far from being able to reproduce the gamut of haptic signals that can perceived, or of being able to reproduce the range of haptic signals that are felt in naturally occurring interactions. When compared

1

with contemporary video and audio displays, haptic display technologies thus remain relatively primitive in their capabilities. With touch being our primary means of interacting with the world, this has led to an paucity of realistic human-computer-interaction methods. This gap in the stimulation of the senses is further exacerbated within virtual and augmented reality (VR, AR), where state-of-the-art devices have matured to provide extremely convincing renditions of virtual environments and objects, with a notable drawback - without the capability to touch these virtual objects, they can often feel artificial and lifeless.

A major challenge in the development of such haptic technologies is that the primary sensory organ of touch – the skin – is the body's largest, most distributed sensory organ, with a total surface area approaching two squared meters. Further, the skin is a heterogeneous sensory organ. It contains receptors for various sensing sub-modalities, such as pressure, vibrations, strain, temperature, pain, and position, making it unique among the sensory organs. In addition, touch is an active sense, with the brain using knowledge about the position and movement of the skin to infer additional information about the object being touched. This makes it extremely challenging to engineer a device that can furnish the range of tactile signals to the skin that are felt when perceiving or interacting with common objects and surfaces. Thus, there is a great need and opportunity to develop devices and methods that can stimulate specific aspects of the sense of touch in a practical and efficient manner. Achieving this engineering goal would provide many opportunities for enriching human-computer interactions within AR and VR by enabling the rendering of complex and varied sensations that improve the quality of tactile interactions. This could be used to either replicate real-world properties and behavior with virtual objects and interfaces, or to explicitly facilitate greater information transfer through the haptic modality.

This PhD dissertation presents several contributions toward this overarching goal of designing methods to effectively and efficiently stimulate the skin. Because the field of haptics involves a close interplay between gaining knowledge on touch perception and the develop-

ment of technologies that effectively target the sense, the research required to achieve goals is highly multi-disciplinary. Reflecting this, the research presented within the dissertation is interdisciplinary, incorporating elements of sensing, psychophysics, skin biomechanics, and haptic actuator design.

The dissertation integrates new findings about the brain's capacity to infer the locations of the fingers (Chapter 3). Information of this kind is valuable for specifying the engineering requirements of hand sensing and tracking systems. This dissertation also includes investigations of the until recently underappreciated role of soft tissue biomechanics in altering and distributing tactile signals (Chapters 4). It applies the resulting knowledge to create new rendering methods that generate tactile sensations over large spatial distances with just a single actuator. The results motivated further research within this dissertation that yielded a new high-fidelity haptic actuator capable of delivering complex tactile sensations across a wide range of frequencies (Chapter 5). Finally, motivated by the impressive spatial and temporal resolution of the skin, it presents a new haptic display technology that provides a practical means of generating controllable haptic feedback over arbitrarily large areas of the skin, which has been a longstanding goal in haptics (Chapters 6). A more detailed summary of the contents and contributions of the dissertation are provided in the following sections.

1.1   Overview

This dissertation is organized in several chapters describing key investigations that together comprise this PhD research.

Following this introduction, Chapter 2 presents background knowledge about human touch perception, explaining how external mechanical stimuli are transduced into neural signals, which are then interpreted by the brain to result in tactile sensations. In addition, it provides an overview of haptic actuation technologies, and a discussion of the current and proposed

implementations of haptics in VR and AR. Additional background information and literature is reviewed within the chapters describing each of the constituent projects of this dissertation.

Most meaningful manual interactions involve the integration of movement and associated haptic sensing, with the brain using this information to generate a robust perception of touch. Existing knowledge about an important element of this process, the fundamental ability of our brain to infer the locations of our hands and fingers, is limited. Motivated by this, the first research topic investigated in the dissertation explored this from a human factors perspective in Chapter 3 (which is based on publication [11]), by studying the ability of humans to localize their fingers within a virtual environment. Perceptual experiments were used to evaluate the errors in the localization of multiple fingers. The localization was surprisingly error-prone, with errors representing a significant fraction of both the length and range of motion of the finger. In a follow-up experiment, I determined that contextual visual cues, such as the locations of any un-occluded adjacent fingers, drastically reduce the errors in localization, suggesting that information from vision is used to refine position estimates. These findings help elucidate human hand function, and inform requirements for hand tracking hardware and rendering methods for virtual reality devices.

The dissertation next presents investigations on the generation of touch sensations. Recent research has indicated that contrary to conventional assumptions about touch, perceptually relevant information is captured at skin locations far away from the contact with an actuator or object, however there has been limited research systematically studying the influence of skin biomechanics on this effect. Motivated by this, Chapter 4 (which is based on publication [12]) investigates the biomechanics with a study of mechanical wave propagation in the skin using full-field vibrometry methods. The results of this study showcased that the viscoelastic nature of human skin causes damping behavior to vibrational stimuli to be frequency dependent. The analysis revealed a very consistent and powerful trend, namely, the damping varied monotonically with frequency, with propagation distances decreasing rapidly with an increase in the

frequency of stimulation. By exploiting this behavior, new haptic rendering methods were developed by constructing waveforms with systematically varying frequency content. These methods generate, with just a single actuator, perceptual sensations that are consistently reported to expand or contract in spatial extent from the location where the stimuli is applied. The spatiotemporally varying sensations were shown to result in significantly more engaging interactions within a virtual reality setting. These findings demonstrate how the physics of waves in skin can be utilized to generate spatiotemporal tactile effects over large surface areas with a single actuator, in a manner that is both practical and effective.

The results of Chapter 4 show that a larger, more expressive class of haptic effects can be generated using actuators with a wide frequency bandwidth. However, the current state-of-the art of compact haptic actuation technologies are limited in their ability to generate wide-bandwidth mechanical stimulation and large forces; due to resonance based effects and thermal limitations. To address this shortcoming, Chapter 5 presents the design and evaluation of a new type of haptic actuator. The design, which is based on voice coil technologies and the principle of electromagnetism, utilizes two permanent magnets in conjunction with an conductive coil and core assembly and a fabric reinforced membrane. An equivalent mass-spring element contacts the skin and displaces as a function of the applied current. A viscous fluid with suspended iron particles (ferrofluid) is incorporated into the system to increase the efficiency of the magnetic circuit, improve thermal performance, and introduce damping to minimizes the effects of mechanical resonance. The constructed prototype can generate sustained forces of 0.5 N, transient forces of 10 N or beyond, and frequencies over a wide bandwidth from DC to 1000 Hz. This actuator can therefore reproduce signals with high temporal resolution and high dynamic range. I then constructed a wearable device utilizing this actuator, and show through evaluation experiments that it can replicate the spatiotemporal tactile effects presented in Chapter 4, from a physically much smaller form factor than previously utilized. This actuator shows great promise for improving the fidelity of tactile sensations that can be obtained from

wearable haptic displays for AR and VR.

The next chapter of the dissertation utilizes an innovative approach built upon recent advances in the fabrication of flexible electronics to create a soft and conformable haptic display that can simultaneously deliver haptic feedback at multiple locations over large areas of the skin, which is presented in Chapter 6. The device is constructed as an array of functional units that consist of an electrical circuit utilizing surface mount electrical components embedded within a flexible substrate, and electrodes that contact the skin to deliver safe, low intensity current pulses that directly stimulate the sensory nerves. To address the challenges of controlling the array and allow for scalability, each functional element ("taxel") is designed to independently deliver current to the skin when it is exposed to a specified amount of light. This enables the device to be optically programmable, which allows for a controllable optical source such as a projector to operate the display with light patterns, effectively allowing the skin "see". The proposed display as constructed is lightweight (<8 gram for a 14 taxel array), and can conform to the curvature of the finger, resulting in minimal encumbrance when compared with electromagnetic actuation methods. This haptic display builds towards a longstanding goal of developing practical devices that can effectively target the continuum of the skin with a high spatial resolution.

Finally, Chapter 7 summarizes the research done in this PhD, synthesizes the findings, and describes future research avenues and applications of this work.

1.2   Contributions

The key contributions of the research are summarized as follows:

1. It presents new information about human abilities to spatially localize the fingers via haptics, and how these abilities are enhanced in the presence of partial visual information (Chapter 3 and publication [11] in the IEEE Transactions on Haptics). It shows that large

random and systematic errors affect the proprioceptive localization of the fingers, gauged relative to the size of the hand and range of motion of the finger.

2. The aforementioned finding also has important implications in the development of hand tracking systems for virtual reality. It suggests large errors in absolute position estimation might be tolerated without causing a reduction in the sense of immersion, provided the relative positions of individual fingers are well represented. This work has influenced research in several other groups, and the published paper [11] was awarded the Best Journal Paper Award amongst papers published in the IEEE Transactions on Haptics journal in the year 2020.

3. It presents new characterizations of touch elicited mechanical waves in the skin, and shows that the damping of the medium, and therefore propagation distances of these waves, are highly dependent on the frequency of vibratory excitation (Chapter 4 and publication [12] in the IEEE Transactions on Haptics). This research expands on the growing body of knowledge studying the influence of skin biomechanics on tactile perception, and can inform the design of compact and efficient haptic sensing and actuation methods.

4. Informed by the prior findings, this PhD proposes new methods for delivering spatially varying haptic feedback over distributed areas of the skin (Chapter 4 and publication [12]). This feedback method is based on a controlling frequency content in the signals in order to vary their spatial extent. Experiments revealed this approach to be effective, even when used with a single actuator. This is the first single actuator method for generating spatially varying haptic effects. These haptic effects significantly improved engagement in virtual reality interactions. A demonstration of this method that I presented at the World Haptics Conference 2019 was recognized as the Best Technical Demonstration (rank 1/64 demonstrations) by a panel of experts in this research domain due to its highly

effective perceptual nature. Further, the earlier conference version of this paper [13] was a finalist for the Best Student Paper Award (rank 3/80 papers) at the same conference. The simplicity and efficiency of this method makes it attractive for implementation in resource constrained devices such as controllers for virtual reality.

5. This PhD presents the new methods for engineering compact electromagnetic haptic actuators that are able to reproduce mechanical signals over the entire frequency bandwidth of the human sense of touch in a controlled manner (Chapter 5, parts of which are submitted to the journal Sensors and Actuators A: Physical). These actuators are compact (order of 1 cm^3), thermally efficient, can reproduce frequencies from DC to 1000 Hz, and is capable of delivering large transient and sustained forces relative to its volume. In performance, they compare favorably to previously investigated devices of this kind. This high-fidelity actuator shows great promise for implementation within a wide variety of wearable haptic applications.

6. The PhD also contributes a new approach to providing spatially programmable haptic feedback to the skin via projected light (Chapter 6, work being prepared for submission to a multidisciplinary journal). This technology is based on an efficient skin-interfaced optoelectronic circuit design in which an array of functionally independent tactile pixels ("taxels") furnish localized electrotactile feedback to the skin when activated with locally incident light from an optical source. Unlike conventional approaches to controlling electrotactile arrays, this design can scale to large surface areas or integration densities without a commensurate increase in electronic complexity. It enables the distributed stimulation of many locations on the skin without need for additional processors or multiplexing.

7. Finally, motivated by this new optical method for delivering haptic feedback, this PhD presents knowledge and methods for the design and fabrication of stretchable skin-

interfaced optoelectronic devices for stimulating the skin (Chapter 6). The fabricated display is thin and light, conforms to the fingers, and can deliver optically programmable haptic patterns to the skin with substantial spatial resolution. The stretchability of these devices enables them to accommodate movements of the body with little restriction. These attributes could makes this technology well suited for future applications in virtual and augmented reality.

Chapter 2

Background

This chapter reviews prior knowledge and literature as general context for the research presented in this dissertation. Additional background literature appropriate for the different research projects included in this dissertation is provided in background and introduction sections of Chapters 3 through 6.

Haptics refers to the science and engineering that relates to the sense of touch. It concerns "real and stimulated touch interactions between robots, humans, and real, remote, or simulated environments, in various combinations" [14]. It includes research that probes how humans perceive information about the environment through touch and movement, and also the engineering of technologies intended to stimulate the sense of touch. There has been an extensive effort to study this sense through the years, leading to great improvements in our understanding of varied aspects of the anatomy, neurophysiology and perception involved in this complex sense.

It is a major engineering challenge to design and build devices that can stimulate the haptic modality with high fidelity, particularly in comparison to the technologies that are tailored towards the visual and auditory senses. Consider some consumer technology devices that are increasingly prevalent in our day to day lives. Display screens on phones and computers have

had their resolutions improve an extent that they are able to almost perfectly reproduce a visual scene (such as a picture taken from a digital camera, or a virtual environment rendered for a game). Similarly, high fidelity speakers and headphones allow for exceptional reproductions of sounds and music, with new methods to obtain spatial audio that allows one to localize a virtual sound source in the environment being increasingly adopted. No analogous technologies to comprehensively stimulate the sense of touch exist.

In recent years, advances in visual and audio displays, computing, and rendering have given rise to the rapid development of virtual reality (VR), augmented reality (AR), and mixed reality (MR) head mounted displays (HMDs). These headsets serve to either immerse the wearer in a virtual environment, or to introduce computer-rendered virtual elements into the real world. New applications for such devices are regularly found in gaming, education and task training, and engineering design [15, 16, 17, 18, 19]. However, the virtual objects rendered by these HMDs are often only echos of their real-life counterparts, in part due to their inability to be reached out to and touched. A longstanding research goal has been to engineer haptic interfaces for VR and AR that allow their users to perceive contact with virtual objects, and identify object properties such as weight, surface textures, and temperatures [20, 21]. This has been a challenging problem due to several unique properties of the sense of touch.

The skin is far and away the largest and most distributed sensory organ. The sense is generated by varied types of receptors embedded within the layers of the skin and tissue that gather information about touch, pain, temperature, forces, and the position of limbs [1, 4]. These receptors are numerous, with estimates exceeding several hundred thousand, and are distributed throughout the skin with varying innervation densities [7]. This presents complex challenges for the design of devices and rendering methods that aim to reproduce the sensations of interaction with real objects. The identification of methods to optimally and efficiently stimulate the varied aspects of touch over its large surface area remains an open question.

Research within the domain of haptics requires a strong understanding of the anatomy and

biomechanics of the human body and the psychophysics of the sense of touch, which has to be paired with solid engineering principles for the construction of effective haptic technologies. In this thesis, I present research studying the position sensing and vibrotactile perception aspects of the human haptic sense, and showcase how the findings motivate and allow us to construct new haptic devices and rendering algorithms.

2.1 Human haptics and the sense of touch

The sense of touch is a highly evolved system involving a large number of distributed receptors, with heterogeneous subtypes that preferentially detect specific classes of sensations. The haptic information from the skin is often classified into two functional components, *cutaneous touch* and *kinesthesia* [22, 23]. Cutaneous touch cues arise from the receptors within the skin that detect, among others, pain, temperature, itch, and low-threshold mechanical stimuli such as pressure and vibrations over a large range of frequencies [1]. Kinesthetic information, which incorporates the sense of proprioception, is obtained from sensors within the muscles, tendons, joints and skin which signal the position and movement of the limb, and the forces being generated by the muscles. Information from both these modalities are integrated and combined with motion planning and coordination with the motor system to enable haptic explorations, with the active motion of the limbs being instrumental in the identification of shape, texture, weight, and other properties of objects [24, 25].

The haptic receptors transduce stimuli by inducing potentials and eliciting spikes within peripheral nerve fibres, which transmit information to the central nervous system [2]. As a consequence of the high innervation densities and mechanical transmissions of energy arising from skin biomechanics which we discuss further in Chapter 4 of this dissertation, even simple touch events excite spikes in large populations of these peripheral nerves. The spikes ascend neural pathways uninterrupted through the spinal cord, before interfacing with second order

nerves of the central nervous system (CNS) within the cuneate nucleus of the brainstem [26, 27]. From here, the pathways ascend through the thalamus, and then into the sensory cortex regions of the brain, with neural processing occuring at each connecting layer of synapses. Prior research has identified ways in which information of spike timings [28, 29, 30], spatial patterns [31] and firing rates [32, 33] in the population responses shape tactile sensations. The way in which information from the receptors is encoded and extracted to generate high level features such as roughness or shape, within the CNS, remains a domain of active research [34, 35].

The skin of humans and other primates comprises of both hairy and nonhairy / glabrous skin, with each having a distinct distribution of receptors. Glabrous skin is primarily found on the palmar side of our hands, and the soles of our feet, and is specialized for discriminative touch. Hairy skin covers most of the remainder of the body, and it also serves a discriminative touch role, but with considerably more limited acuity due to the lower number of embedded receptors. Further, hairy skin is also strongly associated with affective, or pleasant touch.

Mechanical stimulation provided to the skin is transduced and sensed with mechanoreceptors, which are specialized end organs of the sense of touch that are innervated with tactile sensory nerves. In glabrous skin, four types of low-threshold mechanoreceptors with fast nerve conduction velocities (Aβ LTMRs) have been identified, and which are of particular relevance to cutaneous touch. They are distinguished by their morphology, innervation densities, frequency sensitivities, and receptive field sizes [36, 37, 1, 38] (Fig. 2.1). The Merkel cells are embedded within the epidermis, and are responsible for reporting quasi-static touch contacts. The Meissner corpuscles are present in the folds of the dermis, and are sensitive to movements across the skin and other transient contacts. The Pacinian corpuscles (PCs) are embedded deep within the dermis, and are tuned to detecting vibrations over a wide frequency range. The Ruffini corpuscles are embedded within the dermis, and are sensitive to skin stretch. The Merkel cells and Meissner corpuscles are small in size, numerous, and have small receptive

13

field sizes. The Pacinian corpuscles in contrast are large structures, measuring up to 4 mm in length in adult human hands [39]. They are sparsely distributed, with only several hundred estimated to be located in an adult hand, and have the largest receptive fields, with individual Pacinians responding to vibrations presented in an area of 60 mm^2 around it.
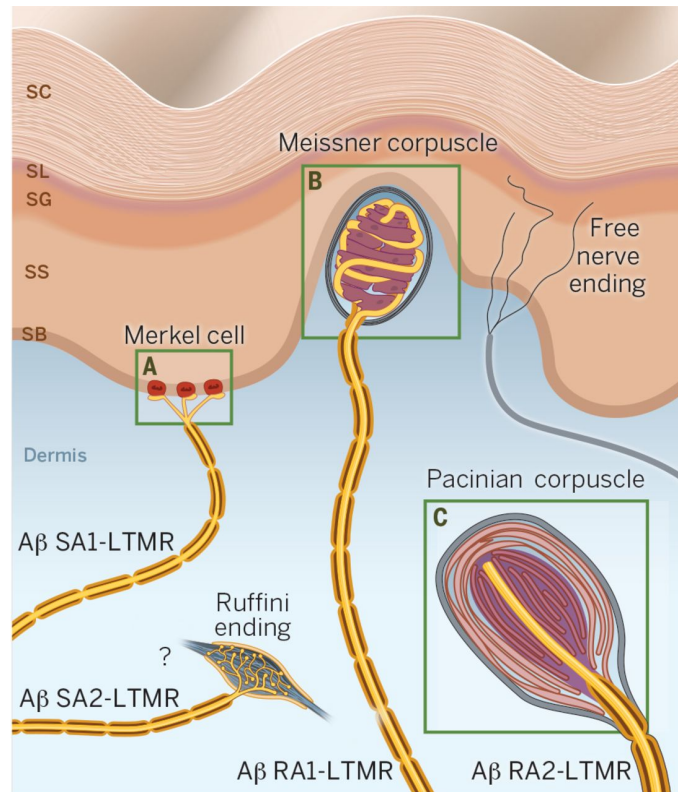
Figure 2.1: Low threshold mechanoreceptors embedded within glabrous skin. Reprinted with permission from the American Association for the Advancement of Science (Zimmerman, Bai and Ginty [1]), copyright (2014).

These mechanoreceptors are also alternately labelled based on their functional behavior of the associated sensory nerves, as either slow adapting (SA) or fast adapting (FA), as follows - SA-I (Merkel), SA-II (Ruffini), FA-I (Meissner) and FA-II (Pacinian) (Fig. 2.2. Slow adapting receptors and nerves respond to constant and slowly varying skin deformations, and cause nerve firing responses throughout the duration of the contact. In contrast, fast adapting nerves respond to dynamic skin deformations, as they set off nerve spikes during the ramp and decay
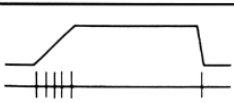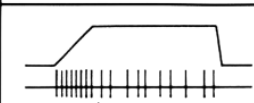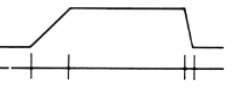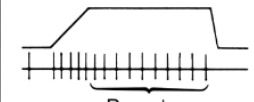
Figure 2.2:   Classification of the mechanoreceptors and sensory nerves found in glabrous skin based on functional behavior. Slowly adapting (SA) nerves respond to sustained stimuli, while fast adapting (FA) nerves only fire at the edges of stimuli. Type I receptors and nerves have small receptive fields, while the receptive fields of Type II are larger with more obscure borders. Reprinted with permission from the Canadian Psychological Association (McGlone et al. [2]), copyright (2007).

of the stimuli, while adapting to not generate a signal in the interim. The number in the above designations denotes their respective field sizes, with Type I nerves (associated with Merkel and Meissner receptors) having small fields, and those of Type II (associated with Pacinian and Ruffini) having large fields as discussed above. Each sensory nerve can obtain information from multiple mechanoreceptors. It has been observed that the Type I nerves are more densely located near the fingertips, highlighting the evolutionary transformations that allow our fingers to be exquisitely sensitive so as to improve their functionality of tactile exploration. While the dense innervations imply that the receptive fields of the receptors overlap greatly, prior research has shown how natural touch interactions are observed by multiple receptor types, and how

15

information from varied sensory submodalities is combined through neural processing stages before it reaches the somatosensory cortex [26].

Hairy skin contains similar sensory nerves as glabrous skin, but the mechanoreceptor end effectors can vary [1, 7]. SA-I nerves are connected to Merkel cells, while SA-II nerves are less observed and thought to connect to Ruffini corpuscles. However, Meissner corpuscles do not exist in hairy skin, rather FA-I nerves terminate in receptors connected to the hair follicles. This enables the hair to act as a sensing element. FA-II nerves exist and are connected to Pacinian corpuscles, but they are rarer and are situated in deeper tissues as compared to glabrous skin. In addition, there exists a type of nerve receptors called C tactile afferents that are present in hairy skin but not in glabrous skin, and there is evidence that this neural pathway is used for affective or emotional touch interactions, such as stroking [40, 41].
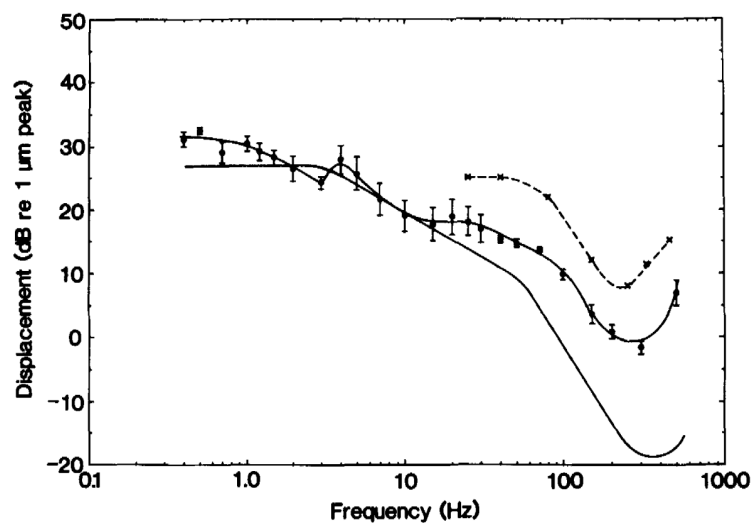
Figure 2.3: Perceptual absolute detection threshold of vibrations at varying frequencies from the FA-II (Pacinian Corpuscle) channel, for both glabrous skin at the thenar eminence (solid line only) and hairy skin at the forearm (filled circles and solid line). The skin is most sensitive at frequencies between 200 and 400 Hz. Hairy skin is an order of magnitude less sensitive as compared to glabrous skin, which can detect displacements as small as a 100 nm. Reprinted with permission from Taylor & Francis Ltd: Somatosensory & Motor Research (Bolanowski, Gescheider and Verillo [3]), copyright (1994).

The brain integrates spiking information from the population of sensory nerves across the

body to generate perception. Different stimuli types are associated with a characteristic detection threshold, above which the stimuli is consistently perceivable. For vibrational stimuli, the detection thresholds at which mechanical displacements become perceptible vary significantly with frequency, with peak sensitivities between 200 and 350 Hz ([42, 3], Fig. 2.3). At these frequencies, sinusoidal vibrations of peak-peak intensities as small as a few tens of nanometers applied at the fingertip can be identified. For hairy skin, the corresponding detection thresholds are at least ten times as large (i.e., less sensitive). These detection thresholds have also been shown to depend on other factors, such as temperature [43] and contact conditions and forces [44, 45], to a smaller extent. The age of a person has also been reported to have an effect [46], which has been hypothesized to be in part due to a reduction in the number of functional receptors as the skin ages.

	No. of sensory nerves	Innervation Density, units/cm^2	Skin area, cm^2	Slowly adapting (SA) sensory nerves, %
Hand	16,500	90	184	43
Fingertips	5,061	241	21	42
Fingers	6,156	81	76	45
Palm	5,046	58	87	41
Foot sole	3,958	21	200	37
Face	46,000	69	675	65
Neck and scalp	8,625	17	516	55
Trunk	41,600	9	4,500	55
Arms	35,335	13	2,769	61
Legs	56,186	10	5,722	47
Total	$\sim 230,000$	15	$\sim 15,000$	53

Table 2.1: Estimated number of sensory nerves in the skin. The fingertips and the hands are the most densely innervated regions, indicating the capture of rich tactile information from these locations. The total number of sensory nerves is of the order of 10^5. Reprinted under a Creative Commons 4.0 license (Corniani and Saal [7]), copyright of the American Physiological Society and the Authors (2020).

An estimation of the number of tactile sensory nerves across the body is given in Table. 2.1. The study of the sensory processing of the vast amount of data being generated by these nerves remains an area of active research.

While cutaneous touch receptors are primarily located in the skin, the specialized kinesthetic receptors are primarily located within the muscle spindles, tendons and the joints ([47, 4], Fig. 2.4). The receptors in the muscle spindles detect both the change, and the rate of change, of the length of the muscle, providing a sensory pathway for the identification of the position and movements of the limb. Signals from the Golgi tendon organs are used to identify tension, and therefore identify forces and the weight of handled objects. The receptors in the joints serve to detect the limits of motion.
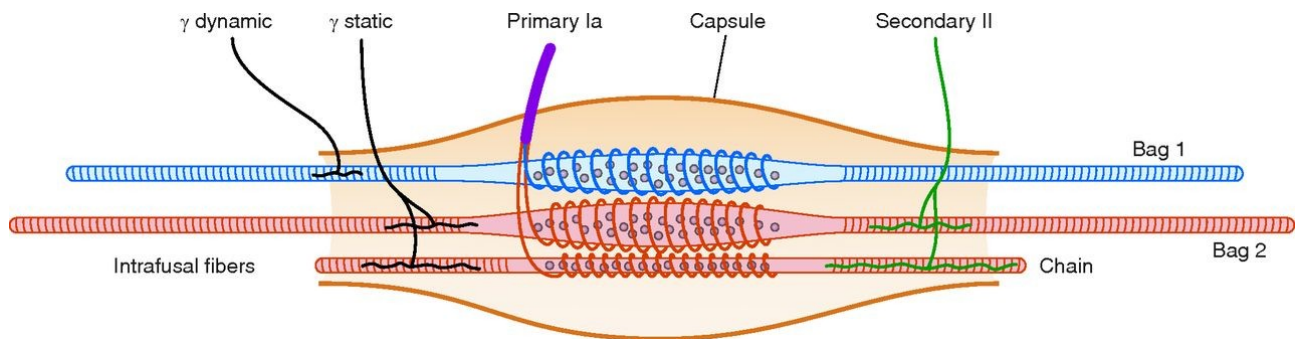
Figure 2.4: Diagrammatic representation of sensory receptors and nerves in skeletal muscle spindles. Specialized intrafusal fibers with multiple innervating nerve endings detect the length of the muscle they are embedded within, enabling the judgement of the position of the limb. Reprinted with permission from the American Physiological Society (Proske and Gandevia [4]), copyright (2012).

In addition to these, the SA-II receptors in the skin can also deliver proprioceptive cues of limb position [48]. Information from these receptors may be particularly relevant in detecting the positions of the fingertips, because the muscles that control the fingers are located at a distant location in the forearm, and thus signals from it are likely to be ambiguous. A more involved discussion of the proprioceptive localization of fingers is included in Chapter 3.

2.2   Skin Biomechanics

With the skin being the primary sensory organ for the detection of mechanical sensations such as contact forces and vibrations, the role of the mechanical properties of the skin and its

resultant influence on perception is of particular interest, and examined in Chapter 4 of this dissertation.

The skin is a continuum surface, and its mechanical properties (in a simplified form) can be approximated by a distributed array of mass spring dampers [49] with complex geometry and boundary conditions. Thus, dynamic mechanical contact results in dynamically propagating patterns of strain over the surface, which can excite neural responses from tactile receptors at locations far away from the point of stimulation. There is significant recent evidence that shows how vibrational signals captured at remote locations contains substantial information [50, 51, 52] and can be perceptually significant [53, 54]. However, even though well accepted, this behaviour is rarely accounted for during the design of haptic devices [55].

The skin also exhibits several interesting mechanical properties such as viscoelasticity and hyperelasticity [56, 57, 58], which further complicates its modelling. A simple way to demonstrate the latter behavior is to apply pressure onto a finger, where one can observe that for indentations beyond a couple of millimeters, the skin rapidly stiffens up. Over the years, several finite element methods have been proposed which incorporate these complex properties to attempt to accurately model the behaviour of the skin during varied touch interactions [59, 60, 61]. A further discussion of the viscoelastic nature of skin, and its impact on the propagation of mechanical energy is provided in Chapter 4.

2.3   Tactile Illusions

The research presented in this dissertation investigates efficient and practical methods to stimulate the skin. Tactile illusions arise when the perception through the sense of touch is not in agreement with the physical stimuli, often in a surprising manner [62, 63, 64]. While not as well-known as visual illusions, several tactile illusions have been identified and described over the years, and these illusions have been utilized to generate efficient haptic display systems.

A rigorous explanation for the origin of perceptual illusions typically arises from a study of how the brain interprets information from the senses [65]. In the context of touch, the physical stimuli imparted to the skin is mediated by the biomechanical coupling to generate the signals in the populations of sensory nerves, with each channel transmitting a subset of the information. The task of the brain then, is to take these large collection of signals and generate a percept. To help accomplish this task, the brain uses information from a wide range of senses and sensory submodalities, and utilizes them in conjunction with prior expectations that have been been constructed through experience.

In some cases, a Bayesian probabilistic model has been shown to accurately predict the results of sensory integration [66, 67, 68]. Several studies have suggested that the existence of probabilistic priors can explain varied tactile illusions, and provided direct evidence to support this [65, 69, 70]. For example, with the well known size-weight illusion, where a smaller object is perceptually rated as heavier than a larger object of equal mass, Flanagan et. al [71] have shown how the effect can be inverted with a sufficiently long practice. A more detailed investigation of sensory integration and priors that explain illusions is beyond the scope of this review, but nonetheless, the identification and study of perceptual illusions have proven invaluable in elucidating the functioning of the human perceptual system, and such illusions have been utilized to construct evocative haptic rendering methods.

An interesting sub-class of tactile illusions involve patterns of transient or vibrotactile stimuli applied to the skin, which can result in a perception of motion, or cause errors in stimuli localization. Some examples of such illusions are described in brief below.

- **Tactile apparent motion** - When a number of discrete taps are applied sequentially at multiple locations on the skin, it is reported as a single stimulus moving across the skin [72] (Fig. 2.5). The optimal onset interval between subsequent stimuli is a function of the duration of the stimuli. These effects have also been reported in a less robust manner

when mechanical stimuli is applied across different body locations.

- **Sensory funneling (phantom tactile) illusion** - When brief stimuli are applied simultaneously at several closely located points on the skin, they are often perceived as a single sensation at the center of the stimulus pattern, as if the stimuli are being funneled to a central location (Fig. 2.5). It is possible to move the perceived location of the stimuli by adjusting the relative intensities of the constituent stimuli [73]. The maximum distance between stimulation locations that preserves the phantom sensations depends on the location of the body [74].

- **Sensory saltation (cutaneous rabbit) illusion** - When a series (3-6) of short pulses is applied successively at three different loci on the skin, it is perceived as a stimuli is progressively moving, or 'hopping' from the first to the third location [75]. An important factor in the applicability of the illusion is the area of the skin over which the stimuli has to be delivered. In regions of low innervation densities, the stimulation methods can be placed further apart.

These tactile illusions have been proposed as a means to greatly reduce the number of actuators required for wearable haptic displays, which is an application where the compactness and efficiency of the device is of great importance [76, 5, 77]. More recently, Park and Choi [78], have closely investigated the information transmission through phantom sensations, showing that phantom sensations of motion are more clearly identified as compared their stationary counterparts, alongside other findings. Several studies have proposed utilizing the principles of tactile illusions to obtain succinct sensations of motion that travel along the skin [79], penetrate the body [80], and even extend beyond the body into regions without any actuators [81].

The design of haptic effects is further discussed in Chapter 4, which utilizes knowledge of biomechanics to present a new type of tactile illusion that is systematically generated through the construction of patterns of spatial wave fields in the skin, wherein the user touches an
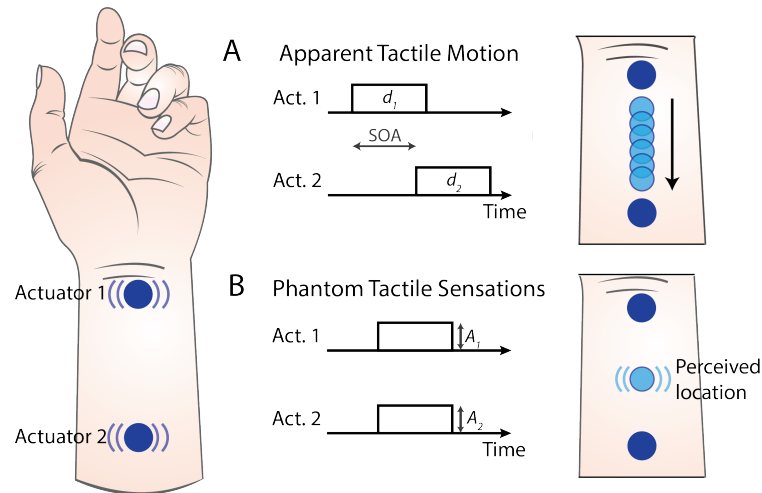
Figure 2.5:   Previously discovered vibro-tactile illusions.   Apparent tactile motion (A) presents vibrational stimuli to two distinct locations on skin with a temporal offset between the signals (Stimulus Onset Asynchrony, SOA), resulting in a perceived sensation of motion between the actuators. Phantom tactile sensations (B) present temporally aligned stimuli to two distinct locations on the skin, which results in a perceived sensation located at a region of skin between the two actuators. (Adapted from Israr and Poupyrev [5])

actuator with their fingertip, but clearly perceives spatiotemporally varying sensations through the length of the finger.

2.4   Haptic technologies

This dissertation investigates methods to develop wearable haptic displays for use with virtual and augmented reality, specifically within Chapters 5 and 6. These displays consist of constituent haptic actuators, alongside devices which integrate them, both of which are discussed here.

2.4.1   Haptic actuation methods

Haptic actuators are transducers which convert input energy into mechanical or electrical stimulation, and they serve as essential component for any haptic display aiming to provide

sensations to the sense of touch [82]. The feedback from haptic actuators plays a important role in many familiar objects, from the taps delivered on typing on the virtual keyboards of smartphones, to the expressive patterns of vibrational feedback used to denote various classes of notifications within smartwatches, and the vibrational rumble patterns designed to enhance the immersion with video game controllers. Indeed, vibrotactile feedback is a dominant method for delivering haptic sensations within commercial devices. Other classes of haptic devices include those that deliver kinesthetic (force) feedback, such as those used in devices aiming to simulate surgical training or driving; friction modulation devices, which aim to recreate the textures of materials on flat surfaces such as touch screens; skin deformation devices providing normal indentations, such as those used in refreshable braille displays; and mid-air ultrasound devices, which provide a non-contact method of delivering low intensity normal indentations to the skin. There have been several additional types of devices which have been proposed in research over the years, but which have yet to be commercialized.

Historically, kinesthetic (force) feedback devices have had significant attention devoted to them due to the motivation of recreating the feedback achieved from real-life tools, for applications in training and tele-robotics. The most commonly used class of such devices consist of grounded desktop multi-link mechanisms that utilize electrical rotary motors, encoders, and force sensors [83, 84]. These can be programmed to apply three-dimensional physical forces and torques to the user, relative the the operator's ground [14].

More recently, a majority of research in the haptics community has focused on cutaneous feedback, in part due to the compactness achievable with such devices. The haptic actuators that are designed to deliver cutaneous (or tactile) sensations can be tuned to preferentially influence various sub-modalities of the sense of touch, such as skin vibrations, transient contacts, skin deformations, lateral displacement patterns and skin stretch, with Culbertson et al. providing a recent review of the state of the art in haptic devices [85]. To better situate the research presented within this thesis, a detailed discussion of vibrotactile actuators and electrotactile

stimulation is provided, with other actuation methods being out of the scope of this review.

Vibrotactile actuators

The human skin can readily identify low amplitude displacements or forces that temporally vary with high frequencies, with these stimuli commonly referred to as vibrations. During natural interactions, these vibrations are regularly used to detect transient contacts with objects, and information about surface textures and roughness. Many application areas for vibrational stimulation in human computer interaction have been investigated due to the large amount of information which can be delivered through this modality alongside the ease of integration of vibrotactile actuators within devices, and many more are still emerging [85].

The role of vibrotactile actuators then, is to provide forces and therefore mechanical displacements to the skin across a range of frequencies. In addition to the peak amplitudes, power consumption, form factor, and the operating range of frequencies which the actuator can reproduce, several other design considerations exist in the development of haptic actuators, as follows. If the actuator has a flat response over its bandwidth, this proves advantageous for the generation of high-fidelity haptic sensations without the need for equalization. If the frequency bandwidth of the actuator extends down to 0 Hz, then the DC component can also serve to provide constant skin deformations, and thus also stimulate the Merkel cells. Further, if the actuator can be designed to have minimal start (onset/rise) and stop times, then vibrotactile actuators can also be used to provide sensations of transient contact through impulsive signals. The mechanism used to mount and interface vibrotactile actuators to the skin also deserves careful design, to optimize the quality of the sensations.

Some of the commonly used types of vibrotactile actuators used in wearable haptic devices are as follows, with Choi and Kuchenbecker [86] providing a more detailed review -

- **Eccentric Rotating Mass (ERM) Motor** - A relatively old technology, ERM motors

24

use an off-center mass affixed to the shaft of a rotary DC electric motor. This design in-
herently couples the amplitude and frequency which this actuator can generate, because
applying a larger control signal results in the eccentric mass rotating at higher frequen-
cies, while also providing larger forces. This reduces the range of usable frequencies,
with a complete inability to generate forces at 0 Hz. Further, internal friction and inertia
result in large start times, typically around 30 ms.

- **Voice coil** - Voice coils are electromagnetic linear actuators that operate on a similar prin-
ciple to audio speakers. They either have an electromagnetic coil enclosing a movable
permanent magnet, or a movable coil adjacent to a fixed permanent magnet. A spring is
used along with bushings to hold the moving mass in place and allow it to return to the
central rest position. Several companies sell voice coils devices optimized for vibrotac-
tile rendering, with usable bandwidths from 80 Hz to 1000 Hz. These devices are either
intended to operate around their broad mechanical resonances [87], or at frequencies
above the resonant frequency [88]. Start and stop times typically range from 15 to 20
ms. These devices cannot generate DC forces.

- **Linear Resonant Actuator (LRA)** - The technology used in most modern commercial
devices, LRAs are a subset of voice coil devices which are designed to have a very sharp
(high-Q) resonance [89]. This allows them to be extremely efficient when driven at
their resonant frequency, however it is difficult to obtain appreciable intensities at other
frequencies. The start and stop time for these actuators are typically around 5-10 ms
when used with custom driver ICs, which allows a haptic designer to generate transient
pulses and perform pulse width modulation. Nevertheless, these actuators do not have
full independent control of the frequency of stimulation.

- **Piezoelectric Actuator** - These actuators rely on the piezoelectric effect - where the
charge applied to a material results in a mechanical displacement. Stacks of piezoelec-

25

tric materials are typically embedded in a cantilever beam configuration [90] or within a cymbal structure [91] to amplify the mechanical displacements. These actuators have a range of operating frequencies from DC to 500 Hz, and start and stop times of ≈ 1 ms. However, a primary disadvantage of these actuators is that they are hard to power, requiring driving voltages of 150 V or higher to achieve appreciable deformations. Thermal limitations also prevent them from generating frequencies beyond 500 Hz.

Electrotactile stimulation

An alternative method to providing cutaneous sensations is to bypass the mechanical transducers and directly stimulate the sensory nerves. This is done by providing low-intensity currents via electrodes to the skin, which propagate to subdermal regions and set off spiking potentials within the nerves [92, 93], effectively bypassing the haptic mechanoreceptors. The typical power draw of an electrotactile stimulator are an order of magnitude lower than a comparable mechanical actuator. Because of the integration densities possible with electronic components and electrode arrays, electrotactile devices have the distinct advantage of being more portable, wearable, and efficient as compared to mechanical actuation, particularly when a large number of actuators are to be used [94]. The quality of the electrotactile sensation depends on parameters such as the electrode dimensions, the duration, amplitude and frequency of the current, and the thickness of the skin [93, 95, 96, 97], with these parameters having to be carefully selected to minimize any discomfort. To limit the possibility of adaptation and to preferentially excite specific classes of nerves, currents are delivered through monophasic or biphasic square pulses [96, 98], with specifically designed pulse widths and repetition frequencies. The electrodes are constructed with skin compatible metals such as gold or stainless steel, or with soft hydrogels [99]. A further discussion is presented within Chapter 6 of this dissertation.

2.4.2   Haptic interfaces for VR, AR, and HCI

Within virtual and augmented reality systems, haptics can play an important role in the generation of an immersive virtual environment that allows for interaction with virtual objects. During the generation of realistic interactions, force feedback provides the user with information about the hardness, weight and inertia of virtual objects. Cutaneous feedback is used to provide the user with a sense of the contact geometry, smoothness, skin stretch and slip, and temperature. Finally position sensing is essential for the identification of the body posture, allowing for accurate recreations of the hands and fingers in the virtual world [20, 100].

Most haptic display devices utilize the fact that the sense of touch involves the integration of multi-modal information, and are constructed using a combination of actuators that can stimulate distinct modalities of touch (Fig. 2.6) [6, 101, 102]. Therefore, haptic displays for kinesthetic and cutaneous feedback are usually developed independently, and integrated as required. There are also several additional considerations involved in the design of haptic devices for AR and VR - in addition to the optimization of performance, there is a preference to have the device be wearable, light-weight, comfortable and low-cost. The devices should ideally not impose additional kinematic constraints on the hand, and not encumber the fingertip, allowing for free exploration of real-world objects.

Kinesthetic feedback devices

Grounded kinesthetic devices (Sec. 2.4.1) are used for tool-mediated interactions in VR such as tele-operation, surgical training and mechanical assembly, where large output forces (> 10 N) are desired from desktop based systems [103, 104, 105]. More recently, with the free-form haptic exploration interaction paradigm becoming more prevalent for virtual and augmented reality, ungrounded and hold-able force feedback devices have seen significant research efforts devoted to them [14].

Figure 2.6:   Representative haptic multi-modal devices proposed for use in VR in various form factors. Reprinted with permission from the IEEE (Wang, Ohnishi and Xu, 2019 [6]), copyright (2019)

When designing a wearable haptic display, the positioning of the grounding location, where the reaction forces are generated, has an large influence on its ability to generate kinesthetic feedback. Perceivable forces are low when the grounding location is close to the point of application of force [106, 107]. One class of wearable kinesthetic devices are the exoskeletons with either rigid links or cables [108, 109, 110, 111, 112, 113], which are grounded at the limbs and body. While exoskeleton based systems can provide large forces (> 5 N), they are often bulky, complex and expensive. Several researchers have also proposed one-dimensional force feedback within hand-held controllers, where an electrostatic brake is used to restrict movement and allow for the opposing region of the hand to provide the grounding force [114, 115, 116].

A similar braking mechanism mediated through cables has been proposed to preferentially restrict movements of individual fingers [117]. Recently, direct stimulation of the muscles with electrical currents has been proposed as an alternative method to provide kinesthetic sensations of contact with virtual objects [118, 119].

Cutaneous feedback devices

Cutaneous feedback devices rely on the delivery of cutaneous cues such as skin contact and vibrations to provide information about virtual objects. Such devices are commonly utilized in consumer applications in virtual and augmented reality, where minimizing the weight and size of the haptic display is a priority. The research presented in this dissertation focuses on developing methods to deliver cutaneous feedback through wearable devices, reflecting recent trends within the field.

Pacchierotti et al. provide a comprehensive review of wearable displays for the fingertips and hand [120]. Broadly, wearable haptic devices can be characterized as providing any of the following -

- **Vibrations** - These devices allow for the delivery of sensations of textures and transient contacts. Specific form factors include placing multiple vibrotactile actuators on the hands and fingers using glove-like interfaces [108, 121, 122, 123, 124, 125], band-based approaches where the actuators are embedded along the circumference [126, 127, 128], or controller based and hand-held implementations [129, 130].

- **Normal indentations** - These devices convey sensations of contact and pressure with virtual objects. Wearable embodiments for VR and AR have been constructed using movable platforms under the fingertips [131, 132, 133, 134] and pin arrays [135, 133, 136, 137].

- **Lateral skin stretch** - These devices reproduce sensations of slip and friction that com-

monly arise during skin-object interactions. Wearable devices use electric motors [138, 139, 140, 141] or pneumatic actuation [142] to displace an end effector that is firmly contacting the skin.

- **Electrical stimulation** - Recent implementations of electrotactile devices for virtual reality primarily consist of body-worn electrode arrays that aim to enhance the information of contact with virtual objects [143, 144, 145, 146].

Position sensing of the hands

The hand and fingers form a highly kinematically complex system with many mechanical degrees of freedom, which facilitates its incredible dexterity. This nature of the hand makes the accurate estimation of its pose a highly challenging problem, but successfully solving it to create a registered hand representation within VR has obvious benefits in terms of significant improvements in the immersion generated by the system [147, 148, 149].

Through the years, several approaches have been proposed for tracking the pose of the hand [150]. Discrete sensing solutions integrate flexural sensors [151, 152], inertial measurement units [153], or a combination of the two [154], at multiple locations within a hand-worn glove. Such devices often require calibration, and errors can arise from sensor drift, and due to the differences between the implicit joint model used by the device and the structure of the individual's hands. However, these devices also tend to have the most robust tracking when considering all possible poses of the hand.

Alternately, optical methods for hand tracking can be employed. These utilize computer vision and machine learning approaches on data collected from stereoscopic cameras or depth sensors to estimate the positions of keypoints on the hand [155, 156, 157]. The most commonly used device within the class is the Leap Motion sensor [158], which uses two monochromatic infrared cameras to recognize the pose of the hand. This device is inexpensive, and with the

availability of mature plug-ins for game engines, easy to integrate within virtual reality applications. More recently, virtual reality headsets using inside-out tracking cameras have also used optical methods to allow for controller-free interactions with virtual environments [157, 159]. While optical methods do not encumber the user, they tend to require more precise positioning of the hands relative to the camera. They are also less robust with their tracking, with the occlusion of hand regions from the view of the cameras (that regularly occurs during natural motion) often resulting in large pose tracking errors.

Errors in hand tracking beyond the precision of proprioceptive localization can result in a loss of immersion, and a reduction in the quality of haptic rendering due to errors introduced to the feedback system of hand movement and touch sensing within the brain. In order to lead to a better understanding of these effects, Chapter 3 of this dissertation presents an evaluation of the inherent accuracy of human proprioceptive localization of the fingers.

Chapter 3

Proprioceptive Estimates of Finger Location Are Coarse, Biased, and Context-Sensitive

Haptic experiences arise from the integration of information about the movement of our hands and body, and the resulting kinesthetic and cutaneous sensations. While there has been an extensive body of work on studying the proprioceptive localization ability for the arms and hands, the localization of individual fingers, which plays an invaluable role in most haptic interactions, was far less understood. This chapter addresses this gap in knowledge through new perceptual experiments using a virtual reality paradigm, which show that the inherent localization errors are surprisingly large. However, the accuracy greatly improves when partial visual cues about adjacent fingers are provided. The findings contribute to the goal of achieving high fidelity haptic rendering for the whole hand within virtual reality by informing engineering requirements for hand tracking systems, clarifying that the necessary spatial tracking precision can be coarser than commonly thought.

The content of Chapter 3 is adapted from the following reference [11] :

B. Dandu, I. A. Kuling and Y. Visell, "Proprioceptive Localization of the Fingers: Coarse, Biased, and Context-Sensitive," in *IEEE Transactions on Haptics*, vol. 13, no. 2, pp. 259-269, 1 April-June 2020, ©2020 IEEE.

Reproduced here with permission from the IEEE, doi: 10.1109/TOH.2019.2899302.

Abstract

The proprioceptive sense provides somatosensory information about positions of parts of the body, information that is essential for guiding behavior and monitoring the body. Few studies have investigated the perceptual localization of individual fingers, despite their importance for tactile exploration and fine manipulation. We present two experiments assessing the performance of proprioceptive localization of multiple fingers, either alone or in combination with visual cues. In the first experiment, we used a virtual reality paradigm to assess localization of multiple fingers. Surprisingly, the errors averaged 3.7 cm per digit, which represents a significant fraction of the range of motion of any finger. Both random and systematic errors were large. The latter included participant-specific biases and participant-independent distortions that evoked similar observations from prior studies of perceptual representations of hand shape. In a second experiment, we introduced visual cues about positions of nearby fingers, and observed that this contextual information could greatly decrease localization errors. The results suggest that only coarse proprioceptive information is available through somatosensation, and that finer information may not be necessary for fine motor behavior. These findings may help elucidate human hand function, and inform new applications to the design of human-computer interfaces or interactions in virtual reality.

3.1 Introduction

The proprioceptive sense provides us with information about the posture of our body. Sensory afferent nerves terminating in muscles spindles, joints and skin convey information about the configuration of the limbs and other body parts to the central nervous system (CNS) [47]. This information is also combined with input from vision and other sources [160], aiding sensorimotor coordination, and helping to maintain a body schema, an internal brain representation about how the body is positioned. This information is also instrumental to the planning of motor tasks [161], the perception of our body and the state of the environment around us.

The brain demonstrates considerable flexibility in integrating multisensory information about the body. Prior research indicates that it can take ownership of a wide variety of hand representations [148], an idea that is particularly relevant for first-person virtual reality simulations that represent the hands and fingers. When immersed in virtual reality, users have been reported to experience greater agency over simpler hand representations. This has been attributed, in part, to the brain's sensitivity to position errors in the display of virtual limbs [148]. However, there is little direct evidence about how limb positions are perceived in the presence of visual-proprioceptive mismatches. Because visual and proprioceptive information is integrated in forming estimates of the position of parts of the body [161, 162, 163], it could be deduced that such mismatches might decrease immersion. To date, however, it is unknown how accurately the locations of each of the fingers can be perceived without the use of vision.

Several studies have explored proprioception for the arm by examining the errors that manifest when the arm points to a displayed visual target [164], to a prior location of the hand [165], or to the perceived location of the unseen other hand [166]. All studies reveal large errors in arm localization, in the order of several centimeters. Further studies that have examined proprioceptive errors for various types of visuo-haptic matching tasks show that the observed errors generalize across various experimental designs [167]. Proprioceptive accuracy

is improved if the muscles of the arm are actively engaged in movement [168], which has been interpreted to imply that efferent signals, which command the muscles to move, can enhance proprioceptive performance. Cutaneous manipulations, including skin stretch, have also been shown to influence proprioceptive localization of the limb [169]. Proprioceptive reaching has been shown to utilize both body and gaze-centered reference frames [170]. The proprioceptive map appears to be both idiosyncratic, varying from person to person, and stable, changing little over time [165, 171]. Proprioceptive localization errors for the hands (i.e., limb position) exhibit systematic differences [172, 173], and the errors vary with the posture of the limb [173]. However, it is unknown if these results generalize to the localization of the fingers. None of these studies have characterized the proprioceptive localization of individual fingers. Consequently, other potentially salient factors, such as effects of hand pose on proprioceptive errors in finger localization, have not been previously explored. The fingers are of particular interest because of their important role in performing fine motor tasks, and proprioceptive information in particular has been shown to be utilized in computing joint-based motor commands [174].

In order to characterize multi-digit proprioceptive localization, we designed a study in which subjects reported the perceived positions of their fingertips without visual feedback, using a virtual reality (VR) environment and multipoint tracking system. Several techniques could be used to assess multi-digit proprioception – for example, by asking subjects to evaluate the postural similarity between a virtual hand and their own, or by asking them to judge when the two differed. Here, we assessed proprioceptive localization using a method that is similar to those used in prior studies of limb proprioception [173]. In it, subjects had their hand placed on a table and selected the perceived location of an unseen digit or digits, by guiding a visual cursor to the perceived location in a VR environment that was carefully calibrated to match the real environment. This method was chosen because of its time efficiency, because it provides a direct report of the location of each finger, and because it allowed us to exclude other potential confounds, such as motor or perceptual errors from the contralateral hand. The use of the VR

system provided flexibility in the design of experimental tasks, as evidenced by Experiment 2 below.

In addition to the somatosensory proprioceptive sense, vision also plays an important role in providing information about the body position. Various studies have also explored the integration of visual and proprioceptive cues in the formation of whole limb position percepts [175, 162], or in motion planning and reaching [176, 177, 178], and such studies have informed models for the integration of visual and proprioceptive information [162]. Studies on the rubber hand illusion [179, 180] have also shown that visual information in combination with other cues can cause an adaptation of proprioceptive estimates.

In our daily lives, we routinely encounter situations in which multiple senses are combined. Frequently, this occurs in contexts in which incomplete sensory information is available. For example, a body part may be occluded from view (by the body or another object in the environment), while visual feedback of the adjoining body segments is still available. This is commonly observed in the hand, due to occlusion of the fingers in many practical tasks. Prior literature has provided limited insight into how visual context, in the form of visual cues as to the location of adjacent body parts, affects localization of a visually occluded part, especially for the fingers. In order to assess the influence of this indirect visual information on proprioceptive localization of the fingers, we designed a second study in which we measured how subjects' ability to localize their fingertips was affected by visual feedback about locations of the other fingers.

In the sections that follow, we present a first experiment on the proprioceptive localization of multiple fingers, and a second experiment in which we assess the effect of visual context on proprioceptive localization, in the form of visual cues as to the locations of adjacent fingers. We discuss the findings and their implications for understanding human haptic function, and point toward open questions and potential applications.

3.2 Experiment 1 : Proprioceptive Localization of Fingers

3.2.1 Methods

Subjects

Twelve subjects (8 male; 23 to 33 years of age) volunteered in this experiment. All subjects were naive to the purpose of the experiment. All subjects had (corrected-to-) normal vision, and gave their written informed consent. Two subjects self reported both hands to be dominant, while the rest reported their right hand as the dominant hand. The experiment was approved by the human subjects research review board of the University of California, Santa Barbara.

Apparatus

The experimental apparatus consisted of a computer, virtual reality headset, and multipoint tracking system (Fig. 3.1). Subjects were seated in front of a table and wore a stereoscopic head mounted display (HMD) (Rift, Oculus VR Inc, Menlo Park, CA). The HMD provides stable tracking of the headset in 3D space, accurate to within a millimeter. The HMD displayed a calibrated version of the table in its virtual environment. A careful calibration of the real and virtual environment was performed, by using sensors to select multiple points on corresponding objects with identical dimensions and locations in the real and virtual spaces, and implementing an affine transformation that superimposed the two. This ensured accurate dimensions and placement to within 2 mm. Ground truth positions of the fingers were obtained through six degree-of-freedom wired electromagnetic sensors for position and orientation (Micro Sensor 1.8 and Liberty tracker, Polhemus Inc., Colchester, VT) that were worn on all five fingers and wrist of the left hand, and that were sampled at a frequency of 240 Hz. These sensors tracked finger and wrist locations with sub-millimeter accuracy and without data loss or occlusion. The sensors were attached by means of custom brackets and double sided prosthetic tape.
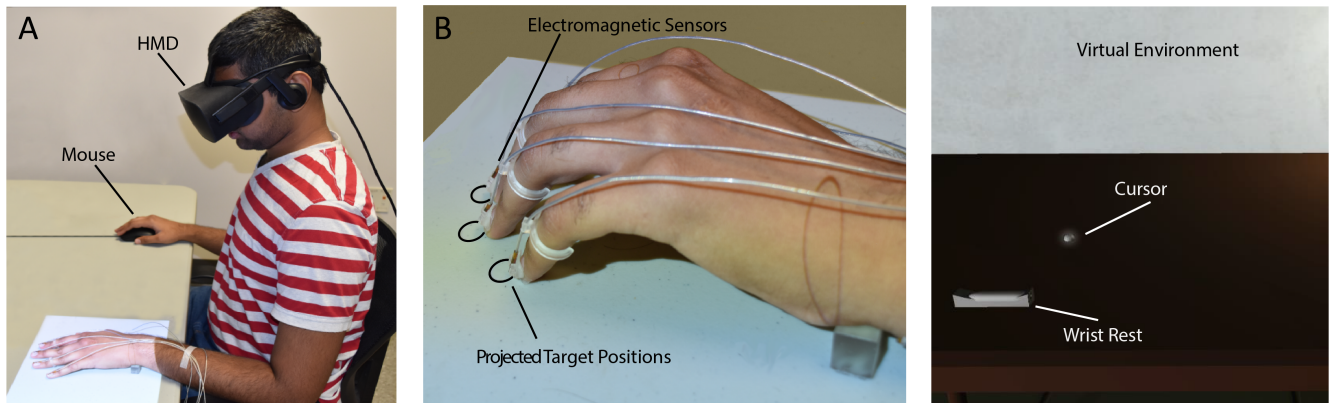
Figure 3.1: A) Experimental System. The subjects left hand was moved to specific hand poses displayed on the table. Subjects used the computer mouse to report perceived positions of their fingertips in the calibrated virtual environment. B) Left hand, showing sensors attached holding a hand pose. C) Displayed Virtual Environment.

Slim, custom brackets were designed and selected to fit the fingernails of each subject and positioned relative to standard anatomical features. Although forces due to the sensors were low, the attachment of sensors to the fingernails via these brackets mitigated cutaneous cues that might otherwise influence proprioceptive judgments [169].

A video projector displayed target positions at computer-specified locations on the table surface, enabling the experimenter to position the subject's hand in each required posture (see Procedure). A wrist rest was fabricated and attached to the table for subjects to place their wrist on during the experiment. A detent in the wrist rest interlocked with a conical bit affixed to the wrist ensuring consistent placement between trials. In all but one of the test conditions, the wrist rest was displayed (at its corresponding location) in the virtual environment. Thus, both visual and cutaneous information about the location of the wrist was available to subjects during the experiment. Visual instructions were provided to subjects via the virtual environment, and a computer mouse enabled them to select perceived fingertip locations.

Target hand poses

Participants hands were positioned in one of five distinct hand poses (P1 to P5; Fig. 3.2), so that we could examine the dependence of proprioceptive errors on finger locations. These poses included a "relaxed" pose (P1), a pose in which all fingers were flexed (P4), and other combinations of flexed and extended fingers. In pose P5, the thumb was flexed inward, towards the palm. The visual display of the wrist rest was included for all these conditions. To examine effects of visual feedback about the wrist position on perceived fingertip location, we repeated pose P1 while omitting the visual display of the wrist rest (P1 without wrist display). Each pose was specified as a set of target positions on the table. These poses were chosen from a subset of possible hand poses constructed by considering two distinct locations for each finger and three distinct locations for the thumb. This choice of poses allowed us to efficiently study the effect of changing the position of the thumb (P1 vs. P5, P2 vs. P3), index finger (P1 vs. P2), and the other fingers (P3 vs. P4).

Prior to the start of the experiment, the length of the subject's hand, from the center of the wrist to the tip of the middle finger, was measured, and the target positions were scaled accordingly. This was done to ensure that subjects maintained similar hand shapes for each pose. In what follows, we refer to the thumb as digit 1, and the little finger as digit 5.

Procedure

At the beginning of the experiment, subjects experienced a familiarization phase, in which sensor data was used to animate a simple representation of the hand, with markers showing the precise locations of the fingertips. Subjects were encouraged to move their fingers and familiarize themselves with the virtual environment and the hand representation, and to convince themselves that it provided an accurate representation of the table in front of them. When subjects indicated they were acclimated, the experiment began. The hand was positioned with the
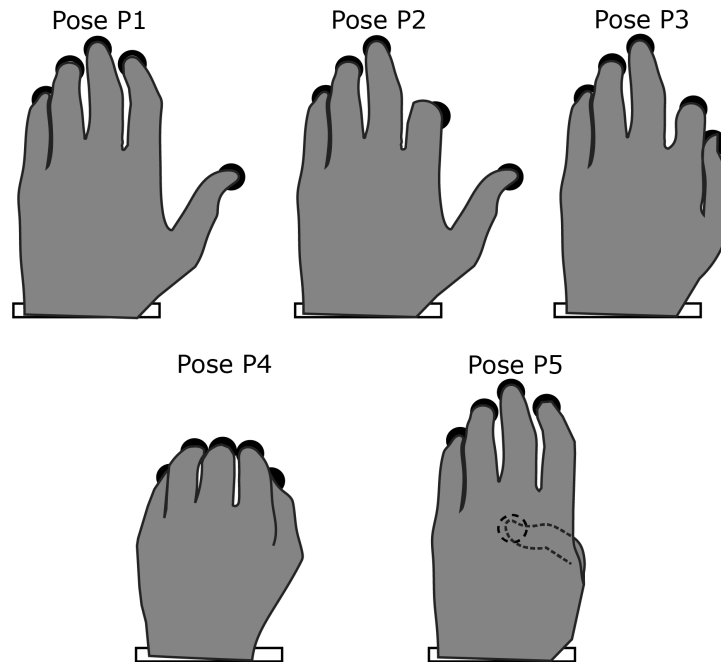
Figure 3.2: Distinct target hand poses used in Experiment 1. P1: Natural resting pose, P2: Index finger flexed, P3: Thumb and index finger flexed, P4: All digits flexed, P5: Thumb flexed inwards. The black circles are the target positions for the fingertips. Dashed strokes are used to represent occluded sections. Note that none of the fingers were touching each other.

wrist on the wrist rest, and the simple hand representation disappeared.

During each trial of the experiment, the experimenter moved the subject's fingers to the hand pose with specified target positions that were automatically projected onto the table, after which the subject held his or her hand at this location. The experimenter ensured that none of the subject's fingers were touching to limit the cutaneous cues available to the subject. The ground truth finger positions were recorded at this stage. The subject could then input a response. A cursor, in the form of a small sphere that was controlled by the mouse appeared at a randomized location. Subjects were prompted to use the mouse and cursor to select and click at the perceived location of each fingertip in sequence, from digit 1 (thumb) to digit 5 (little finger). The cursor was reset to a random location upon each click to prevent starting position bias. Once all positions were reported, a new hand pose was selected, and the next trial started.

Each of the six hand poses was repeated 15 times, for a total of 90 trials per subject. The poses were presented in block-randomized order, with each hand pose presented once within a random ordering, before moving to the next block of six hand poses. The experiment lasted 75 minutes on average for each subject.

Control Experiment

The hand could not be seen during the main experiment, in which participants wore the HMD displaying a virtual environment without any feedback about the positions of the fingers. Thus, the use of proprioception was required in order to report finger position. This reporting was performed within the virtual environment, so that the reported locations may be regarded as proprioceptive estimates in the body frame of reference, translated into the visual frame of reference [181].

In order to rule out the possibility that the measured errors in the primary experiment could be due to errors introduced by the HMD or the experimental design, such as sensor error, display distortion, input errors, scaling errors, object misalignment or other factors, we conducted a control experiment. We quantified errors in a condition in which participants could see their real hand location when reporting positions, by alternating between views of the real environment and calibrated virtual environment. Subjects accomplished this by raising and lowering the HMD until they were satisfied with the reported positions. Four subjects participated in the validation experiment, none of whom participated in the main experiment. Participants were asked to accurately align the cursor in the virtual environment with their fingers. By analyzing the reported finger locations, we determined that the magnitudes of the localization errors, as defined in the analysis below, were small, averaging 0.9 cm. This was strikingly lower than the errors reported in the main experiment, see below. There was no obvious pattern of bias to the resulting data. The errors were similar for all fingers. The error magnitudes obtained in this task were similar in magnitude to values that have been reported for visual estimation errors

for nearby positions in virtual reality [182].

Analysis

The analysis of data from the main experiment compared the reported and veridical positions of the fingertips for each subject in each pose. The veridical and reported positions consisted of vectors in the two-dimensional plane of the surface, $\vec{p}^{\,v}_{i,f,s,t}$ and $\vec{p}^{\,r}_{i,f,s,t}$, respectively. Any errant input of a finger position, as self-reported by the subject during the trial (accounting for $< .5\%$ of all trials), was removed from the analysis. For each subject, finger, hand pose and trial (i, f, s, t respectively), we computed the error vectors $\vec{\varepsilon}_i$ between veridical and the reported positions.

$$\vec{\varepsilon}_{i,f,s,t} = \vec{p}^{\,r}_{i,f,s,t} - \vec{p}^{\,v}_{i,f,s,t} \tag{3.1}$$

The error vectors between the reported and ground truth positions were then translated to ensure that the veridical positions of each individual finger across the trials coincide, to account for any minor differences in the placement of the finger by the experimenter between trials. The errors were quantified by modelling the reported positions for each pose and finger with a bivariate normal distribution. Proprioceptive localization errors can include both systematic and random components. The magnitude of the displacement vector between the distribution mean and the true finger position is defined as $E_{i,f,s}$.

$$E_{i,f,s} = \left| \frac{1}{N_t} \sum_t \vec{p}^{\,r}_{i,f,s,t} - \vec{p}^{\,v}_{i,f,s} \right| \tag{3.2}$$

$E_{i,f,s}$, which is also the magnitude of the mean error vector, reflects the systematic error, or bias in the reported positions. The area of the 95% confidence ellipse, which is the smallest possible ellipse that would be expected to contain 95% of the locations in the distribution, reflects the random errors, or variability in the data [172, 173]. The same error measures were used for the

42

validation experiment.

The magnitude of the mean error vector was averaged across the poses and compared with the mean errors obtained in the control experiment, using an independent-sample Student's t-test. The magnitude of mean error vector and the area of the confidence ellipse were compared between the discrete hand poses (P1 to P5) and digits via 5×5 repeated measures (RM) ANOVA tests. The normality of the data was evaluated using the Shapiro-Wilk test. Greenhouse-Geisser corrections were employed when sphericity was violated, and Bonferroni corrections were applied to the tests. By studying the effect of pose, it is possible to assess the effect of finger position on proprioceptive localization. In these analyses, we assumed that the reported positions for each finger are independent.

To compare the effect of visual information on the location of the wrist, we performed two 2×5 repeated measures ANOVA tests (Pose $\times$ Digit) on the magnitude of mean error vector and the confidence ellipse area data of poses P1 and P1 without wrist display, which differed only in the visual information that was provided about wrist location (via the displayed and felt wrist marker and wrist rest, and interlocking features).

The digit-wrist distance was computed as the distance between the tip of the digit and the center of the wrist, and we calculated the percentage differences between the reported and actual digit-wrist distances. The inter-digit distance was also computed for adjacent digits, and the reported distances were compared with the true distances.

3.2.2 Results

The reported positions and the confidence ellipses for all target positions for two subjects are shown in Fig. 3.3. The observed errors were large, averaging 3.7 cm (range 0.4 to 8.6 cm), and varied with the finger, pose and subject. The positions reported by six subjects for hand pose P1 are shown in Fig. 3.4. Results for a representative subject are shown in Fig. 3.5.
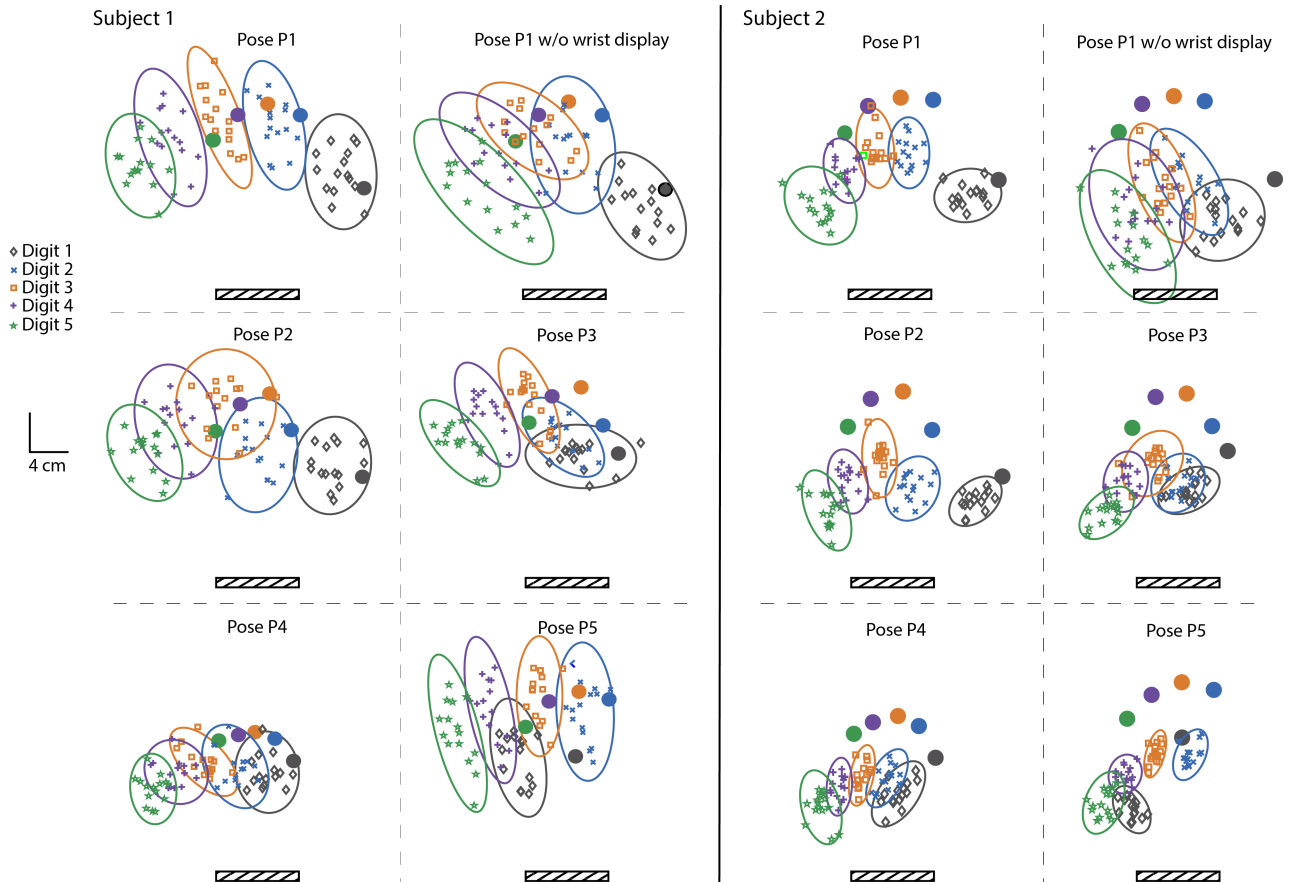
Figure 3.3: Results for each hand pose for two subjects in Experiment 1. The solid circles represent the ground truth positions of each finger, and the hatched rectangle represents the location of the wrist. The reported locations for each individual digit over all trials are represented with a specific marker and color indicated in the legend. The ellipses are the 95% confidence ellipses for the distribution of each digit. The data shows a noticeable bias in the reported positions from the true position. The average error for Subject 1 across all fingers and poses was 4.17 cm (range 2.1-6.6 cm); the average area of the confidence ellipses was 39 cm^2 (range 17-72.4 cm^2). Results from subject 2 exhibited larger errors (mean 5.3 cm, range 2.5-7.8 cm), however localization is more precise than subject 1 (mean area of confidence ellipse 15 cm^2, range 3-50.6 cm^2). Results from subject 1 exhibited a consistent leftward bias in reported locations, whereas subject 2 reported the fingers to be more proximal to the wrist than the veridical positions.

The errors observed in the primary experiment were significantly larger than those in the validation task ($p < 0.001$), at more than 400% as large. This suggests that the observed errors in the primary experiment were likely caused by proprioceptive sensing of finger locations. Thus, the contributions of distortions due to the display, input method, sensing apparatus, and

44
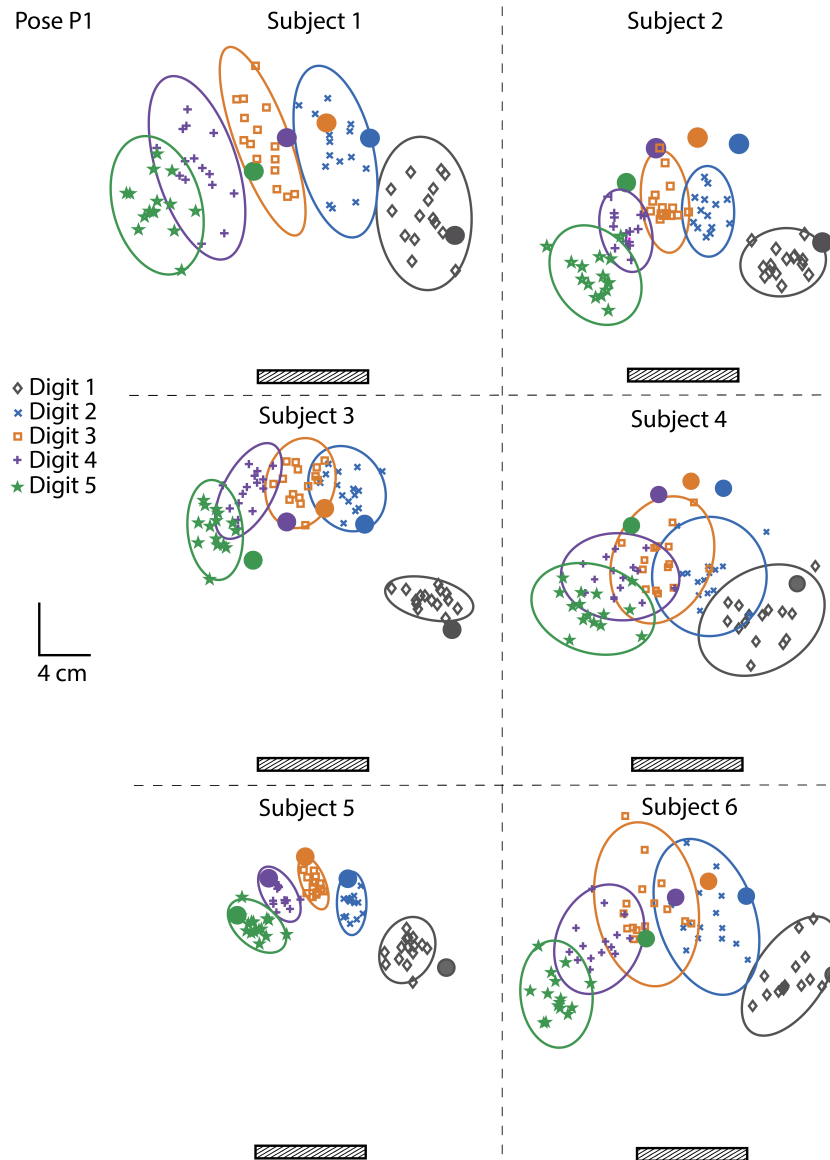
Figure 3.4: Results for hand pose P1 for six subjects in Experiment 1. Subjects 1 and 6 show a consistent leftward bias in reported locations. Subjects 2 and 4 reported the fingers to be more proximal to the wrist than the veridical positions, while subject 3 reported the finger to be more distal. Each subject has a distinct error pattern, which illustrates the idiosyncratic nature of proprioceptive localization.
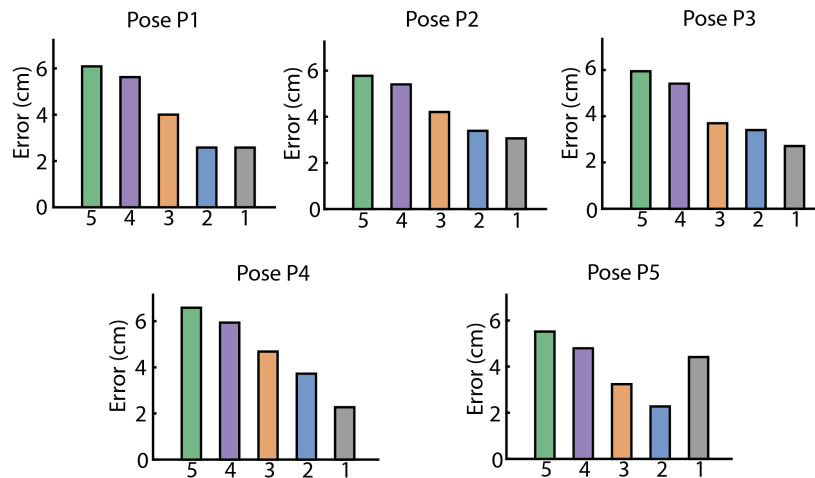
Figure 3.5: Per-finger errors for all distinct hand poses (P1 to P5) for one subject in Experiment 1. The x axis indicates the digits of the hand. For most hand poses (P1 to P4), the localization of the thumb and index finger was the most accurate (mean 2.96 cm and 3 cm respectively), and the errors get progressively larger from digits 2 - 5, with the little finger having the largest errors (mean 5.96 cm). We observed large errors (4.5 cm) in the localization of the thumb in pose P5, when the thumb is placed in an extremely flexed position.

virtual environment calibration likely played a smaller role.

The mean errors for each discrete pose averaged across all subjects are shown in Fig. 3.6. The results of the 5×5 (hand poses P1 - P5 $\times$ digits 1 - 5) repeated measures ANOVA on the errors showed a significant main effect of the digit ($F(1.321, 14.533) = 15.42, p = 0.001$). There was no significant effect of the pose ($p = 0.078$) and no significant interaction between the digit and pose ($p = 0.19$), which precludes within-factors analysis. The pairwise comparisons for digits showed that the errors of the thumb, index and middle fingers were significantly lower than those of the ring and little fingers. The errors of the middle finger were significantly higher from that of the index finger. There were no other significant comparisons (all p's > 0.125).

On comparing the errors for each digit averaged across all hand poses and subjects, we observed that localizations of digits 1 and 2 are generally most accurate (mean error 2.89 cm and 2.81 cm respectively) followed by that of digit 3 (mean error 3.66 cm), while localization of digits 4 and 5 were least accurate (mean error 4.4 cm and 4.7 cm respectively).

The 5×5 repeated measures ANOVA on the area of the confidence ellipse showed no
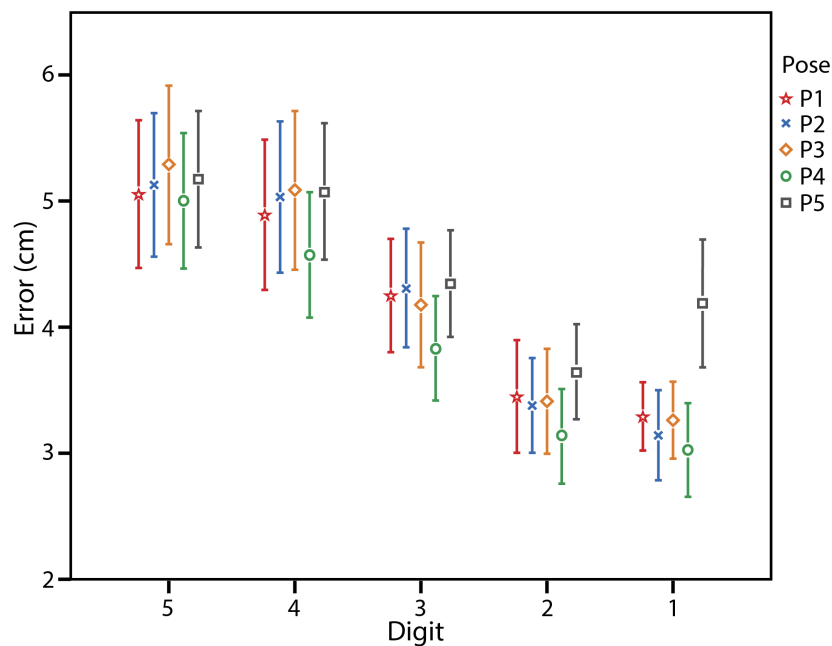
Figure 3.6: Errors for each discrete hand pose (P1 to P5) averaged across all subjects in Experiment 1. The error bars show the Standard Error of the Mean (SEM) across subjects. Error patterns similar to those in Fig. 3.5 were observed, showing that they generalize across subjects. The localization errors of the thumb and index finger were similar, as were the errors of the ring and little fingers.

significant effect of either pose ($p = 0.064$) or digit ($p = 0.14$). There was no significant interaction between the finger and pose ($p = 0.594$). Confidence ellipse areas were smallest for pose P4 (mean 29 cm^2), and largest for pose P1 (mean 43 cm^2). The area of the ellipse was smallest for digit 1 (mean 32 cm^2), and largest for digit 3 (mean 39 cm^2), but these results are not statistically significant.

The errors and areas of the confidence ellipse for poses P1 and P1 without wrist display are shown in Fig. 3.7. The results of the 2×5 repeated measures ANOVA on the errors of poses P1 and P1 without wrist display showed a significant main effect of both the pose ($F(1, 11) = 12.346$, $p = 0.005$) and digit ($F(1.809, 19.9) = 7.12$, $p = 0.006$). There was no significant interaction between the digit and pose ($p = 0.417$). The errors for pose P1 without wrist display were on average approximately 1 cm larger than P1 for all fingers. We observed

47
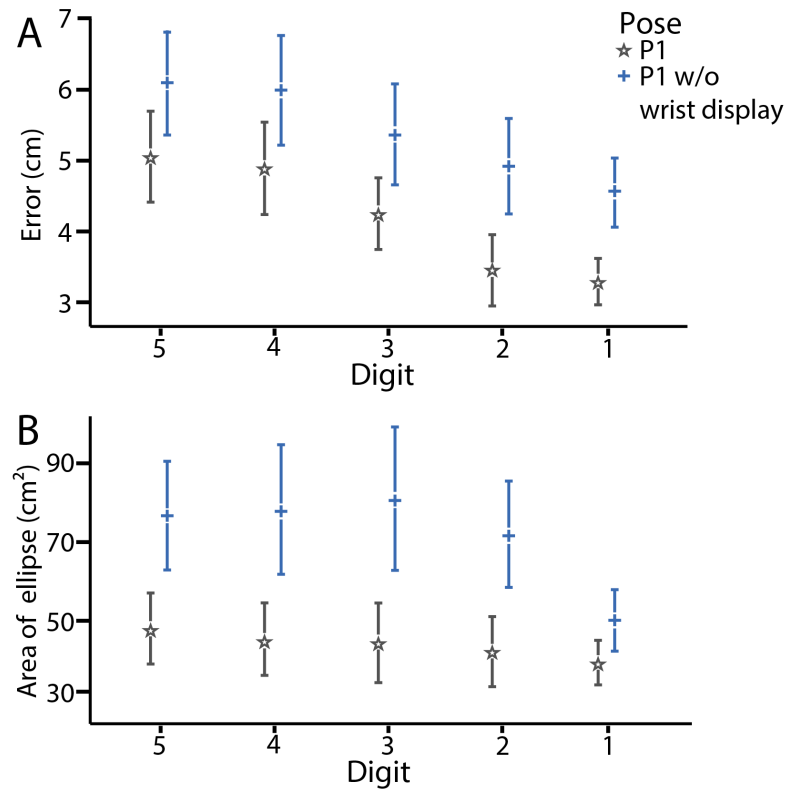
Figure 3.7: A) Errors and B) area of the confidence ellipse for poses P1 and P1 without wrist display, averaged across all subjects in Experiment 1. The error bars show the standard error of mean (SEM) across subjects. The errors for pose P1 without wrist display were on average 1 cm larger than that of pose P1 for each finger. The areas of the ellipse for pose P1 without wrist display were on average 12 cm^2 larger than that of pose P1.

similar per-finger trends in error for Pose P1 without wrist display as the other poses. The 2×5 repeated measures ANOVA on area of the confidence ellipse showed an effect of the pose ($F(1, 11) = 13.65$, $p = 0.004$), but no significant effect of the finger ($p = 0.176$). There was no significant interaction between the finger and pose ($p = 0.059$).

3.3 Experiment 2 : Visuo-proprioceptive integration in localization of fingers

The results of Experiment 1, if taken at face value, suggest that proprioception may provide location information that is too coarse, by itself, to accurately guide performance or learning in normal fine motor tasks, which commonly involve movements coordinated closely between multiple fingers. Thus, we sought to clarify how visual cues are integrated with proprioception in the estimation of finger locations. We hypothesized, and confirmed via pilot testing, that position estimates can be greatly improved if limited visual information about finger position is available, in contrast to the no-vision condition of Experiment 1. Thus, in order to study the integration of indirect visual cues and proprioceptive information in the localization of the fingers, we adapted the method of experiment 1 for a new study in which subjects reported the perceived positions of their fingertips with and without visual indicators as to locations of the other fingers. We also asked subjects to report the estimated position of a fingertip when visual indicators of adjacent fingertip locations were shown and no relevant proprioceptive information was available to the subject (because their hand was placed elsewhere), in order to assess the role of contextual visual information alone in estimating finger locations. In this experiment, we restricted our attention to digits 1 and 2 (thumb and index finger), since they are very commonly used to perform fine manipulation tasks in daily activities.

3.3.1 Methods

Subjects

Eight volunteers (6 male; 24 to 29 years of age) participated in the experiment. Four of them also participated in Experiment 1. All subjects were naive to the purpose of the experiment, had (corrected-to-) normal vision and gave their informed consent. One subject self-reported

both hands to be dominant, with the others reporting their right hand to be dominant. The experiment was approved by the human subjects research review board of the University of California, Santa Barbara.

Apparatus

The experimental apparatus was identical to that used in Experiment 1, except that in Experiment 2, additional visual indicators, in the form of virtual markers (diameter: 8 mm), could be placed at the locations of fingertips.

Target hand Poses

A set of four unique hand poses (P1 to P4) was used (Fig. 3.8A) to discourage memorization of locations. The thumb and index finger were grouped as one unit, with other fingers grouped into another unit. The poses consist of combinations of flexing and extending each unit. Poses were specified as a set of fingertip positions, as in Experiment 1.

Procedure

During each trial of the experiment, the experimenter moved the subject's fingers to the hand pose with specified planar fingertip positions that were automatically projected onto the table, after which the subject held his or her hand at this location. The experimenter ensured that none of the subject's fingers were touching the others to limit the cutaneous cues available to the subject. The fingertip positions were recorded at this stage. A cursor, in the form of a small sphere that was controlled by the mouse appeared at a randomized location. Subjects were prompted to use the mouse and cursor to select the perceived location of the fingertip. Once the position was reported, a new hand pose was selected, and the next trial started.

The experiment consisted of three conditions (P, V, P+V). In the P condition, the perceived location of the fingertip was reported solely through proprioceptive information, and no visual
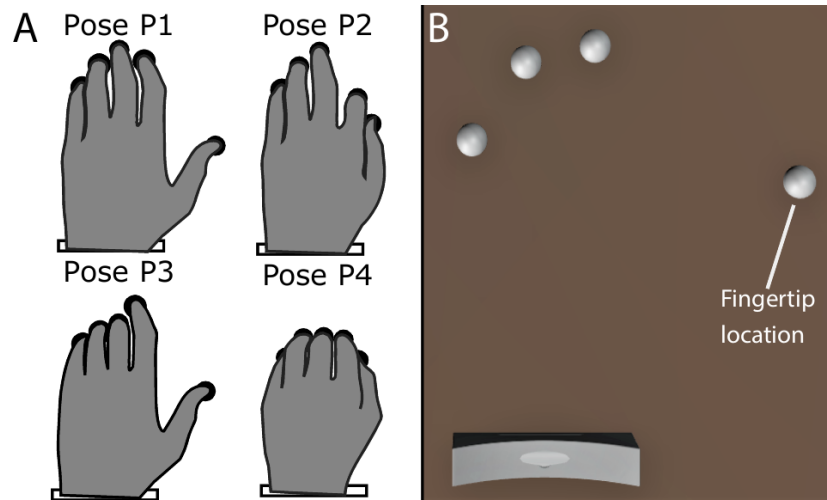
Figure 3.8: A) Target Hand Poses used in Experiment 2. P1: Natural resting pose, P2: Thumb and Index finger flexed, P3: Middle, Ring and Little fingers flexed, P4: All digits flexed. The black circles are the target positions for the fingertips. Note that none of the fingers were touching each other. B) Top view within the virtual environment during one block of the V and P+V conditions, corresponding to Pose P1. The locations of the tips of digits 1, 3, 4, and 5 are shown via the displayed markers. Participants selected a location representing the missing digit. The wrist rest is shown at lower left.

cues are provided. In the V condition, the subject's hand was placed about two feet away from the table by fully extending the elbow joint, thus minimizing the role of proprioception in the task. Visual cues corresponding to the locations of fingertips for a hand holding a pose on the table were shown, with one fingertip location withheld (Fig. 3.8B). Subjects were asked to report their best estimate of the location of the missing fingertip based on the information provided to them. In the P+V condition, visual cues of the location of all other fingertips were provided, and perceived positions were reported using a combination of visual and proprioceptive information. In each block of trials, the subject reported the perceived location of one of either the thumb or index finger per condition, for a total of six blocks (3 conditions × 2 digits). Each of the four hand poses was repeated 15 times in each of the six blocks of trials, for a total of 360 trials per subject. Subjects received short breaks between each block of trials. Within each block, the poses are presented in block-randomized order, with each hand pose presented once within a random ordering, before moving to the next set of four hand poses.

51
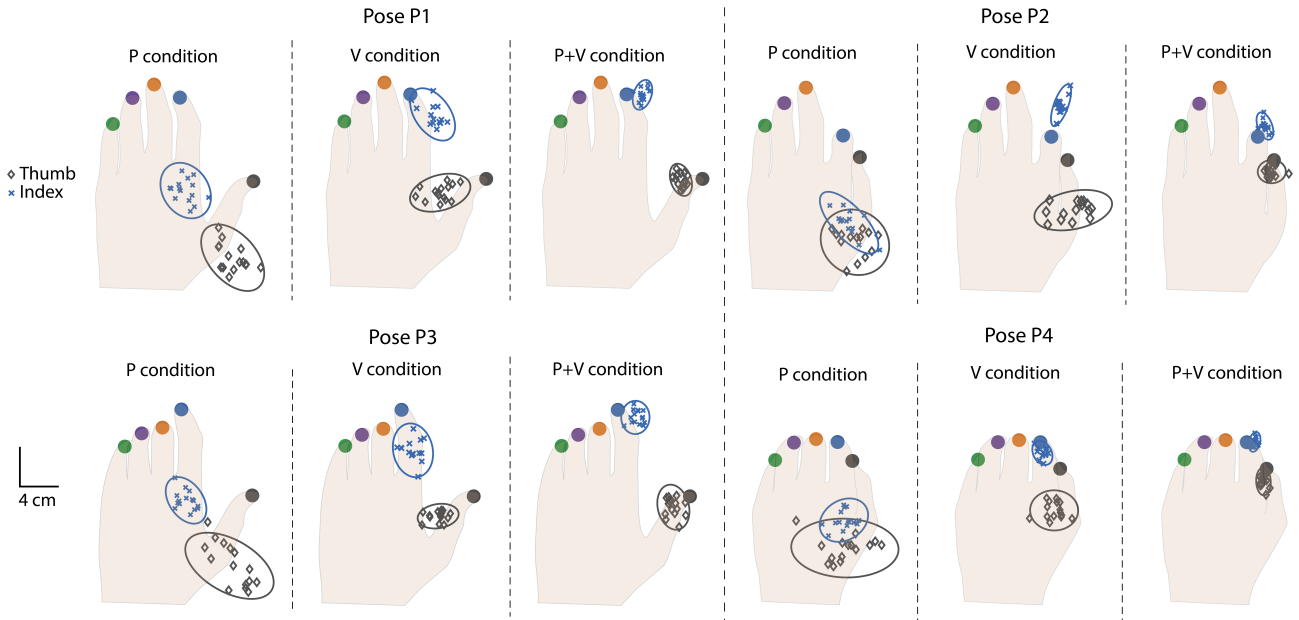
Figure 3.9: Results for all poses and conditions for one subject in Experiment 2. The reported locations for the thumb and index finger for each pose and condition over all trials are overlaid to the same figure and are represented with specified markers. The ellipses are the 95% confidence ellipses. The error averaged over the two digits for the P condition was 7.38 cm, and the average area of the ellipse was 21 cm^2, For the P+V condition, average error was 1.31 cm, and average area of the ellipse was 3.9 cm^2. The subject was able to localize their fingertips more accurately when visual information of all the other fingertips locations were provided (P+V condition).

The experiment lasted 90 minutes on average for each subject.

Analysis

As in Experiment 1, we computed the magnitude of the mean error vector and a 95% confidence ellipse from each distribution of reported positions for the P and P+V conditions. The area A of the confidence ellipse was used to measure the random errors in localization. As multiple poses were utilized primarily to introduce variations in the task, and the results for Experiment 1 did not show a significant effect for pose, the pose was not used a factor for the analysis. The magnitude of mean error vector was averaged over all the poses ($E_{i,f}$) and compared for the P and P+V conditions, for both the thumb and index finger, by performing a

2×2 repeated measures ANOVA tests (Condition $\times$ Digit). Greenhouse-Geisser corrections were employed when sphericity was violated, and Bonferroni corrections were applied for the tests.

The V condition was used to study whether the distributions of finger positions with negligible proprioceptive information and only visual cues (V condition) are combined with the distribution of finger positions obtained through proprioceptive cues (P condition) through linear multi-sensory integration models to obtain the combined percept (P+V condition). For this condition, as the ground truth position of the finger was not well defined, the error magnitude was not calculated. The area of the ellipse was computed in a similar fashion as the other conditions. The area of the confidence ellipse, when averaged over all the poses, was compared for all 3 conditions by performing a 3×2 repeated measures ANOVA tests (Condition $\times$ Digit).

3.3.2 Results

The reported positions and the confidence ellipses for all the conditions and target positions for one subject are shown in Fig. 3.9. The results for errors and confidence ellipse areas averaged across all subjects are shown in Fig. 3.10. Errors were significantly larger in the proprioception (P) condition when compared to the P+V condition (mean error 5.9 cm vs 1.54 cm, $p = 0.001$). The area of the ellipse was consistently larger for the P condition compared to the P+V condition (mean 49.8 cm^2 vs 7.8 cm^2, $p = 0.002$).

The results of the 2×2 repeated measures ANOVA test on the errors showed a significant main effect of the condition ($F(1, 7) = 31.684$, $p = 0.001$), and no significant effect of the digit ($p = 0.453$). There was no significant interaction between the condition and digit ($p = 0.39$), which precludes within-factor analysis. Post-hoc pairwise comparisons for the condition showed that the errors for the P+V condition were significantly lower than those for the P condition ($p < 0.001$).
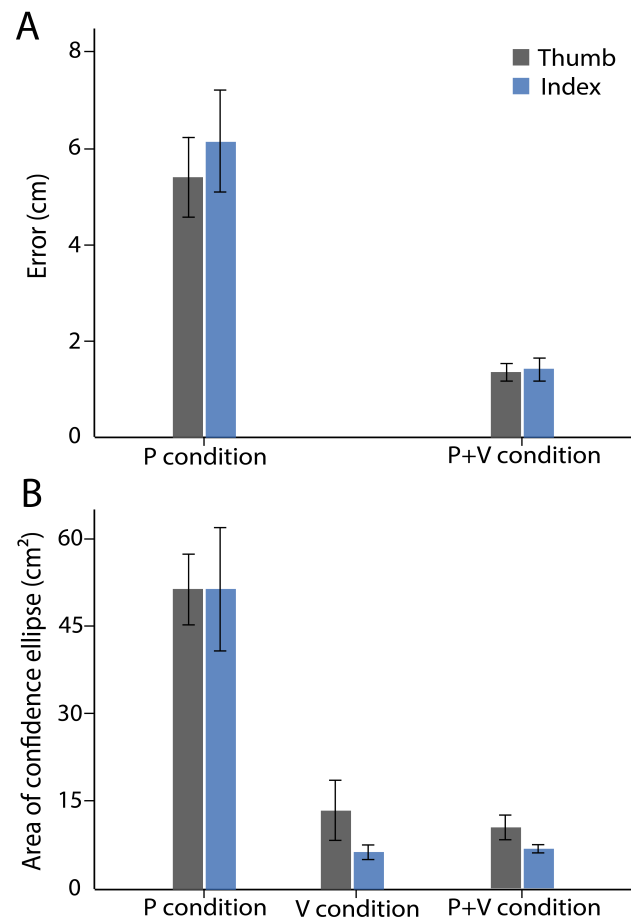
Figure 3.10: A) Errors for the P and P+V conditions, for thumb and index finger, for all subjects in Experiment 2. B) Area of the confidence ellipse A for the P, V and P+V conditions, for thumb and index finger, for all subjects in Experiment 2. Error bars show the standard error of mean (SEM) across subjects. The localization accuracy in the P+V condition was significantly better than that obtained through either vision or proprioception alone. The random errors of localization in the P+V condition was significantly lower the P condition, but not the V condition.

The results of the 3×2 repeated measures ANOVA test on the area of the confidence ellipse showed a significant main effect of the condition ($F(2,6) = 27.1$, $p < 0.001$), and no significant effect of the digit ($p = 0.097$). There was no significant interaction between the condition and digit ($p = 0.41$). Post-hoc pairwise comparisons for the condition shows that the areas for the P+V condition were significantly lower than those for the P condition ($p = 0.002$), but not significantly different from the V condition ($p > 0.5$). Further, the areas of

the confidence ellipse for the V condition were significantly lower than those of the P condition ($p = 0.004$).

3.4   Discussion

The goal of Experiment 1 was to investigate multi-finger proprioceptive localization. We found the systematic errors (bias) and random errors in finger localizations to be large, implying that proprioceptive localization is neither very accurate nor precise compared, for example, with the typical length of the finger.

Our results suggest that the random errors of proprioceptive localization are similar for each finger. The systematic errors were smallest in magnitude for digit 1 and 2 (the thumb and little finger) and became progressively larger for subsequent digits, including digit 5 (little finger). The thumb and index finger are highly individuated and frequently used in precision grasping and manipulation. Consequently, it would appear that these estimates have developed to be the most accurate. The origin of large biases in proprioceptive estimates of finger locations is unclear. Plausibly, these positions could be calibrated through inputs from the visual system [183, 184], but it appears that large biases are allowed to persist.

While the dependence on pose was not significant, the mean errors and confidence ellipse areas were lowest for pose P4, in which all fingers were flexed and the fingertips were closest to the wrist. The errors for the thumb were largest when it is at its most extreme position in pose P5. This suggests that, similar to proprioceptive localization of the whole limb [164, 165], proprioceptive localization of the fingers is more accurate for fingers that are closer to the body. An examination of the errors for pose P6 also shows that our effort to prevent accumulation of errors in the reporting for subsequent digits by randomizing the cursor location was successful, as the errors for digits 2 - 5 in this pose were not significantly influenced by the large errors of the thumb. This suggests that the reporting of finger locations was not dependent on previously

reported positions.

The observed patterns of the systematic errors appeared to be idiosyncratic, and to vary across subjects, as illustrated in Fig. 3.4. The reported positions for various subjects differed both in error magnitude, and in the direction of the error patterns. We did not observe any systemic drift in proprioceptive estimates of finger locations for any pose over the course of either experiment (which lasted for a maximum of 100 minutes). In informal testing, we have observed that the error patterns remain consistent over the course of several weeks. This suggests that while the trial-to-trial variability in estimates is large, the proprioceptive map of the entire hand may remain stable, although further research is needed. These findings are analogous to those of prior studies that have shown that proprioceptive localization of the whole arm is idiosyncratic and stable [165, 171]. Informal testing also revealed similar patterns of errors for other reporting methodologies and hand positions, including methods which did not use a virtual environment.

The errors for all of the fingers were similar in magnitude to those that were reported for proprioceptive localization of the whole arm (3 to 6 cm) [164, 166, 171], even when the position of the wrist was displayed and was felt at the same location; this was true for all poses except P1 without wrist display. We had hypothesized that when the location of the wrist was displayed, the brain would be able to incorporate this knowledge to greatly aid the location estimates of the fingertips, making them more accurate, as the location of the arm would not need to be independently estimated. Based on the accuracy of fine motor behavior and that of various perception tasks (such as precision grip aperture size estimation), we had expected these errors to be on the millimeter scale. However, we observed that localization errors remained large (2.8 to 4.8 cm) when the wrist location was shown, and that the error patterns were similar to those we observed without this information. The magnitudes of the errors are especially striking when we consider that the average length of the hand is only 18 cm, and the average width only 10 cm. This could indicate that the brain does not use prior knowledge of parts of the body

to directly refine proprioceptive estimates, suggesting that there exists in the CNS independent body schemas obtained through vision and proprioception, information from which would be combined to give position estimates, akin to the modular theory detailed by Tagliabue et al. [185]. A statistical comparison of the results for poses P1 and P1 without wrist display, which differ only in visual information about the wrist, does indicate that errors increased significantly in magnitude ($p = 0.005$) when the wrist location was not shown, but those errors were only 1 cm larger on average. This difference is much smaller than the errors in localizing the wrist. We hypothesize, based on post-experiment written reports of the subjects, that one of the reasons why both the errors and the confidence ellipse areas of pose P1 were smaller than those in P1 without wrist display was because subjects could notice that a proposed finger location estimate was implausibly close to the displayed location of the wrist for pose P1, which could affect their reported positions. In short, the effect of visual information about wrist location was significant, but small, contrasting with the larger effects observed in Experiment 2, as discussed below.

In Experiment 1, we also observed that the mean position estimates were more proximal to the wrist than the veridical fingertip locations, with digit-wrist distances being underestimated by 10% on average. The distances between the tips of digits 1 and 2 (thumb and index finger) are underestimated by 12%, while the 2-3, 3-4, and 4-5 inter-digit distances are overestimated by 28%, 46% and 13% respectively. This may suggest that the implicit map of the hand generated from proprioception is distorted from the true shape of the hand. The results are similar, in this respect, to those reported by Longo and Haggard [186] who found that the implicit hand representation for a single hand pose was widened (mean 67% overestimation of distance between knuckles) and shortened (mean 28% underestimation of finger length). From the results of pose P5, we observe that the inter-digit distance may generally depend on the pose of the hand. This distorted hand shape is also apparent when examining the results of many individual trials, possibly suggesting that an internal representation of the hand was employed in the

perceptual task. This raises the question of whether proprioceptive estimates for each finger are independent. We explored this question by computing the standard deviation of the inter-digit distances across trials, the average of which was 1.2 cm. This result is larger than that expected if the reported positions for each finger were fully correlated, but is only marginally larger than the errors observed in our control experiment. This question would therefore necessitate a more focused study than ours to conclusively answer.

In Experiment 2, we observed that the localization in the "vision only" condition involves very small random errors, which seems to indicate that our subjects had a very precise visual estimate of where the finger could be positioned based on visual cues. The results for the "proprioception + vision" condition show that visual cues indicating the positions of adjacent fingers can greatly affect localization of unseen digits. Both random and systematic errors of localization improved significantly when this indirect visual information was available. This suggests that even partial visual information can greatly aid localization of the fingers. Such partial visual information could be available in conditions in which some digits are occluded from view, such as during object grasping and manipulation, or when visual attention is constrained. Thus, despite the limitations of proprioceptive sensing that this study brings to light, it can be improved by indirect visual cues; in our experiment, the mean errors and confidence ellipse areas declined to 1.54 cm and 7.8 cm^2 respectively with this information. This suggests that proprioceptive information about finger position, however coarse, may aid manual activities, although further research is needed in order to assess this in more complex and dynamic tasks, where proprioception may become more accurate, due to active movement.

As illustrated in Fig. 3.9, the position estimates in the condition in which both proprioception and visual cues were available did not generally lie between the estimates obtained separately in each unimodal condition. For this reason (as further reflected in our analyses), the results observed would not be consistent with models of multisensory integration that involve a weighted combination of unimodal estimates, such as simple linear weighted cue combina-

tion models, or maximum likelihood models, although other models of cue integration may be consistent with these findings. However, we note that in the "vision only" condition here, in addition to vision, participants also had access to (conflicting) information from proprioception from their hand, which was resting elsewhere. Thus, even though participants were instructed to ignore this proprioceptive sensory input as "irrelevant", it is unclear how it may have affected their responses. Further research is needed in order to clarify the integration of direct or indirect visual cues and proprioceptive information in the localization of the fingers.

3.5 Conclusion

In this study we investigated the proprioceptive localization of multiple fingers of the hand using somatosensory information alone, and in combination with visual cues as to the locations of the other digits. Proprioceptive position estimates exhibited large random and systematic errors. The latter were on the order of several centimeters. This was true even when the location of the wrist is displayed. Participants did not fare much better at locating their fingers relative to their wrist than they have been reported to do at locating the wrist itself. The observed errors were finger-dependent, with the localization of the thumb and index finger being most accurate. The hand shape implied in the data would be compatible with an internal representation that is biased and distorted, consistent with prior research, but which may be well maintained over time. When visual cues as to the locations of adjacent fingers was available, the errors decreased markedly. This suggests that the perceptual system is able to integrate bimodal information to improve position estimates even when body parts are occluded.

The results of this research suggest that the perceptual system can integrate discordant representations of finger position. This may be important for the sensorimotor control of grasping. It also suggests that in applications such as human-computer interaction or virtual reality, users may be able to accommodate large visuo-haptic discrepancies in finger position, which may

facilitate new interaction techniques, rendering methods for representing the hands, or other interesting effects.

Chapter 4

Rendering Spatiotemporal Haptic Effects via the Physics of Waves in the Skin

In the domain of haptic engineering, there have been intense efforts to identify methods that can stimulate the skin across its entire spatial extent. This chapter contributes to this body of research by first presenting measurements which elucidate the distribution of mechanical energy in skin when driven by haptic actuators, identifying a powerful concept: frequency-dependent damping of propagating mechanical waves in the skin. These findings are used to construct a new class of haptic feedback that utilizes spectral methods to control the spatial extent of sensations. These haptic effects are perceived as spatially varying over large regions of the skin, even when presented using a single actuator. These effects are shown to result in more engaging interactions when employed in a virtual reality setting. This research presents a particularly efficient method to stimulate large areas of the skin with a limited number of actuators.

The content of Chapter 4 is adapted from the following reference [12] :

B. Dandu, Y. Shao, and Y. Visell. "Rendering Spatiotemporal Haptic Effects Via the Physics of Waves in the Skin." in *IEEE Transactions on Haptics*, vol. 14, no. 2, pp. 347-358, 1 April-June

Abstract

A major challenge in haptic engineering has been to design practical methods to efficiently stimulate distributed areas of skin. Here, we show how to use a single actuator to generate vibrotactile stimuli which cause sensations of temporally varying spatial extent. Through optical vibrometry methods, we show that vibrational stimuli applied at the fingertip elicit waves in the finger that propagate proximally toward the hand and show how the frequency-dependent damping behavior of skin causes propagation distances to decrease rapidly with increasing frequency of stimulation. Utilizing these results, we design haptic stimuli applied through a single actuator that produces wavefields that expand or contract in size. In a perception experiment, participants accurately (median >95%) identified these stimuli as expanding or contracting without prior exposure or training. As a potential application, we used these effects as haptic cues for interactions in virtual reality. We show through a second experiment that the spatiotemporal haptic stimuli were rated as significantly more engaging than conventional vibrotactile stimuli. These findings demonstrate how the physics of waves in skin can be utilized to excite spatiotemporal tactile effects over large surface areas with a single actuator, and inform methods to utilize the effects in practical applications.

4.1   Introduction

Our skin is an exquisitely sensitive distributed sensory medium which provides a rich source of information about the world around us. Tactile interactions excite the skin in a complex fashion due to its intricate structure and many mechanical degrees of freedom, and

this is then filtered by the perceptual system to ascribe a meaning to it. A major challenge in haptic display engineering is to find methods for efficiently stimulating this large continuous medium with practical devices containing a limited number of actuators.

It has long been observed that locally applied stimulation of the skin evokes distributed mechanical waves [187, 188, 55] which propagate through the ridges in the epidermis and multiple tissue layers in the dermis. These are then transducted by various classes of embedded mechanoreceptors serving different perceptual functions, each with distinct distribution densities, spatial and temporal resolutions, and sensitivity properties [189, 188]. In particular, for the perception of vibrations, the Meissner and Pacinian corpuscles (FA-I and FA-II afferents respectively) are of primary importance. Information from the receptors are translated by the nervous system to synthesize what we feel[37]. The somatosensory specializations of the receptors such as the large receptive fields associated with Pacinian Corpuscle (PC) afferents [190, 36] can be partly explained by these wave processes, which are an essential component in the mechanism of touch perception.

While touch sensations are often assumed to be localized to the region of stimulation, excited mechanical waves in the skin can propagate to reach remote locations at amplitude levels higher than perceptual thresholds [51, 50, 191, 192], and research has shown that these can indeed be utilized by the perceptual system [53]. The extent of propagation is determined primarily by the mechanical properties of human skin and its structure. Studies have shown that the skin on the finger can be considered a linear propagation medium, except in irregular regions such as the folds of the joints [193]. Further, the glabrous skin on the hand has been shown to have significant mechanical differences from hairy skin [55]. In addition to the anatomy and mechanics of the skin, the propagation of these waves has also been shown to depend on the properties of touched objects, the locations of contact with the skin, posture of the hand, contact force, and the frequency content of tactile inputs [50, 51, 194, 195]. To date, the influence of propagating waves on tactile perception is not fully understood. While the

transmission of vibrations in the skin has been considered to affect the performance of haptic devices [55], there have been limited instances where they are accounted for, or utilized in the design of devices [196, 197].

One sub-class of haptic display devices consists of those that generate tactile motion effects. Spatiotemporally varying haptic motion effects have been previously been utilized as a means to enhance user experiences and immersion in games and movies in conjunction with tightly coupled visual cues of movement[5, 198]. Such effects can allow for improved information transfer through the haptic modality, and have been used to provide haptic guidance and directional information [199, 200], enable rich notifications [201], and to create a communication method for the deaf-blind [122].

Prior efforts to stimulate the skin to obtain spatiotemporal tactile effects have often focused on using dense arrays of actuators stimulating local regions of the skin, which require significant bulk and complexity, and impose large barriers for adoption. Through the years, several spatiotemporal vibrotactile perceptual phenomena, including apparent motion, saltation, funneling, and contrast phenomena have been discovered, [202, 203, 204, 72, 75], and utilized to render smooth tactile motion effects on various regions of the body more efficiently [205, 5, 206, 207]. Such effects often reflect the spatiotemporal integration of cutaneous vibrotactile stimuli that are (in most cases) applied at multiple skin locations. However, such rendering methods utilizing perceptual phenomena still require multiple actuators, and it remains a challenge to achieve spatiotemporal effects over large areas of the skin with a single actuator.

The present work is inspired by research on cochlear auditory processing for which von Békésy received the 1967 Nobel Prize [208]. Using methods analogous to those we employ here, he combined optical measurements of basilar membrane vibrations with mechanical modeling to deduce that the selective transmission of lower frequency waves to greater distances provides a tonotopic spatial mapping in the basilar membrane. This mechanical process was

shown to underly frequency encoding in early auditory processing. Analogously in the vibrotactile system, the frequency-dependence of the damping and wavespeeds of mechanical waves in the skin have been deduced to give rise to distinct population responses in cutaneous mechanoreceptors [50] and consequently provide a frequency encoding method, but the full implications of this frequency dependence for tactile perception are not yet fully understood.

Here, we present a new method for rendering spatiotemporal haptic effects via a single vibrotactile actuator. Our method exploits the viscoelastic properties of skin, which cause induced propagating vibrations to decay in a frequency-dependent manner. We hypothesized that by varying the frequency content of locally applied vibrotactile signals, we could control the spatial extent of propagating waves they excite in the skin. We then hypothesized that using this method, vibrotactile stimuli provided by a single actuator could be designed to elicit spatiotemporal haptic effects.

In the sections that follow, we first provide a physical description for the frequency-dependent transmission of the mechanical waves in skin induced by vibrotactile stimulation. We then empirically assess the propagation of these waves using in-vivo measurements captured via optical vibrometry, and show that the frequency content of locally applied vibrotactile stimuli determines their spatial extent in the skin, with low frequencies propagating greater distances. To demonstrate the utility of these results for haptic display engineering, we then design vibrotactile stimuli that excite spatially expanding or contracting fields of vibration in the skin. In a perception experiment, we demonstrate that participants perceive these stimuli as expanding or contracting, without prior exposure or training. We used these to design visuo-haptic effects for virtual reality, and show through an evaluation experiment that the spatiotemporal haptic effects are rated to result in a more engaging experience over the use of conventional vibrotactile stimulation. We then present some potential applications. These results expand the repertoire of vibrotactile feedback that can be delivered by a single actuated degree-of-freedom, and suggests new practical approaches for haptic virtual and augmented reality and new methods for

haptic feedback in human-computer interaction.

4.2   Viscoelastic Waves in the Skin

Touch sensations arise from mechanical stresses and strains in the skin which are trans-
ducted via numerous cutaneous afferents situated within the dermis and subdermal connective
tissues. After the application of a tactile stimulus, the strains propagate through the medium.
An idealized physical model for the response of the system for a driving force field $\boldsymbol{f}(\mathbf{x}, t)$,
assuming the skin as a homogeneous medium and subject to boundary conditions, is given by
the elastic wave equation,

$$\boldsymbol{f}(\mathbf{x}, t) = \left(- \rho \frac{\partial^2}{\partial t^2} + ((K + \mu/3)\boldsymbol{\nabla})\boldsymbol{\nabla} \cdot + \mu \nabla^2 \right) \boldsymbol{\xi}(\mathbf{x}, t) \tag{4.1}$$

where $\boldsymbol{\xi}(\mathbf{x}, t)$ is the time varying displacement vector field, $\mathbf{x}$ is position, t is time, ρ is density
of the material, and K and μ are the bulk and shear moduli respectively [209]. The solutions
for this equation may be expressed as expansions in harmonic plane waves,

$$\boldsymbol{\xi}(\mathbf{x}, t) = e^{j(\mathbf{k} \cdot \mathbf{x} - \omega t)}$$

where $\omega = 2\pi f$ is the angular frequency and $\mathbf{k}$ is the wave vector. The wave velocity is
specified as by $\mathbf{v} = (\omega/|\mathbf{k}|)\hat{\mathbf{k}}$. The solutions can be further be decomposed into transverse (shear)
and longitudinal components. Shear waves $\boldsymbol{\xi}_T(\mathbf{x}, t)$ satisfy $\mathbf{k} \cdot \boldsymbol{\xi}_T = 0$, while longitudinal waves
$\boldsymbol{\xi}_L(x, t)$ satisfy $\hat{\boldsymbol{k}} \times \boldsymbol{\xi}_L(x, t) = 0$. Shear waves travel at speeds $c_T = \sqrt{\mu/\rho}$, while compression
waves travel at speeds given by $c_L = \sqrt{(K + 4\mu/3)/\rho}$. For soft tissues, the shear wave speeds
($c_T < 30$ m/s), are much lower than those of compression waves ($c_L > 1500$ m/s) [187, 210].

At vibrotactile frequencies (< 1000 Hz), mechanical transmissions in the bulk of the
medium occurs primarily via shear waves. Such waves appear to travel in soft tissues rather

than via bone [51, 187], but the relative contribution of tissue types (including dermis, tendon, and muscle) is unclear. In contrast, compression waves are the dominant mode of energy transmission at higher frequencies ($f > 10^4$ Hz).

Experimental observations [50, 51] and mechanical considerations suggest that at most stimulation frequencies near the skin surface, a mixing of shear and compression waves yields surface waves (including Rayleigh and Love waves) with speeds similar to those of bulk shear waves [211]. These waves propagate exponentially with depth z, over a distance on the order of one wavelength (wavelengths λ of the order of 1 cm in skin for vibrotactile frequencies). In contrast, they propagate more efficiently over long distances on the surface and outer layers of the skin as compared to bulk waves.

The skin and soft tissues exhibit viscoelastic properties, and waves in such tissues are damped and dispersive, yielding frequency-dependent damping $\delta(f)$ and wave-speeds $c(f)$ [211, 50, 212]. In biological tissues, damping can arise from thermal (absorption) and acoustic (dissipation) processes, with the latter expected to dominate at vibrotactile frequencies. In a linear viscoelastic model, damping imparts complex wavenumbers, $k = k_1 + i\delta$, to harmonic plane wave solutions, where δ, is the damping factor, and $k_1 = 2\pi f/c(f)$. The damping term δ can be considered a function of frequency $\delta = \alpha(f)$. Harmonic components in one dimension thus satisfy

$$\boldsymbol{\xi}_f(x,t) = e^{-\alpha(f)x}e^{j2\pi f(x/c(f)-t)} \tag{4.2}$$

This describes an oscillating wave that decays exponentially with distance from the driven location.

An arbitrary plane-polarized wave has a Fourier expansion,

$$\boldsymbol{\xi}(x,t) = \int_{-\infty}^{\infty} df \ \phi(f)e^{-\alpha(f)x}e^{j2\pi f(x/c(f)-t)}. \tag{4.3}$$

Here, $\phi(f)$ is the amplitude and phase of an individual frequency component f. Because the amplitudes are small and the system is linear, there is no mixing between frequency components. Each frequency component decays exponentially with distance, with the decay factor being a function of frequency. The distance at with the energy of a frequency component wave decays to a fixed percentage of the amplitude at $x = 0$ is specified by $x_D = (\alpha(f))^{-1}$ Thus, the relative weighting in $\phi(f)$ of low and high frequency content in the solution determines the distance that a propagating wave is expected to travel before attenuating. This suggests that the spatial extent of vibrotactile stimuli is greatly affected by their frequency content. If damping increases monotonically with frequency, $d\alpha/df > 0$, this would cause higher-frequency waves to attenuate out over a shorter distance than lower frequency waves. We test this prediction using vibrometry experiments, and use it to guide the design of spatiotemporal haptic effects.

4.3   In-Vivo Vibrometry Experiments

We assessed the frequency-dependence of the spatial propagation of vibrations in the hand via time-resolved optical vibrometry. This provided non-contact measurements of skin vibrations at numerous points on the glabrous hand surface in response to vibration inputs applied to the distal end of the finger. We analyzed this data to relate the frequency content of the stimuli to the spatial distribution of skin vibrations they excited in the hand.

4.3.1   Participants

7 participants volunteered for the experiment (5 male; 20 to 45 years of age). All gave their informed, written consent. The experiment was approved by the Human Subjects Committee of the University of California, Santa Barbara.
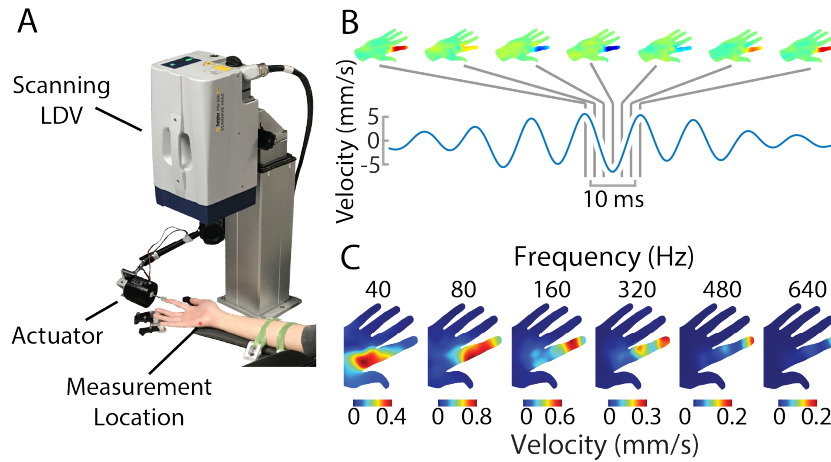
Figure 4.1: A) Measurement Apparatus. Hands were positioned within the field of view of the SLDV, which captured the velocity of skin vibrations across the entire volar hand surface in response to stimuli applied at the tip of digit 2. B) The stimuli elicited propagating waves in the skin. The data comprises of one trial for one participant, with the 80 Hz windowed stimulus. C) The RMS velocity of skin oscillations illustrate the frequency-dependent spatial extent of the wave fields elicited in the skin (shown here for one participant). Low frequencies stimuli excited waves that extended farther in the finger.

4.3.2 Apparatus

We captured cutaneous vibrations via a 1-axis non-contact scanning laser doppler vibrometer (SLDV; model PSV-500, Polytec, Inc., Irvine, CA). The right hand of each participant was positioned within the SLDV field of view. The hand was stabilized in an open posture via custom 3D printed brackets affixed to five fingernails via adhesive tape (Fig.4.1). The arm, hand, and brackets were supported via a pneumatically-isolated table. Participants were seated in a reclined chair raised to a height at which their arm could remain relaxed.

Vibration stimuli were applied normal to the tip of digit 2 along the axis of the finger via an electrodynamic actuator (Mini Shaker Type 4810, Brüel & Kjær, Denmark) driven by a laboratory amplifier (PA-138, Labworks Inc.). Prior to the experiment, we measured the frequency response of the amplifier-actuator system to be flat over the entire measurement range ($\pm$ 3 dB). The finger was attached to the actuator along a 49 mm^2 interface via adhesive tape to prevent the skin from decoupling during actuator retraction.

4.3.3   Stimuli

Two types of vibration stimuli were applied via the actuator: sinusoidal signals with linearly swept frequency variation, and windowed sinusoidal signals at discrete frequencies. The driving signals were generated by the PSV-500 system, ensuring sample-accurate synchronization of the driving signal with the measurement. The frequency sweep extended from 20 Hz to 1000 Hz. The frequencies of the windowed sinusoidal signals ranged from 40 Hz to 640 Hz in steps of 40 Hz. To avoid transient artifacts, we applied a Hanning window function to each sinusoid, with a duration of 10 cycles (thus, longer for low frequency signals). To avoid interference between different stimuli, a pause of 150 ms was enforced between measurements [51]. Amplitudes were selected to provide sufficient signal-to-noise ratio and to be comfortable even during extended stimulation.

4.3.4   Procedure

After each participant was seated at the apparatus, a 3D scan of the volar hand surface was performed via the integrated geometry scan unit of the SLDV. Vibrometry measured the velocity of skin motion normal to the volar hand surface at 300 points that were equally distributed across the surface. We selected this spatial resolution because we estimated it to be approximately $10\times$ finer than the wavelength of cutaneous vibrations in the tested frequency range. A range setting of 250 mm/sec was used for the vibrometer, to ensure that high amplitude vibrations at all points on the skin were measured without distortion. The measurement sampling frequency was 20 kHz.

For each scanned measurement point, the finger was presented with all stimuli while data was collected at the measurement point. The vibrometer captured the vibration velocity in a direction normal to the volar hand surface. The experiment took a total of 80 minutes per participant.

4.3.5 Analysis

The data consisted of velocity signals describing skin vibrations at 300 measured locations for each of the 16 signals and 7 participants. We analyzed skin vibrations at different frequencies using the frequency sweep signals, which we used to reconstruct the time domain mechanical response at different frequencies. We then computed root-mean-squared (RMS) averages for each measurement trial, frequency, and participant. This yielded RMS velocities $v(\boldsymbol{x})$ at the 3D positions $\boldsymbol{x} = (x_1, x_2, x_3)$ of all measurement locations. To assess the spatial extent of skin vibrations elicited for different stimulus frequencies, we evaluated the RMS velocities v_{rms} along a straight line extending from the contact location of the actuator to the the base of the hand. For each frequency, velocity values at 200 points on this line were computed via interpolation. For each frequency f, we computed the median spatial extent of skin vibrations as the the distance $D(f)$ up to which the signal energy reached half of the total, averaged across all participants. Due to the oscillatory nature of the measured waves, the median spatial extent provided for a more accurate model of the decay of energy in the system. We fit $D(f)$ to a power law, $D(f) = c_1 f^{-c_2}$, where c_1 and c_2 were the fitting parameters.

4.3.6 Results

The results indicate that stimulation at the fingertip elicited time-dependent wave fields that reflected the stimulation frequency (Fig. 4.1C, 4.2) and extended proximally from the fingertip (Fig. 4.1B), reaching the palmar surface within 10 ms.

Consistent with predictions from wave mechanics, the vibration-elicited waves typically decayed with distance from the stimulation point, in a frequency-dependent manner (Fig. 4.2, 4.3). For all participants, the highest frequency stimuli (f=640 Hz) elicited cutaneous waves of greatest amplitude (velocity, m/s) near the point of application at the fingertip, decayed rapidly over the course of 40 mm. Near the base of the finger, 80 mm distant, these vibration velocities
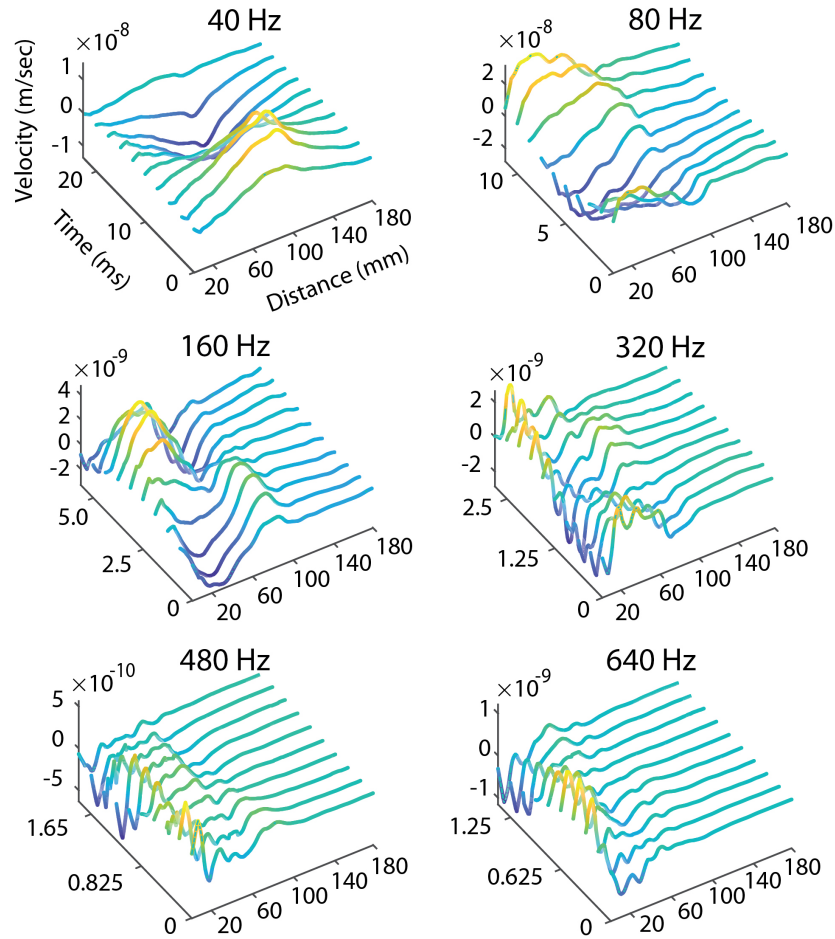
Figure 4.2: Time evolution of mechanical waves. One period of oscillation displayed for each frequency. The skin appeared to exhibit quasi-modal behaviour on stimulation. The attenuation of the waves along the spatial axis was observed to be frequency dependent. Distances extend proximally along the midline of the finger into the palm.

were attenuated by an average of 95%. In contrast, low frequency stimuli were found to excite large sections of the skin through the hand, with the lowest frequency stimuli (40 Hz) eliciting cutaneous waves that initially increased in measured amplitude with distance, reaching a maxima near the base of the finger. We attributed this increase in amplitude to two factors. Firstly, the model of wave propagation predicts the wave to have the form $\exp(-\alpha x)\exp(j(kx - \omega t))$, where $k = 2\pi/\lambda$, with λ being the wavelength. With the presence of reflections and boundary conditions, this can result in standing waves, akin to mechanical modes on a string. Indeed,
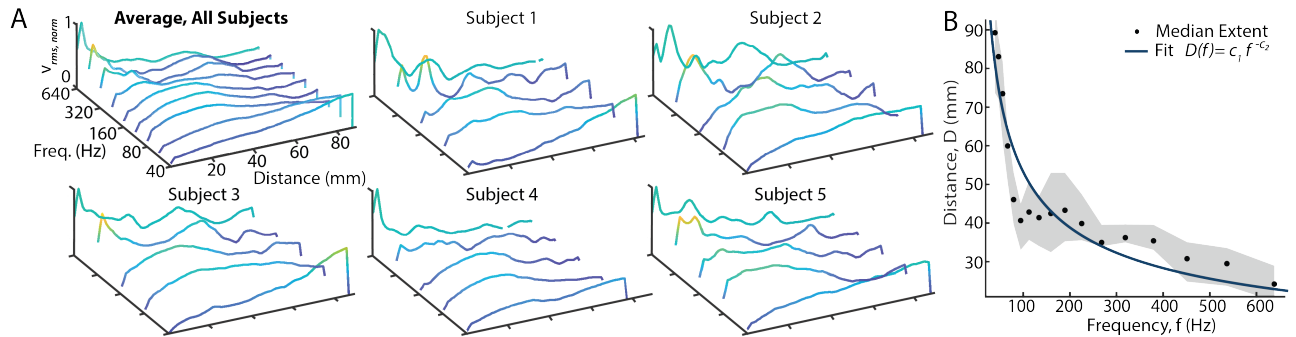
Figure 4.3: The amplitude (normalized rms velocity $v(f)/\max_f v(f)$) of propagating waves decreased with distance in a frequency-dependent manner. A) The magnitude of skin responses varied with distance from the location at which they were applied on the fingertip and the frequency content of the stimulus. Distances extend proximally along the midline of the finger to the location of the knuckle. B) The median spatial extent of vibrations decreased supralinearly with increasing frequency. This reflected the spatial decay and spatial wavelength of the propagating wave. A power law fit $D(f) = 436f^{-.5}$ provided a good fit ($R^2 = .74$) to the measurements. The shaded region represents the quartiles of distribution of the measurements

the time evolution results (Fig. 4.2) suggest that standing waves are set up on the skin when driven by sinusoidal signals at most frequencies. At low frequencies, λ is large (of the order of ≈ 10 cm), yielding a gradual increase over a wavelength, alongside the gradual decay with distance. Second, while the stimuli was primarily applied normal to the skin surface at the tip of the finger, the geometry of the finger results in the skin curving to conform to the shell of the finger, and several boundary conditions are introduced at the locations of the joints. This could result in a conversion of energy in one axis of propagation into another. Thus, the 1-axis measurements may not fully capture all energy present in the fingertip at low frequencies. In the following section, we present preliminary data from 3-axis vibrometry measurements to better study this behaviour of skin.

As frequency increased from 40 Hz to the 640 Hz, the median spatial extent $D(f)$ of cutaneous waves continually decreased from more than 85 mm to less than 30 mm (Fig.4.3B). This was adequately captured by a power law fit $D(f) = 436f^{-.5}$ ($R^2 = 0.74$). This is consistent with the theoretical predictions made in Sec. 4.2, as $D(f)$ specifies the distance as a

function of frequency at which damping term specified in Eq. 4.2 is constant, and thus -

$$e^{-\alpha(f)D(f)} = c$$

From this, we derive that $\alpha(f) = c'f^{.5}$, where c and c' are constant terms. This suggests that the damping term increases supra-linearly with frequency, which signifies a monotonic relation between damping and the frequency of excitation.

Results were similar for all participants. We attributed inter-subject differences to variations in hand geometry and contact conditions. Across participants, the standard deviation of the normalized amplitude $v(f)/\max_f v(f)$ was 0.03, underlining the uniformity of this observed phenomenon.

4.3.7   3-axis vibrometry measurement

Oscillations normal to the skin surface increased in RMS amplitude with distance from the vibration source. We hypothesized this to be due to coupling between strain direction components produced by boundary interactions (Eq. 4.1). To further clarify this, we performed additional measurements of vectorial oscillations of the skin using a 3-axis scanning laser doppler vibrometer system (PSV-500-3D, Polytec, Inc., Irvine, CA). This yielded a full 3-axis orthogonal set of measurements across the skin (Fig. 4.4A). We captured these measurements from one male hand using a frequency sweep method, as in the single axis measurements. We analyzed this data to obtain the RMS velocity vectors at 200 points along the midline of the finger (Fig. 4.4B). To shed light on our observations about the magnitude of oscillations, we computed a normalized inner product $R(f)$ between the normal component of the velocity signal at each measurement point x, $v_z(x, f)$ and the magnitude $|\mathbf{v}(x, f)|$ of the vector vibration
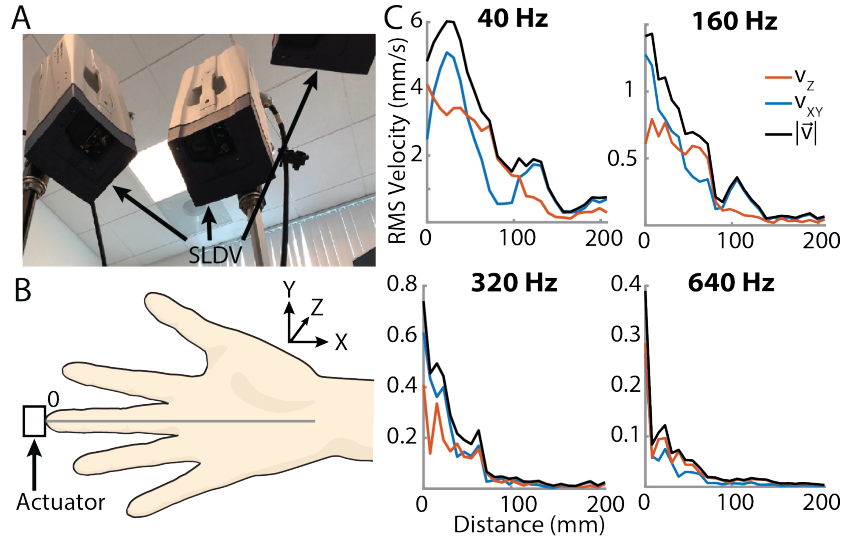
Figure 4.4: Three-axis vibrometry measurements. A) 3D SLDV apparatus, consisting of three 1-axis scanning vibrometers simultaneously capturing vibrations. B) Vibrotactile stimuli was applied at the fingertip of digit 3. Velocity vectors computed at points on a line extending from the fingertip to the wrist. The Z-axis corresponds to the direction normal to the surface of the skin. The XY-axis corresponds to the direction parallel to the surface of the skin. C) Measured in-plane, normal and absolute RMS velocities along the length of the finger for sinusoidal stimuli at various frequencies. Normal measurements capture a large ($> 73\%$) portion of the magnitude of the velocity vector.

velocity signal for each frequency,

$$R(f) = \frac{\sum_x \mathbf{v}_z(x, f)|\mathbf{v}(x, f)|}{\sum_x |\mathbf{v}(x, f)|^2} \tag{4.4}$$

The results show that energy is present in both the normal (Z-axis) and in-plane (XY-axis) vibration directions, and that the component magnitudes varied with position (Fig. 4.4C). At low frequencies, the relative contribution of the normal and in-plane components varied greatly with position, suggesting that coupling between the strain directions was pronounced at such frequencies. At frequencies higher than 480 Hz, the normal velocity component was typically larger than the in-plane component.

Consistent with our single-axis measurements, the median spatial extent, $D(f)$, decreased monotonically with frequency. Averaging across frequencies, the normal oscillation compo-

nent (matching the direction captured in our 1-axis SLDV experiment) captured more than 73% of the magnitude of the vibration vector. Together these findings support the conclusions we drew based on the 1-axis measurements, but a more extensive theoretical and empirical investigation would be needed in order to fully characterize the role of strain component coupling in vibrotactile transmission in the skin.

4.4   Design of Spatiotemporal Haptic Effects

Consistent with theoretical predictions, the in-vivo mechanical measurements reflected that low frequency ($f < 160$ Hz) stimuli excited waves extending throughout the finger and into the hand, while damping confined waves excited by high frequencies ($f > 160$ Hz) close to their locus of application (Fig. 4.1).

A portion of the vibration measurement procedure had entailed the successive application of N brief sinusoidal stimuli with frequencies f_k that increased monotonically, $f_{k+1} > f_k, k = 1, 2, \ldots, N - 1$. This yielded skin vibrations that successively decreased in spatial extent. Several participants independently reported that these increasing-frequency sequences elicited the sensation that the spatial extent of vibrations was contracting over time. In contrast, when we provided sinusoidal stimuli of any constant frequency, the spatial extent of skin vibrations was difficult to discern without special attention.

Informed by these findings, we sought to design vibrational stimuli which could consistently elicit spatiotemporal haptic perceptual effects. Our goal was a pattern of vibrations on the skin which spatially expand or contract in area, which we hypothesized to cause an analogous perceptual response of sensations of expansion or contraction on the skin.

We first observed that a simple frequency sweep stimulus, while causing a spatially varying region of the skin getting vibrated over time, did not elicit such a perceptual response. As vibratory stimuli has been shown to excite extended areas of the skin through a large frequency

range, we hypothesize that effects of tactile masking [213, 214, 215] over the continuum of mechanoreceptors would interfere with the perception of these effects when a frequency sweep is used as a stimulus.

Taking the effects of masking into consideration, we designed vibrational stimuli comprised of sequences of N short segments $x_k(t)$, $k = 1, 2, \ldots, N$ of successively increasing or decreasing frequency content, separated by a pause time between segments. We designed the changes in frequency to span a range from 12.5 Hz to 333 Hz, which matched the range over which the spatial extent of skin vibrations changed most rapidly (Fig. 4.3B). We first tried sequences of sinusoidal segments of equal (constant) duration. However, we observed these to elicit ancillary sensations of ascending or descending "tones" that were distracting, possibly due to the linked temporal frequency channels of audition and touch [216]. Windowed band-passed noise signals were similarly reported to provide sensations of tones, albeit to a lesser degree. To avoid this, we instead designed signals $x(t)$ to consist of sequences of wavelet-like segments $x_k(t)$, whose energies were more broadly distributed in frequency (Figure 4.5). The segments consisted of scaled window functions modulated by a fixed frequency sinusoid.

$$x(t) \quad = \quad \sum_{k=1}^{N} x_k(t - r_k), \tag{4.5}$$

$$= \quad \sum_{k=1}^{N} A_k \, g_k(t - r_k) \, \sin(2\pi f_0(t - r_k)). \tag{4.6}$$

Here, $T = 100$ ms is a short pause time between segments. We chose this value for the pause time as it was larger than empirically observed decay and masking time estimates. A_k is an empirically set gain factor that compensated for differences in the perceived magnitude of the segment signals as determined by pilot testing. The onset time of segment k is $r_k = \sum_{j=0}^{k-1}(\tau_j + T)$.

The window function $g_k(t)$ is a truncated Gaussian of duration τ_k and standard deviation

$\sigma = c\tau_k$.

$$g_k(t) \;=\; \operatorname{rect}(t/\tau_k)\exp\left(\frac{-t^2}{2\sigma^2}\right), \;\; \sigma = c\tau_k \tag{4.7}$$

$$G_k(f) \;=\; \sqrt{2\pi}\sigma \operatorname{sinc}(f\tau_k) \star e^{-2(\pi f\sigma)^2} \tag{4.8}$$

where $\star$ denotes convolution in the frequency domain and $G_k(f) = \mathcal{F}(g_k(t))$ is the window spectrum. We set the scale factor c to $1/5$ to ensure that the bandwidth of the window function is approximately $BW_k = 1/\tau_k$. The spectrum, $X_k(f) = \mathcal{F}(x_k(t))$, of each signal segment is given by

$$X_k(f) = A_k G_k(f) \star \frac{j}{2}\left[\delta(f + f_0) - \delta(f - f_0)\right] \tag{4.9}$$

It is centered at frequency f_0 Hz with a segment bandwidth of approximately $f_k = 1/\tau_k$. This choice of window function makes it possible to control the bandwidth of each segment by modifying the window duration. The sinusoidal carrier (frequency $f_0 = 25$ Hz) ensures that most of the signal energy is contained at frequencies that are salient to vibrotactile perception.

For the concentrating stimulus, we designed signals $x(t)$ with N segments having frequency bandwidths f_k that increased in a logarithmic series over time, from $f_1 = 12.5$ Hz to $f_N = 333$ Hz by controlling the segment duration τ_k. For the expanding stimulus, the sequence was reversed. Stimuli used in the experiments had $N = 10$ segments. This stimulus resulted in consistent perceptual effect, as confirmed through pilot studies.

These stimuli contain frequencies extending from DC to 600 Hz, as verified by analyzing the spectrograms of the signals (Fig.4.5). Few vibrotactile actuators can reproduce such low frequency signals without introducing distortion. Here we used the electrodynamic actuator used for our vibrometry measurements (Mini Shaker Type 4810, Brüel & Kjær, Denmark), which was empirically verified to have a flat response for a large majority of the frequency range of interest.
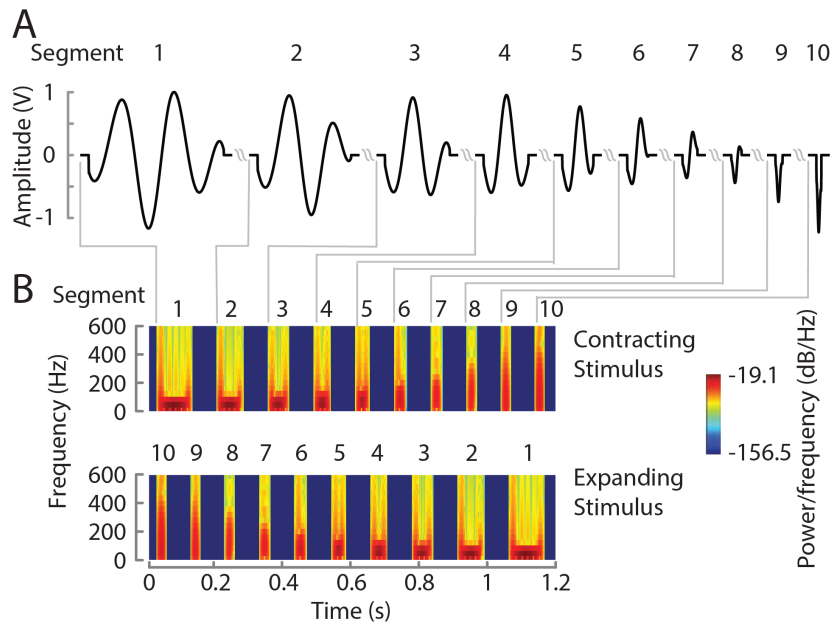
Figure 4.5: The tactile effects were designed to elicit sensations of spatial expansion or contraction via sequences of segments with respectively increasing or decreasing frequency content. For contracting effects, the segments were wavelet-like signals (A) of decreasing duration, and (B) logarithmically increasing bandwidth. Segments were separated with 100ms of pause time.

4.5 Perception of Spatiotemporal Haptic Effects

We hypothesized that our findings linking the frequency of stimuli signals to their spatial extent of vibrations would be reflected in perception as a spatiotemporal haptic effect. To this end, we designed a perceptual experiment in which participants classified either the wave-based effects (described in the preceding section) or control signals as "expanding" or "contracting".

4.5.1 Participants

Fifteen participants volunteered for the experiment (12 male; 19 to 30 years of age). All participants were naïve to the purpose of the experiment and gave their written informed consent. The experiment was conducted according to the protocol approved by the UCSB Human Subjects Committee.
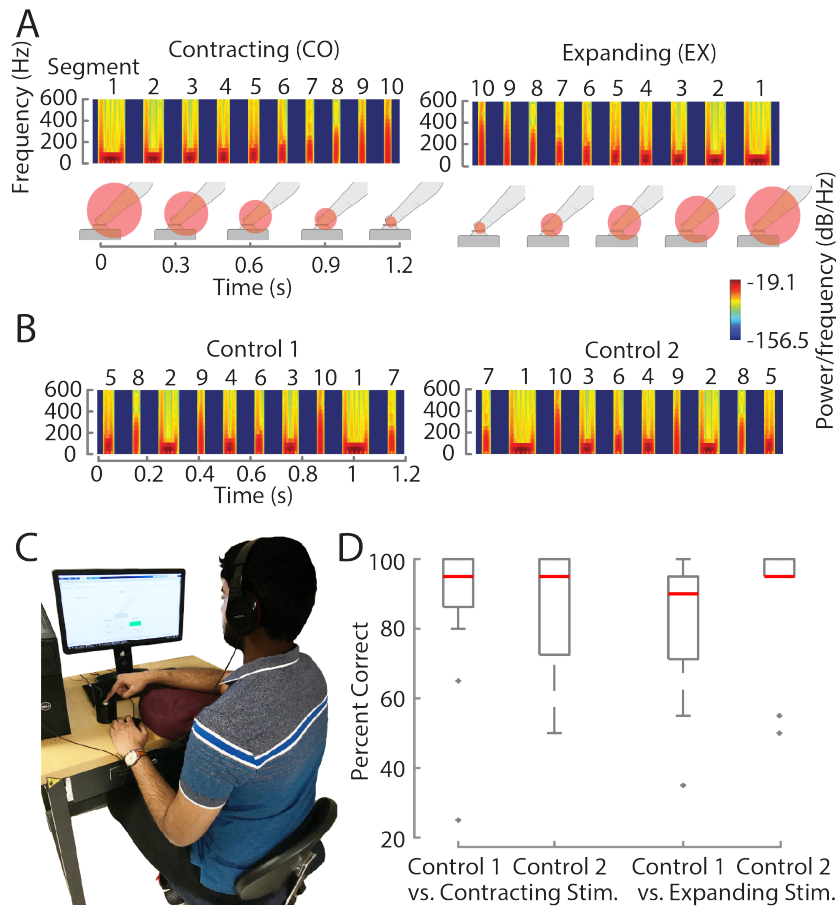
Figure 4.6:   Perceptual experiment. A) Spectrograms of the designed stimuli that produce contracting (CO) and expanding (EX) sensations and associated animations used. B) Spectrograms of the control stimuli, with permuted segments. C) Experiment setup. Participants contacted the actuator with their right index finger. D) Results of the experiment The two plots at the left show results for the two-alternative forced choice experiment involving when the contracting stimulus vs. one of either of the two control stimuli. The two at the right show those for the expanding stimulus. Participants consistently identified the designed stimuli.

4.5.2   Apparatus

Vibrotactile stimuli were applied to the distal end of the index finger using hardware identical to that used in the measurements. Participants were seated, with their index finger in contact with a flat surface (diameter 15 mm) on the actuator (Fig. 4.6C). The finger was held at a 45° angle and a contact force of 2 Newtons (a force gauge was used for comparison). Participants wore foam earplugs (attenuation rating 33 dB) and circumaural headphones playing pink noise

sufficiently loud to mask feedback from the actuator. The experiment was automated via a computer's graphical user interface.

4.5.3   Stimuli

The stimuli consisted of the designed "expanding" (EX) or "contracting" (CO) stimuli described in the preceding section (Fig. 4.6A). We also designed two different control stimuli (Fig. 4.6B). The control stimuli were composed of sequences of the same signal segments $x_k(t)$ present in the EX and CO stimuli, as discussed in Sec. 4.4, with the segments presented in a permuted order. Because we hypothesized that the respectively decreasing or increasing trends of frequency bandwidths over time of the EX or CO stimuli would cause them to be perceived as expanding or contracting, we selected permutations of signal segments so that there was no systematic increase or decrease in frequency extent over the course of each entire control signal, or over the first or second half separately (Fig. 4.6B).

4.5.4   Procedure

The experiment was based on a two-alternative forced choice task in which participants were presented with one designed stimulus (EX or CO) and one control stimulus. Participants were also presented with an animated visual representation of "expansion" or "contraction" at the fingertip matching the presented designed stimulus (Fig. 4.6A). We did not describe what these animations represented, nor did we describe any association with the haptic stimuli, which participants were naïve to. In pre-testing, we determined that visual representations were understood better than text labels. Participants were allowed to experience the two stimuli an arbitrary number of times and asked to report the stimuli which caused a perceptual sensation closest to what is indicated in the displayed visual animation. The stimuli were presented in random order and their position was randomized on the computer screen. We selected one de-

signed and one control stimulus at random for each trial, yielding four possible combinations. Each of the designed or control stimulus was presented a total of 40 times, for a total of 80 trials per participant. In a post-experiment questionnaire participants were asked to describe the strategy they used to respond. After the experiment, they felt the designed stimuli again and were asked to describe them.

4.5.5 Analysis

We computed the percentage correct scores as the proportion of responses that assigned the designed stimulus to the corresponding visual depiction across all presentations for each of the four combinations, for each participant. The median percentage correct score was computed across participants. We assigned a percentage correctness of 75% as the threshold for a positive effect relative to chance performance (50%). Because the distributions violated normality assumptions, we used non-parametric one sample Wilcoxon signed rank tests. We tested the null hypothesis that the median was less than or equal to 75%. We also assessed the effect of the control stimulus choice using Mann Whitney U tests.

4.5.6 Results

Without training or prior exposure, participants consistently associated the designed EX and CO stimuli with the visual representations of "expanding" or "contracting". The designed stimuli were selected with median probability 96.7% (CO stimuli: 97.5%, EX: 95%). The control stimuli were selected with median probability 3.3%. The percentage correct scores were significantly greater than a positive effect threshold of 75% ($p = 0.0163$ and $p = 0.0039$ for CO and EX). There was no significant effect of the choice of which control stimulus was presented ($p > 0.74$ and $p > 0.08$ respectively).

4.5.7   Discussion

The results indicate that the designed stimuli were consistently associated with the designed visual depictions of expansion and contraction. This suggests that participants perceived the stimuli as respectively expanding or contracting, consistent with predictions from theory and mechanical observations, without any prior exposure or training. The high median accuracy reflects the robustness of these associations. The associations were unaffected by the control stimulus used for the comparison.

After repeated exposure to the stimuli, participants would have had little difficulty identifying either the designed or control stimuli, due to the differences in timing and frequency content. Consequently, it could be hypothesized that they based their decisions on arbitrary cognitive criteria. However, a priori, we would expect any such criteria to result in a bi-modal response pattern, with an equal number of participants selecting both the designed and control stimuli consistently. In our experiment, the control stimuli were selected with a very low median response rate (3.3%). Furthermore, no participant consistently inverted the associations of the stimuli to the visual depictions of expansion and contraction. Together, these results indicate that the effect was not bistable, and suggest that arbitrary criteria were not applied.

We conclude that the increasing or decreasing bandwidth of the designed stimuli caused them to be perceived as spatially expanding or contracting. This conclusion is supported by the questionnaires, in which participants spontaneously described sensations such as "concentrating to / spreading from the fingertip" or a "wave coming closer to / moving away from the fingertip" or "radiating inwards / outwards" and proceeding "from bigger portion of the finger to smaller portion / vice versa". Informal testing also suggests that the effects are similarly perceived with altered mechanical configurations of the finger, and at various contact locations.

The designed stimuli were selected with greater frequency after the first few trials, with percentage correct score increasing from 87.5% (median percentage for trials 1-4) to 100%

(trials 5-20). Because participants did not feel any stimuli prior to trial 1, this could reflect increasing familiarity with the protocol. It could also reflect strengthened associations after repeated exposure, which was consistent with our informal observations.

4.5.8   Multi-actuator spatiotemporal effects

We investigated enhancements to the design space of haptic effects afforded through the use of multiple actuators. In one example, we positioned fingertips separately on two actuators (Fig. 4.7), and coupled the designed EX and CO stimuli by delivering them individually to each actuator channel with a time offset between them. The offset was set at 1 s, to ensure a small amount of spatiotemporal overlap in the regions of the skin that are stimulated through each actuator. This resulted in sensations that were reported to travel from one fingertip into the palm, and then back into the other fingertip in a single motion (as verified by experts from the haptics community). Such haptic motion effects between pairs of actuators could previously only be rendered over much smaller distances with conventional methods, as compared to the > 15 cm distance which we achieve here. This showcases the potential for design of efficient and evocative effects using spectral control based methods. We aim to further evaluate multi-actuator effects in future work.

4.6   Evaluation of Visuo-Haptic Spatiotemporal Effects in Virtual Reality

To explore potential applications and highlight the utility of the designed spatiotemporal effects, we incorporated them alongside visual cues (which also vary in space and time) in multi-modal interactions, with the aim of improving their perceived engagement and immersion over the use of conventional vibrotactile stimuli. The haptic effect can, in this instance,
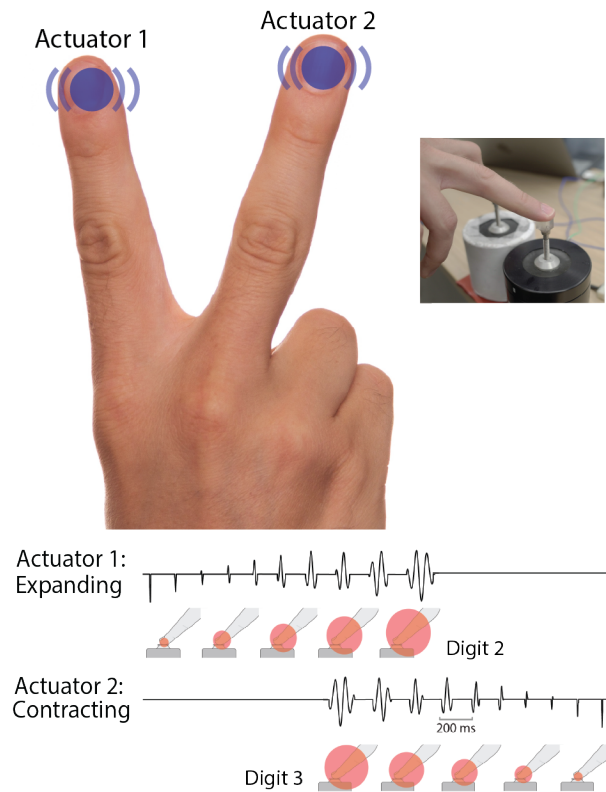
Figure 4.7:   A proposed multi-actuator extension to the effects discussed here involves actuators presenting the EX and CO stimuli to distinct fingers with a time offset of 1 s. Empirically, this resulted in sensations expanding from one fingertip into the palm, and then contracting to the other fingertip, in one single, evocative, motion.

be delivered with a single actuator present in either a hand-held or grounded embodiment. To study this, we designed a simple evaluation experiment in a virtual reality setting where participants rated the spatiotemporal stimuli in conjunction with designed visual cues of expansion and contraction, on various user experience metrics.

4.6.1   Visual cue design

We designed visual cues of expansion and contraction to accompany the press of a button in virtual or augmented reality. We chose to vary the size of a visually seen virtual object over time, which we hypothesized would supplement the evolving perceived spatial extent of the
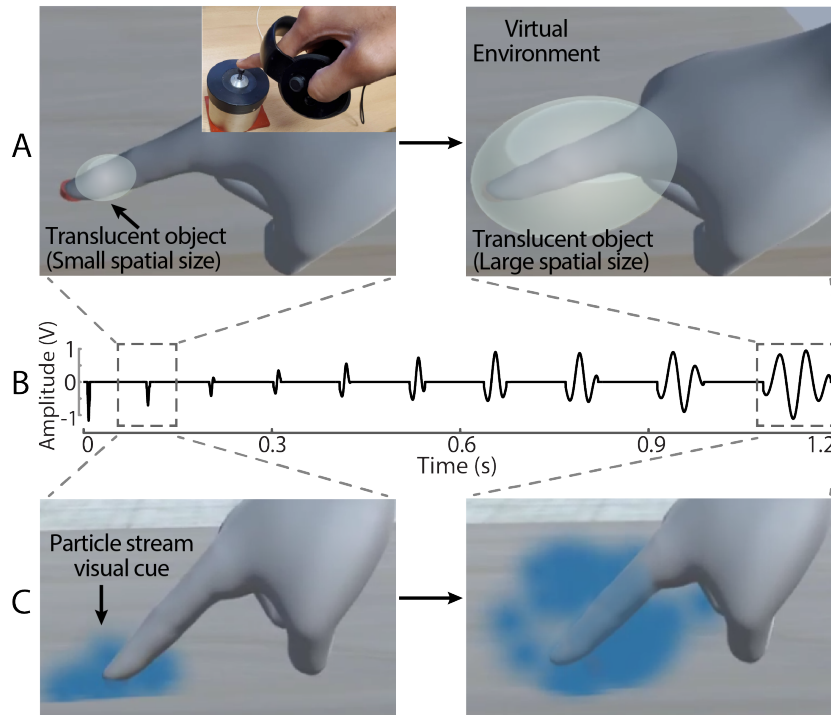
Figure 4.8: Visual cues presented with the spatiotemporal haptic stimulus in virtual reality. A) Visual cues in the virtual environment as used in the evaluation experiment. In the experiment, participants hold a VR controller and contact the actuator with the index finger of their right hand (inset figure). The controller enables a registered hand representation in VR, where the hand is shown to contact a surface. For the expansion cue (V-EX), a translucent ovoidal object is positioned at the fingertip that expands in volume over the stimulus duration to cover the entirety of the finger. The contracting visual cue reverses this over time. B) The expanding haptic stimulus applied in conjunction with the visual cue C) An example of an alternate visual cue which we observed to be enhanced by the spatiotemporal haptic effects. A series of particles are emitted from the contacted surface which expand to cover the finger.

designed haptic effects to result in a greater sense of engagement.

One visual effect consisted of a direct representation of increasingly larger or smaller areas of the skin getting excited. A translucent ovoidal object (similar to a bubble) was overlaid onto the length of a virtual representation of the index finger of the hand, which increased or decreased in size over time (Fig. 4.8A), with the object occupying the entire length of the finger at its largest size, while being centered at the tip of the finger at its smallest size. The duration of the visual cue was set to be exactly the same duration as the designed haptic cue. We used this visual cue for the evaluation experiment discussed subsequently.

In a similar fashion, we also explored alternate visual cues, one example of which was a stream of particles being shown to be emitted on pressing a the button, which we chose to be paired with the "expanding" haptic stimuli (Fig. 4.8C). Another alternate cue consisted of the hand representation shrinking or expanding in size over time.

4.6.2 Participants

Nine participants volunteered for the experiment (5 male; 21 to 33 years of age). All participants were naïve to the purpose of the experiment and gave their written informed consent. Participants reported (corrected-to-) normal eyesight and no neurological conditions that could affect their sense of touch. The experiment was conducted according to the protocol approved by the UCSB Human Subjects Committee.

4.6.3 Apparatus

The experimental apparatus consisted of a virtual reality (VR) headset with associated controllers (Rift with Touch Controllers, Oculus VR Inc, Menlo Park, CA) and a vibrational actuator identical to that used in the measurements and prior experiment. Participants were seated in front of a table, with their hands grasping the controllers, and the index finger of their right hand in contact with a flat surface (surface area 36 mm^2) on the actuator (Fig. 4.8A). Participants were asked to use a fully extended index finger to contact the actuator and to use gentle pressure to maintain contact. No further restrictions on contact angle or contact force were imposed. The VR headset displayed a calibrated version of the table, and the VR controllers were used to render co-located representations of the hands in the virtual space. A virtual button was displayed at the registered position of the actuator.

4.6.4 Stimuli

The stimuli consisted of a combination of visual and haptic cues. The visual cues used in the experiment consisted of representations of "expansion" (V-EX) or "contraction" (V-CO), which were achieved with a translucent object as previously discussed, which increased or decreased in size over a duration of time respectively (Fig. 4.8B). The haptic cues comprised the spatiotemporal expanding and contracting stimuli (S-T.H.), described in the preceding sections (Sec. 4.4, Fig. 4.6A), which were paired with the corresponding visual cue. The control haptic stimulus (C.H.) was constructed as a continuous 200 Hz vibration. This stimulus was chosen as a control because sinusoidal vibrations of frequencies between 200 and 250 Hz are often used in commercial devices to deliver haptic feedback [86]. The durations of the visual and haptic cues were set to be identical.

4.6.5 Procedure

During each trial of the experiment, participants pressed a button on the controller to allow them to experience the stimulus. They were then asked one of three questions, which were as follows

- Rate the interaction on how engaging it felt

- Rate how congruent the vibrations you felt were with the visual cue

- Rate to what extent you felt the vibrations enhanced the visual cue

Participants provided a rating for these performance metrics on a 15 point discrete scale, with extrema being labelled "Not at all" and "Very". Participants were allowed to experience the stimulus any number of times before providing their rating.

As a control condition, we introduced trials in which the visual cue was presented without any accompanying haptic stimulus (N.H.), to obtain baseline ratings for how engaging the

visual cue was perceived. Thus, there were a total of 14 distinct trials (2 visual $\times$ 2 haptic $\times$ 3 questions + 2 visual $\times$ 1 question). The stimuli were presented in a block-randomized fashion. There were a total of seven repetitions for each block of trials in the experiment, leading to a total of 98 trials per participant. In a post-experiment questionnaire participants described how many different vibrational stimuli they perceived, the strategies they used when rating the stimuli, and provided free-form comments on the stimuli they perceived.

4.6.6   Analysis

The first block of trials for each participant was considered as a practice block and their reports were discarded from the analysis. This allowed for more consistency in the results as the participants would have experienced all trials in the first block and formulated a rating strategy for the reminder of the experiment. One participant did not follow the reporting instructions and was excluded from the analysis. We computed the average of the ratings for the expanding and contracting visual cue, and computed the mean and standard deviations across trials for each performance metric for each stimulus for each participant. The normality of the data was evaluated with the Pearson's chi-squared goodness of fit test. Pairwise comparisons for the means of the performance metrics were performed with two sample t-tests.

4.6.7   Results

Participants consistently rated the interactions with both the spatiotemporal haptics and the control haptics stimuli to be significantly more engaging than without haptics (Fig. 4.9), when presented with the visual cue ($p < 10^{-7}$ and $p = .001$ respectively) . Interactions with the spatiotemporal haptic stimulus were rated as more engaging than those with control haptics than ($t(14) = 2.7, p = 0.018$) at the 5% significance level. The spatiotemporal stimuli was found to be significantly more congruent with the visual cue ($t(14) = 2.4, p = .034$), and
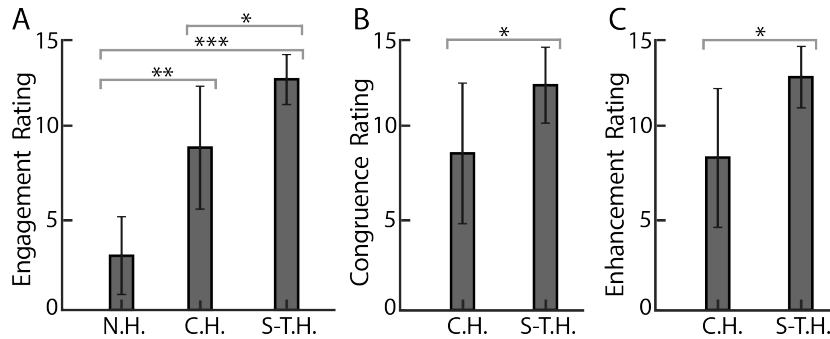
Figure 4.9:   Results of the evaluation experiment. A) Ratings for perceived engagement of interaction, for the No Haptics (N.H.), Control Haptics (C.H.) and Spatio-temporal Haptics (S-T.H.) conditions. B) Ratings for congruence of haptics with visual cue, and (C) enhancement of visual cue through haptics, for the C.H. and S-T.H. conditions. Results averaged across both visual cues and all participants . Error bars indicate standard deviations. Participants consistently rated the spatiotemporal haptic stimuli to result in the most engaging interaction. Further, the spatiotemporal effects were rated to better enhance the provided visual cue and be more congruent with its varying nature, when compared with a single frequency vibrational stimuli (For comparisons, $* \Rightarrow p < .05$, $** \Rightarrow p < .01$, $*** \Rightarrow p < .001$).

the spatiotemporal stimuli was rated to significantly enhance the visual cue over the control stimulus ($t(14) = 2.8, p = .014$). Normality assumptions held for all distributions.

4.6.8   Discussion

In the visual only (N.H.) conditions, participants pressed a button and saw the visual animation without haptic feedback. Adding either form of haptics greatly and significantly increased how engaging participants perceived the interaction to be. In addition, the spatiotemporal haptic stimulus was perceived as significantly more engaging than the control stimulus. Based on these results, the spatiotemporal haptic effects were found to be more perceptually engaging over the use of single frequency haptic stimulation when combined with the designed visual clues. This was also borne out in the written responses of participants in the post-experiment questionnaire, who reported the spatiotemporal haptic effects to be more compelling and their preference for it.

The designed spatiotemporal haptic stimulus was rated to be significantly more congruent

with the visual cue than the single frequency vibrational stimulus was. This suggests that participants identified the perceived spatially expanding or contracting sensations on of the skin to be harmonized with the displayed visual cues which showed increasingly larger or smaller regions on the finger being enveloped by a bubble over time. The spatiotemporal haptic stimulus was also found to significantly enhance the designed visual feedback in this visuo-haptic feedback scenario.

On averaging the computed standard deviations across the three performance metrics, we observe that there was a large variability in the ratings for the control stimuli ($\sigma = 3.8$), which was twice as large as the variability for the spatiotemporal stimuli ($\sigma = 1.8$). This suggests that the spatiotemporal stimuli resulted in a more consistent experience across participants.

4.6.9 Applications

In addition to the aforementioned visuo-haptic effects based on a bubble metaphor, we designed other visuo-haptic effects combining our vibrotactile rendering method with graphics effects such as particle clouds (Fig. 4.8C). Informal testing revealed that these multisensory effects were likewise appreciated as eliciting sensations of expansion or contraction. This suggests that there are many opportunities for using the methods proposed here to enhance experiences in VR and HCI applications. Beyond the rendering methods described here, we have also explored interations with virtual control interface elements, such as buttons or sliders. In the latter case, we found it possible to produce a sense of mechanical resistance during operation of such a virtual slider. Thus, the effects proposed here hold promise for being integrated in a variety of interfaces in augmented and virtual reality. Because our methods afford dynamic control over spatial properties of haptic stimuli using even a single actuator, they may also prove useful for providing directional cues, such as in navigation devices or assistive technologies for individuals with visual impairments.

4.7   Conclusions

In this work, we show how a single actuator may be used to generate vibrotactile stimuli with dynamically controlled spatial extent. Our method exploits the frequency-dependent damping of cutaneous wave propagation. We used theoretical analysis and experiments using optical vibrometry to reveal that the frequency content of applied vibrations determines the spatial extent of vibrations in the skin. We combined these findings with properties of vibrotactile perception to design vibrotactile stimuli that can be delivered via a single actuator in order to produce haptic effects of expansion or contraction in the skin in regions near the locus of actuation. A perceptual experiment revealed that these stimuli were consistently perceived as respectively expanding or contracting, consistent with predictions from theory and our mechanical experiments.

To show how these phenomena may be applied to generate evocative multisensory effects, we designed rendered graphics effects that matched the haptic effects. A user study revealed the resulting visuo-haptic cues of expansion or contraction to be more engaging when compared with conventional vibrotactile stimuli. These methods hold promise for improving applications in virtual reality and human-computer interaction. Our findings demonstrate how the physics of waves in the skin can be exploited to design methods for spatiotemporal haptic feedback that are both practically effective and perceptually evocative.

While the conditions of our experiment addressed stimuli applied at the fingertip, the physical and perceptual phenomena that enabled them are general. We have informally observed these effects to be reproducible at other body locations. Our results show how a single actuator is already sufficient for producing evocative spatiotemporal effects. They also suggest that it is interesting to apply these methods in multi-actuator configurations that provide greater control over the spatiotemporal haptic effects that are produced. Examples of such phenomena include tactile apparent motion effects. The advantage of our methods for producing haptic effects to

be delivered to extended areas of the skin is that they may provide extensive spatial control with small numbers of actuators. We intend to explore these opportunities further in future work.

Chapter 5

A Fluidic Electromagnetic Actuator for High-Fidelity Haptic Feedback

In the design of haptic displays for virtual and augmented reality, the miniaturization of components to make devices wearable and portable is a major requirement. The findings from Chapter 4 demonstrates that an expanded design space of haptic effects can be achieved through controlling the spectrum of the stimuli, highlighting the utility of actuators that can reproduce signals with high dynamic range across a wide range of frequencies. However, the current state-of-the-art of compact haptic actuators are limited in this regard, both due to thermal constraints and mechanical limitations that force their operation to a narrow range of frequencies. Inspired by this need, Chapter 5 presents the design of a new type of small form-factor, high-fidelity (wide bandwidth) actuator operating on electromagnetic principles. The design employs ferrofluid, a functional material, to optimize the device performance. The assembled prototype is compact, thermally efficient, and has an exceptionally flat frequency response. The actuator will allow for the creation of new controller-based or wearable displays that can generate rich haptic sensations.

At the time of writing, this chapter was submitted to the journal Sensors and Actuators A: Physical under the title :

N. Kastor*, B. Dandu*, V. Bassari, G. Reardon and Y. Visell, "A Fluidic Electromagnetic Actuator for High-Fidelity Haptic Feedback," Sensors and Actuators A: Physical.

* These authors contributed equally.

Abstract

Engineering high-fidelity haptic actuators is challenging due to the capabilities of the human sense of touch. Tactile sensing via the skin operates within a wide frequency bandwidth, with high spatial resolution and dynamic range. These sensing capabilities cannot be matched by existing haptic feedback devices. Electromagnetic haptic actuators are widely used for delivering vibrations to the skin, especially in handheld and wearable devices, due to their robustness and the relative ease and efficiency with which they can be designed and driven. However, existing actuators can only reproduce a limited subset of perceptually significant tactile signals. Compact haptic actuators are needed in many applications, but such actuators are rarely capable of furnishing sustained forces or low-frequency vibrations. This limitation is due in part to thermal constraints that grow rapidly as actuator dimensions are decreased. Here, we present a compact fluidic electromagnetic actuator for high-fidelity haptic feedback. This thermally efficient actuator integrates a permanent magnet within a fabric-reinforced elastic membrane coupled to a ferrofluid-encapsulating magnetic circuit. Using theoretical modeling, simulations, and experiments, we show how a compact actuator may be designed to produce both sustained indentations of the skin and vibrations and to generate transient forces of 10 Newtons or more. This design approach could increase the fidelity of haptic actuators in many

wearable or handheld devices.

5.1 Introduction

Haptic actuators are electronic devices for mechanically stimulating the skin in the range of human touch sensitivity. Such actuators are widely used in mobile computing devices, game controllers, wearable electronics, virtual reality interfaces, and other devices [86]. Haptic actuators are also being widely investigated for augmented and virtual reality, robotic surgical interfaces, surgical simulators, prosthetics, and other domains [100, 217].

The skin, the sensory organ of touch, integrates many thousands of tactile receptors, and multiple receptor types, that enable it to capture mechanical signals over a wide frequency range, from 0 to 1000 Hz [22]. Near frequencies of 200 to 300 Hz, vibrations with amplitudes smaller than 10 nanometers can be felt, surface textures on the scale of tens of nanometers can be discriminated, and locations of light touch contact can be discriminated with millimeter precision; See [218] for a recent review discussion. The dynamic range of perceivable forces is also impressive, extending from approximately 10^{-3} to 10^2 Newtons. No existing haptic device is capable of generating mechanical signals across the breadth of this range of frequency, spatial resolution, and dynamic range [218, 219]. The large disparity between haptic perceptual abilities and the capabilities of haptic actuators has motivated substantial research efforts, but no technologies yet demonstrated can even approximately match perceptual capabilities [220, 221, 222, 223].

Among the most common technologies for stimulating the skin are electromagnetic (EM) actuators. In both commercial products and in engineering research, the great majority of electromagnetic haptic actuators are of inertial linear voice-coil type. Examples include narrow-bandwidth linear resonant actuators and wider-bandwidth Lorentz force actuators [86, 224, 221]. Such devices comprise an assembly including a permanent magnet (or magnets) and

voice coil coupled within a casing via springs or elastic members. Such actuators can be designed to directly displace the skin, although inertial configurations are more commonly used. When driven, the coil produces an electromagnetic force causing the magnet to oscillate. The resulting oscillating motions are transferred to the skin (or other surface), via conservation of momentum. Such devices can be designed to be inexpensive, and are often simple to drive at low voltages with commodity electronics, similar in both respects to inexpensive loudspeakers. However, the practical bandwidth of such devices is limited to a single frequency, if driven at the mechanical resonant frequency $f_0 = 2\pi\sqrt{k/m}$, where m is the moving mass and k the spring stiffness, or to frequencies greater than f_0 if wider bandwidth operation is needed [225]. Consequently, such devices are unable to deliver sustained or low frequency forces or displacements to the skin. Such stimuli are commonly felt during sustained or transient contact with familiar objects and surfaces.

Several devices have been designed to overcome these limitations [226, 227, 228, 229]. However, most are limited in dynamic range or in their ability to generate high-frequency vibrations. A haptic actuator capable of reproducing both sustained and oscillating forces or displacements with high dynamic range and temporal precision would have many potential applications. Such actuators could more readily reproduce touch sensations like those felt during naturally occurring touch interactions, including texture vibrations [230], transient forces, or sustained skin indentations. In applications, such actuators could be used to produce evocative haptic effects [231, 232], such as those described in recent publications of the authors [12, 233]. However, it is challenging to design compact actuators with such properties, due to mechanical resonance effects and thermal limitations. Indeed, due to thermal limitations, the maximum force F that can be produced by a permanent magnet electromagnetic actuator scales $F \propto l^2$, where l is a length scale parameter [234]. Thus, thermal effects fundamentally limit the dynamic range of forces that can be produced by such actuators.

In this work, we present a compact actuator capable of producing quasi-static indentations,

and low and high frequency vibrations with high dynamic range across the entire frequency range that is perceivable via touch. This performance is achieved via thermal and electromechanical design specializations, including a ferrofluid encapsulated within a low magnetic reluctance circuit. The design leverages features that are used in high-performance loudspeaker designs [235, 236]. The properties of the ferrofluid aid in thermal management and provide viscosity that facilitates control over the device dynamics. The performance and compact form factor of this actuator make it particularly suitable for use in wearable haptic applications for augmented reality, virtual reality, mobile computing, and human-computer interaction.

5.2   Design Concept and Operating Principle

The aforementioned considerations led us to identify design objectives for a compact electromagnetic haptic actuator. To facilitate use in wearable haptic systems, our goal was to achieve dimensions comparable to the size of a fingertip. We used a moving-magnet voice-coil configuration in which the magnet assembly is placed in contact with the skin surface. Due to fundamental thermal limitations summarized in the foregoing, achieving our goals required that the thermal performance of the device be optimized through the use and arrangement of thermally conductive materials, including ferrofluid and thermal epoxy resins. Motivated by the frequency bandwidth associated with human tactile sensitivity, we aimed to engineer the device to be capable of reproducing frequencies from DC (0 Hz) up to nearly 1 kHz, a range that includes both quasi-static forces or displacements, and higher frequency vibrations. To ensure a useable frequency bandwidth spanning this range, we designed the device to minimize mechanical resonances across this frequency range. This was facilitated, in part, by the damping characteristics of the encapsulated ferrofluid. The range of forces that could be produced was augmented by the use of a paramagnetic core within the electromagnet. We offset

the attractive force between the moving magnet and core via a magnetic bearing implemented

via a second permanent magnet in the magnetic circuit. These features, and optimizations of

the geometry and assembled configuration, together maximized the feasible dynamic range of

forces and displacements that could be delivered to the skin via the actuator.
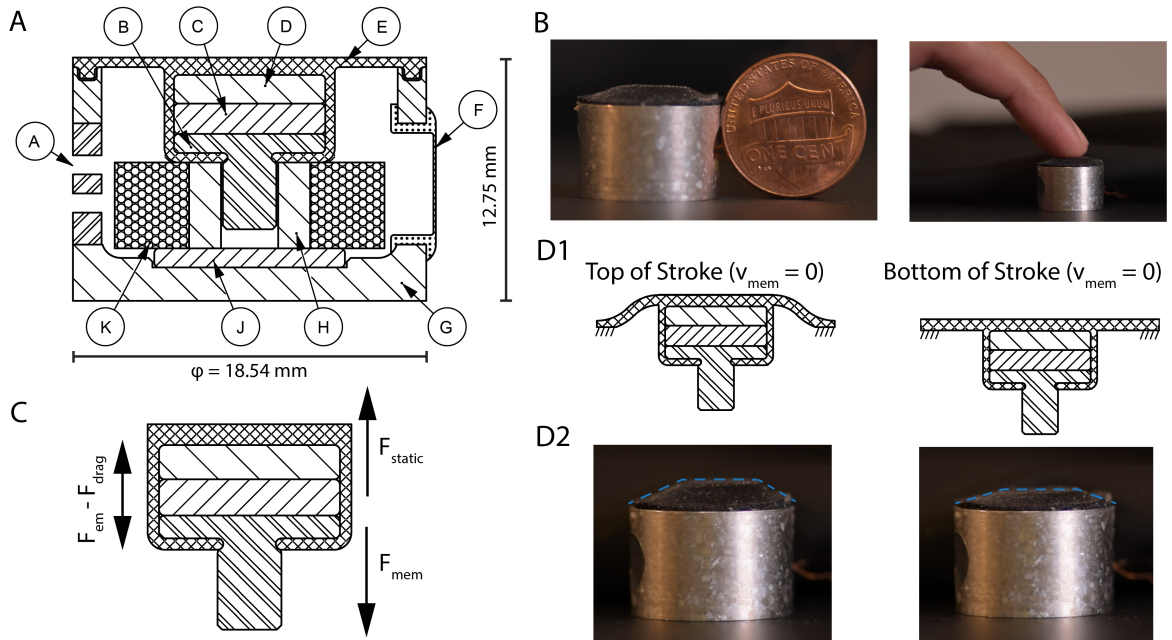
Figure 5.1:   The compact fluidic EM haptic actuator design resulted from our theoretical modeling, numerical simulations, analyses, and fabrication process. A) Schematic drawing of the actuator. Cross-section with the following components. A: Filling and wiring ports. B: Bearing. C: Permanent magnet. D: High magnetic permeability plate. E: Fiber-reinforced membrane diaphragm. F: Fluid displacement feature. G: High magnetic permeability housing. H: High magnetic permeability electromagnet core. J: Fixed permanent magnet. K: Copper electromagnet coil. Dimensions of the actuator are listed. B) Images of constructed actuator. One cent coin to scale. C) Free body diagram of the moving mass of the actuator. F_{static} denotes the net repulsive forces due to the magnetic components. F_{mem} denotes the restoring force of the membrane. F_{em} and F_{drag} are the forces due to the current through the coil and the viscous drag respectively. D1) Diagrams showing the moving mass at the top and bottom of its stroke. D2) Images highlighting the top and bottom of the stroke of the constructed actuator, when it is driven by a 1 A rms 0.5 Hz sinusoidal signal.

The actuator is constructed using two axially aligned permanent neodymium magnets (parts

C and J; refer to Fig. 5.2A for the design and part labels), which have their like poles facing

each other, resulting in a static repulsive force F_{static} between them. One of the magnets is embedded within the ferromagnetic actuator housing (G), while the other is suspended at the far end of the actuator within a fiber reinforced membrane diaphragm (E). A copper coil (K) wound around a ferromagnetic core (H) is placed in the region between the two magnets, such that it contacts the embedded, fixed magnet (J) and has some clearance with the suspended, floating magnet (C). The application of current I to the coil results in additional magnetic flux through the system, which interacts with the suspended magnet to apply added electromagnetic forces $F_{em}(I)$ to it. The membrane in the annular region between the magnet and the actuator housing acts as a spring that provides a restoring force $F_{mem}(\delta)$ with imposed displacements δ, and can thus return the moving mass assembly to a zero position when the currents are turned off. To improve the efficiency of the magnetic circuit, a small top plate (D) is introduced into the moving mass assembly. A linear bearing comprising a miniature shaft within the core, and bearing (B) is introduced to limit displacements in the radial direction and out-of-plane rotations. This feature could introduce additional drag forces F_{drag}, which are minimized in our design through the use of a hollow bearing shaft. The actuator is filled with ferrofluid to further improve the magnetic performance, as well as to introduce damping to the system, thereby limiting the impact of resonance. A picture of the constructed prototype with no input current shown in Fig. 5.2B.

The moving mass of the actuator is designed to directly contact the skin. With the moving magnet assembly coupled to skin, a quasi-static analysis yields the resultant normal force that the actuator provides to the skin (Fig. 5.2C), which is given by

$$F_{act}(I) = F_{em}(I) + F_{static} - F_{mem} - F_{drag} \tag{5.1}$$

The magnetic bearing results from repulsive forces between the magnets. We selected the magnet geometries to ensure that the nominal position of the moving magnet was at the center

of the range of its motion even when lightly loaded. In the absence of external loading of the moving magnet, the moving magnet displaces until the restoring force of the membrane is balanced by the those due to the electromagnet, membrane, and magnetic bearing. The clearance specified in the design between the moving mass assembly and the core serves as a hard limit to the displacement at the bottom of the stroke of motion, when large negative currents are driven through the coil (values reflecting the performance of our device are reported below). The displacement at the top of the stroke is constrained, at the largest excursions, by the membrane hyperelasticity (Fig. 5.2D). We empirically identified the approximately linear range of motion as a function of current within the displacement extremes.

5.3   Electro-magnetic modeling

The forces generated from this electromagnetic actuator design are determined primarily by the resultant forces on the moving magnet assembly, which we model both analytically and with numerical simulations.

5.3.1   Analytical modeling

The resultant force on the moving magnet can be decomposed into the static repulsive force between the two permanent magnets and the electromagnetic force between the coil and the suspended magnet element. Each of these were modelled separately.

The forces on a permanent magnet with magnetization $\mathbf{M}$ in an external magnetic field $\mathbf{B}$ can be derived by considering a differential volume inside it with a magnetic moment $\mathbf{m} = \mathbf{M}dV$. The total force $\mathbf{F}$ is computed using the electric current loop model in the absence of electrical currents within the magnetic volume, and integrating the differential forces [237, 238]

-

$$\mathbf{F} = \int_V \nabla(\mathbf{m} \cdot \mathbf{B}) dV \tag{5.2}$$

The exact solutions for the forces depends on the geometry of the system. Accurate expressions can often only be computed for simplified geometries in free space. For the purposes of identifying analytical expressions for the forces experienced by the suspended magnet, we first neglected the effect of the ferromagnetic components (parts D, G, H in Fig. 5.2).

The axial force $F_{z,mm}$ between the two coaxial cylindrical magnets (i.e. the fixed and suspended magnet) was approximated by computing elliptic integrals arising from this geometry, using a low-order approximation for the Bessel function terms that arise. The approximation that is entailed is valid under the assumption that the magnets are far from each other relative to their geometry [239]. Computation yields

$$F_{z,mm} \approx \frac{1}{4} \pi \mu_0 M^2 r_m^4 \sum_{i,j=0}^{1} \frac{(-1)^{i+j}}{(d_{\mathrm{mm}} + it_1 + jt_2)^2} \tag{5.3}$$

Here, $M = B_0/\mu_0$ is the saturation magnetization of the permanent magnets, B_0 is the residual flux density d_{mm} is the distance between the poles, r_m is the common radius of the magnets, and t_1, t_2 are the heights of the individual magnets. In the remainder, we omit the subscript z and consider all forces to be in the axial direction unless otherwise noted.

To compute the axial force between the electromagnetic coil and the suspended magnet F_{em}, we used an equivalent current-carrying coil representation of the permanent magnet. We obtain an expression for the force between the two by computing their mutual inductance, under the assumption that the magnet is smaller than the coil and the field lines from the coil

are nearly parallel to the magnetic moment of the magnet [240]. This yielded

$$F_{em} \approx \frac{\mu_0 n_s I_s M \pi r_m^2}{2} \times \left[\frac{d_{\mathrm{mc}} + t_s + t_m}{\sqrt{(d_{\mathrm{mc}} + t_s + t_m)^2 + r_s^2}} - \right.$$
$$\left. \frac{d_{\mathrm{mc}} + t_s}{\sqrt{(d_{\mathrm{mc}} + t_s)^2 + r_s^2}} - \frac{d_{\mathrm{mc}} + t_m}{\sqrt{(d_{\mathrm{mc}} + t_m)^2 + r_s^2}} + \frac{d_{\mathrm{mc}}}{\sqrt{d_{\mathrm{mc}}^2 + r_s^2}} \right] \tag{5.4}$$

where n_s is the number of turns per unit length of the coil, I_s is the current, r_s, t_s are the radius and length of the coil respectively, t_m is the height of the magnet, and d_{mc} is the axial distance between the closest ends of the coil and magnet. If axial symmetry is maintained, the net torque on the suspended magnet due to the magnetic field of either the fixed magnet or the electromagnetic coil is zero.

We obtained specific solutions using geometrical parameters from the fabricated actuator, described in further detail in sections that follow. The analytical model provides a static force F_{mm} of 0.59 N when the pole to pole distance d_{mm} is 7 mm. The model yields an electromagnetic force F_{em} of 0.21 N when the current is 1 A, for $d_{\mathrm{mc}} = d_{\mathrm{mm}} - t_s = 2.5$ mm. This force scales linearly with current.

The addition of the ferrofluid, and the ferromagnetic core, shield and top plate increase the efficiency of the electromagnetic circuit (and thus force magnitude) by reducing the magnetic reluctance, which increases the flux density **B**. However, these elements also alter the magnetic flux paths, causing them to curve more than when these elements are not included, thus slightly reducing forces, due to the dot product between **m** and **B** in Eq. 5.2. The presence of the ferromagnetic materials also introduces an additional interaction force F_{int} which can be decomposed to forces between the suspended magnet and the core, and smaller forces between the fixed magnet and top plate, and between the suspended magnet and shield. This reduces the static repulsive force experienced by the moving mass, $F_{static} = F_{mm} - F_{int}$. An analytical expression for F_{int} is difficult to compute, but can be assumed to be small, due to the small cross-sectional area of the core relative to the flux paths of the magnet. We accounted for

these effects using numerical simulations, from which we obtained values of F_{static} and F_{em} as driving current is varied.

5.3.2 Numerical simulations

We simulated the forces generated by the actuator using finite element analysis (FEA; COMSOL AB, Stockholm, Sweden). We developed an axisymmetric model of the actuator, and evaluated the axial magnetic force. The geometry and materials were specified to match the fabricated device (Sec. 5.6), with the dimensions as shown in Fig. 5.2A. The coil was modeled as a homogenized multi-turn structure. The ferromagnetic materials were configured as Nickel Steel Permalloy NGO, as defined within the COMSOL material library. The ferromagnetic materials were modeled with a BH curve relation. The ferrofluid was modelled as a homogeneous material with a relative permeability μ_r of 2, consistent with reported values. Representative surface plots of the magnetic flux densities through the cross-section of the actuator are shown in Fig. 5.2A.

When the electromagnet was not driven, the net force, $F_{static} = F_{mm} - F_{int}$, on the moving magnet was due to the opposing forces F_{mm} due to the magnetic bearing formed from the oppositely poled permanent magnets and F_{int} due to the attraction between the moving magnet and the core. The simulations predict that F_{static} decreases monotonically with the magnet-magnet distance d_{mm} (Fig. 5.2B). The relationship was approximately linear for distances $6 < d_{mm} < 7.5$ mm, attaining a value of 1.45 N for $d_{mm} = 7$ mm.

With d_{mc} held constant, the electromagnetic force on the moving mass F_{em} increased with the current (Fig. 5.2C). The relationship was nearly linear, notwithstanding potential flux saturation effects within the core, with a slope of 0.87 N/A for $d_{mc} = 2.5$ mm. This force was nearly four times larger than predicted from our simplified analytical model, highlighting the increase in the efficiency of the magnetic circuit achieved through the use of the ferromagnetic

elements. We also simulated forces for a configuration in which the ferrofluid was replaced with air. This configuration yielded smaller forces of 0.62 N/A. Thus, a 35% increase in forces was produced due to the greater magnetic permeability of the integrated ferrofluid.

To validate the previously considered analytical models, we performed simulations where we specified the physics model of all materials to utilize a relative permeability equation, and artificially set the magnetic permeability of the ferromagnetic components and ferrofluid to be 1. The modified FEA simulations subsequently predicted $F_{mm} = 0.32$ N, and $F_{em} = .2$ N/A. The electromagnetic force F_{em} predicted by the simulation is in excellent agreement with the analytical model. The analytical model overestimates the repulsive forces between magnets F_{mm} by 85% when compared to simulations, which we hypothesize to be due to the far-field assumptions made in the derivation of the analytical expressions not being fully met.

To investigate effects of lateral displacement of the moving magnet, we simulated configurations in which the magnet center was offset from the axis of the electromagnet. While the magnet position is constrained, in practice, by the membrane, the simulation revealed that it is positioned in unstable equilibrium in the radial directions. A radial offset of 1 mm introduced a radial force F_r of 1.3 N, and also yielded a net torque of 2×10^{-4} Nm. Such effects can yield ancillary linear or torsional oscillations in the absence of constraining features. We revised our design to minimize such effects via a guide bearing formed by extending an aluminum shaft from the magnet into a hollow region of the core (Part B in Fig. 5.2A). The shaft and bearing did not modify the electromagnetic performance, but modestly affected the dynamics of the system, as described in the following section.

5.4   Mechanical modeling

We constructed an analytical model capturing the static and dynamic behavior of the actuator. The actuator performance depends on several factors, including the membrane elasticity,

inertia of the moving elements, and dissipative forces caused by the viscous fluid within the actuator.

5.4.1   Static Forces

The forces acting on the moving magnet assembly include the force F_{em} produced by the electromagnet, the repulsive force F_{static} between the permanent magnets, the force F_{mem} due to membrane deformation, and the viscous force F_{drag} due to the encapsuated fluid. A free body diagram of forces on the moving mass is shown in Fig. 5.2C.

When the coil is not energized, if the system is in static equilibrium, then $F_{static} - F_{mem} = 0$ and $F_{em} = F_{drag} = 0$. Applying an additional static load force F_{load} to the surface of the moving magnet assembly will displace it from this equilibrium. For sufficiently small static load forces, a new equilibrium is reached, satisfying

$$F_{static} - F_{mem} = F_{load} - F_{em} \tag{5.5}$$

The force due to gravity is far smaller, due to the low mass of the moving magnet assembly, and thus may be neglected.

5.4.2   Membrane Model

The actuator is designed to accommodate application-dependent pre-loading of the membrane and mass via fluidic pressure or external forces. We omit this effect in a first analysis. Thus, the membrane displaces by an amount δ such that the membrane restoring force, F_{mem}, is equal to the net force exerted on the magnet by the electromagnetic circuit to reach static equilibrium.

106
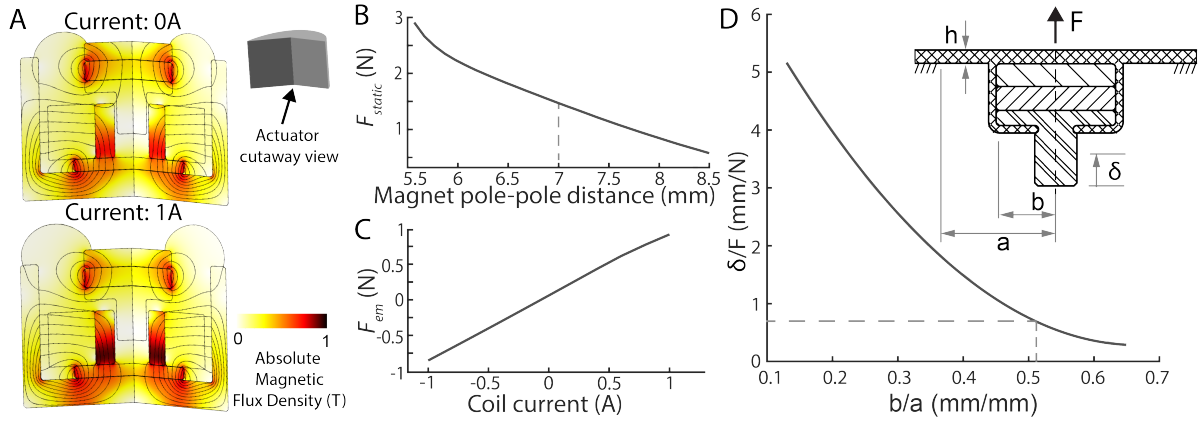
Figure 5.2: Modeling and simulation results utilized in the design of the actuator. A) Numerical predictions of magnetic flux densities within the actuator for varying current levels within its operating range. When driven at a DC current of 1 A, the ferromagnetic material in the core approaches its magnetic saturation. B) The static repulsive force experienced by the moving magnet F_{static} decreases monotonically with the the magnet-magnet distance. When coupled with the restoring force of the membrane, the representative magnet-magnet distance d_{mm} equals 7 mm for the moving mass in static equilibrium. C) The scaling of electromagnetic force F_{em} with current is approximately linear with a slope of 0.87 N/A. The scaling is computed to be sub-linear at large positive currents once magnetic saturation is reached. D) A plot of the deflection at the center of the diaphragm δ is shown as a function of force produced by the magnet assembly F, for $h = 0.5$ mm. The membrane performance can be optimized by varying dimensions a, b, and h. For the designed dimensions of the actuator, the predicted stiffness value is 1.25 N/mm.

Material Model

We adopted a linear material model for the membrane, which is reasonable because of the in-plane membrane strain is less than 50% across the range of operation. In principle, because the membrane is a fiber-reinforced elastomer, models of Kelvin-Voigt or Helmholtz types would be appropriate. However, manufacturing tolerances and unknown parameters governing the fiber alignment and concentricity of the assembly are challenging to obtain for laboratory produced devices such as ours, for which manufacturing tolerances are substantial. Additionally, the material properties of the elastomer matrix of the membrane can vary modestly from batch-to-batch. Thus, we adopted a simpler homogenized model of the elastomer membrane mechanics. The effects of fiber reinforcement are nonetheless important to capture, as our ac-

107

tuator was designed to take advantage of the beneficial effects they confer in limiting in-plane strains. Indeed, our primary objective was to model the more substantial out-of-plane displacements of the driven magnet. Based on representative values for the materials we designed the actuator to utilize, we adopted a value $E = 11.4$ MPa for the linear elastic modulus and $\nu = 0.5$ for the Poisson ratio. We determined these properties from laboratory tensile testing with rectangular samples of an elastomer material that we used in prototype fabrication.

Membrane Deformation

The geometry of the membrane was determined analytically for a circular membrane with a rigid center and a force acting at the center along the axis (Fig. 5.2D) [241]. The maximum deflection δ at the center of the membrane is given by

$$\delta = \frac{Fa^2}{Eh^3} \frac{3(1 - \nu^2)}{\pi} \frac{(a/b)^2 - 1}{4(a/b)^2} - \frac{\log(a/b)^2}{(a/b)^2 - 1} \tag{5.6}$$

Where F is the net force on the moving magnet, E and ν are the elastic modulus and Poisson's ratio of the membrane material respectively, and a, b, and h are geometric dimensions shown in Fig. 5.2D. An approximation for the effective spring constant of the membrane can be computed from Eq. 5.6 as $k_{\text{eff}} = dF/d\delta$.

5.4.3 Viscous Effects

The encapsulated ferrofluid augments the performance of the actuator by improving thermal transport, by reducing the magnetic reluctance of the electromagnetic circuit (thus amplifying forces), and by furnishing damping that reduces the Q-factor of mechanical resonances in the system. Damping of this form is often desirable in haptics, since it can increase an actuator's usable frequency bandwidth, which is typically constrained by the high-Q resonances in the system [225, 242].

A full fluid dynamics description of ferrofluid damping effects would be beyond the scope of the present contribution. A lumped parameter model may be obtained by regarding the combination of the guide shaft bearing and moving assembly (Fig. 5.2C) as comprising a dashpot, yielding a force

$$F_{drag} = -c\frac{dz}{dt} \tag{5.7}$$

Here, $z(t)$ is the displacement of the moving mass attached to the diaphragm, and c is the effective damping coefficient. For a fluidic piston-cylinder dashpot with clearance gap d, piston diameter D, piston length L, and dynamic fluid viscosity μ, the damping coefficient is given by

$$c = \frac{3\pi L\mu D^3}{4d^3}(1 + 2d/D) \tag{5.8}$$

For the parameter values describing our fabricated device (Sec. 5.6.2), Equation 5.8 yields a damping coefficient of approximately $c = 9.8$ Ns/m when the actuator is filled with ferrofluid. In contrast, if the same actuator is filled with air rather than ferrofluid, $c = 1.2 \times 10^{-3}$ Ns/m, which is four orders of magnitude smaller.

5.4.4   Dynamic Forces

When the coil in energized and the system is unloaded, the motion of the moving magnet system was modeled as a damped harmonic oscillator with a driving force $F_{em}(t)$ generated by the electromagnetic circuit,

$$m\frac{d^2z}{dt^2} = F_{em}(t) - c\frac{dz}{dt} - kz \tag{5.9}$$

where z and m is the normal displacement and mass of the moving mass element (bearing, moving magnet, and top plate; parts B, C and D in Fig. 5.2) respectively, c is the damping coefficient (Eq. (5.8)), and k is the stiffness of the membrane (Sec. 5.4.2).

The solution to (5.9) can be identified in the Fourier domain, with the undamped ($c = 0$) natural frequency of the system being denoted as $\omega_0 = \sqrt{k/m}$:

$$\hat{z}(\omega) = \frac{\hat{F}_{em}(\omega)(m(\omega_0^2 - \omega^2) - jc\omega)}{m^2(\omega^2 - \omega_0^2)^2 + c^2\omega^2} \tag{5.10}$$

For sinusoidal driving signals, $F_{em} = A\cos(\omega t)$, the solution is:

$$z(t) = \frac{A}{\sqrt{m^2(\omega^2 - \omega_0^2)^2 + c^2\omega^2}} \cos(\omega t - \phi)$$
$$\phi = \arctan\left(\frac{\omega c}{m(\omega^2 - \omega_0^2)}\right) \tag{5.11}$$

When $c/m >> 1$, the system is dominated by the damping, and the effect of the mechanical resonance is minimized. Such a system exhibits several properties that are desirable for a haptic actuator, with the acceleration d^2z/dt^2 being uniform across frequencies, and the system possessing a linear phase response.

5.4.5 Optimization of geometry

The results and insights from the electromagnetic and mechanical modeling were used to optimize the geometry of our fabricated device shown in Fig. 5.2. The actuator dimensions were specified in order to allow it to supply haptic feedback to the human fingertip. The diameter of the actuator was selected to be 18.5 mm, which is slightly wider than the average width of a typical adult index finger.

The diaphragm thickness h of the membrane could only be varied in manufacturing by 0.5 mm increments, based on the fixed thickness of the fabric reinforcement layer. In order to maximize the displacement, the minimum thickness of 0.5 mm was used. Without the reinforcement layer, lateral forces produced by the magnet assembly location being outside of the minimum concentricity tolerance cause the membrane to buckle and the magnet assembly to

rotate out-of-plane.

The dimension a was specified as 7.75 mm based on manufacturing and electro-mechanical considerations regarding the minimum thickness of the actuator housing. The dimension b was specified to obtain a membrane stiffness of approximately 1 N/mm, to ensure deformations within the displacement limits of the bearing, upon the application of forces. Based on this constraint and the available dimensions of commercially available rare-earth magnets, we selected the value of radius of all elements within the moving mass assembly b to be 3.97 mm. This resulted in a predicted stiffness of $k_{\text{eff}} = 1.25$ N/mm (5.2).

The fixed magnet placed at the bottom of the actuator was made as wide as possible to provide consistent static forces, even under the introduction of small radial offsets within manufacturing tolerances. Further, the thickness of this magnet was chosen to be the smallest available to minimize the magnetic reluctance it imposes in the flux path.

The coil was chosen to be wound with a wire of conductor diameter 0.255 mm (30 AWG), which imposes a steady state current limitation with its rating of 0.86 A. The bearing dimensions such as the clearance gap, and piston length (Sec. 5.4.3) were specified based on machining and fluid transport constraints.

We then considered the length of the core/coil assembly, the outer diameter of the core, the thickness of the moving magnet, the thickness of the top plate, and the distance between the moving magnet and core as free parameters, and optimized the geometry by running parameter sweeps with step sizes of .25 mm within our FEA numerical models. We identified the configuration that produces the largest electromagnetic force F_{em}. We also imposed an additional constraint during this process to verify that during regular operation within current limits, the sum $F_{static} + F_{em}$ is always positive. This ensured that the force never turned attractive during regular operating conditions, which would have caused the moving mass to adhere to the ferromagnetic core and introduce significant non-linearities.

5.5 Thermal modeling

The robustness of the proposed actuator depends on its thermal properties in addition to the electromechanical design. Compact electromagnetic actuators typically experience high temperatures due to the combination of resistive and induction heating with a small mass. As a result, thermal considerations often limit the utility of these compact actuators. We therefore carefully evaluated the thermal behavior of the actuator.

5.5.1 Actuator Features and Thermal Characteristics

Several design decisions shape the thermal characteristics of the actuator. The spacing between the suspended elements and the coil and the inclusion of a dashpot cylinder are justified by their impact on the mechanical performance of the device but introduce appreciable thermal effects. In particular, the aluminum linear bearing introduces a new conductive thermal path from the coil to the moving magnet. However, we explicitly introduced several measures to enhance the ability of the device to transfer the heat generated at the coil. Specifically, the internal cavity increases the heat capacity of the actuator, thus mitigating the rise in temperature due to heat generation. This feature also introduces the possibility of including a coolant liquid with a greater heat capacity than air, a role taken up by the added ferrofluid.

We identified three relevant temperature-dependent constraints for the device: the melting of the insulating coating of the coil wire, the demagnetization of the permanent magnets, and the degradation of the device's performance past the Curie temperature of Permalloy-80.

5.5.2 Thermal Behavior and Simulations

To examine the thermal response of the proposed design, we begin with a generalized description of the heat transfer problem for the actuator:

$$\rho C_p \frac{\delta T}{\delta t} + \rho C_p \mathbf{u} \cdot \nabla T + \nabla \cdot \mathbf{q} = Q + Q_{ted} \tag{5.12}$$

where T is temperature, t is time, ρ is the material density, C_p is the specific heat at constant pressure, $\mathbf{u}$ is translational velocity vector, $\mathbf{q}$ is the conductive flux, Q is the heat received from additional sources, and Q_{ted} is the heat dissipated through mechanical stress. To apply this governing equation to the intricate geometry of the actuator, we carried out a set of axisymmetric FEA heat transfer simulations in COMSOL. These numerical studies implement transient models of the device after two minutes of continuous operation. We used time-dependent solutions because the device's sealed configuration prevents it from reaching steady-state until after a few hours of operation. This figure is outside of the device's intended operational conditions, so we incorporated a time frame appropriate in the context of haptics.

The heat transfer models used the material properties listed in Table. 5.1. To account for the range of commercially available materials, we created two simulations to represent best and worst-case scenarios in terms of time to failure. We modeled the electromagnetic coil as a single material to eliminate the computational cost associated with its detailed geometry. To do so, we established an equivalent value of thermal conductivity for the coil using results from an auxiliary simulation [243]. The equation

$$G_{cond-rad} = \frac{\dot{Q}}{T_{max} - T_{wall}} \tag{5.13}$$

was used to calculate the effective coil conductance from this auxiliary simulation which only featured the coil, where $G_{cond-rad}$ is the radial conductance of the coil, $\dot{Q}$ is dissipated heat flux, T_{max} is the maximum temperature domain, and T_{wall} is the temperature imposed at the coil's upper edge. Equivalent radial conductivity (λ_{eq}^r) was then derived from the following expression

$$\lambda_{eq}^r = \frac{G_{cond-rad} \cdot e_r}{S_r} \qquad (5.14)$$

where S_r and e_r are the coil width and half-length, respectively. Additionally, the specific heat capacity of the coil was set to that of the wire insulator since it effectively limited the rise in temperature by surrounding the copper conductor.

In a preliminary analysis, we used an effective model of eddy current losses in wires [244] to determine that the heat generated within the bearing and the ferromagnetic components as fabricated was less than 0.1 W at 1000 Hz excitation, the highest frequency at which haptic actuators are driven. This analysis suggested that Joule heating in the coil was the dominant mechanism of heat production heat in the system.

We performed simulations with resistive heat generation at the coil and modeled natural external convection using Nusselt-number correlations for flat plates. Finally, we imposed appropriate thermal contact resistances at metallic interfaces using approximate surface roughness values and an interstitial air layer.

We repeated the analysis with currents varying from 0-6 A for configurations without a coolant and with ferrofluid. Preliminary results suggested that failure due to the demagnetization of the neodymium magnets is far more likely than the other modes. Subsequently, we shifted the focus of the simulations to this constraining factor. Representative results are included in figure 5.3. We defined the safety parameters with respect to the critical temperature for demagnetization ($T_{permissible}/T_{max}$). Subsequently, values less than 1 indicate potential failure. The simulations predict that at 1 A of input current (intended operational condition), no failure should occur within 2 minutes of continuous usage. The device is capable of handling greater currents over progressively shorter intervals of time (Fig. 5.3B). Finally, Fig. 5.3A2 juxtaposes the simulated temperatures to empirical results. This comparison validates the effectiveness of the simulations in predicting the device's thermal response. We carried out
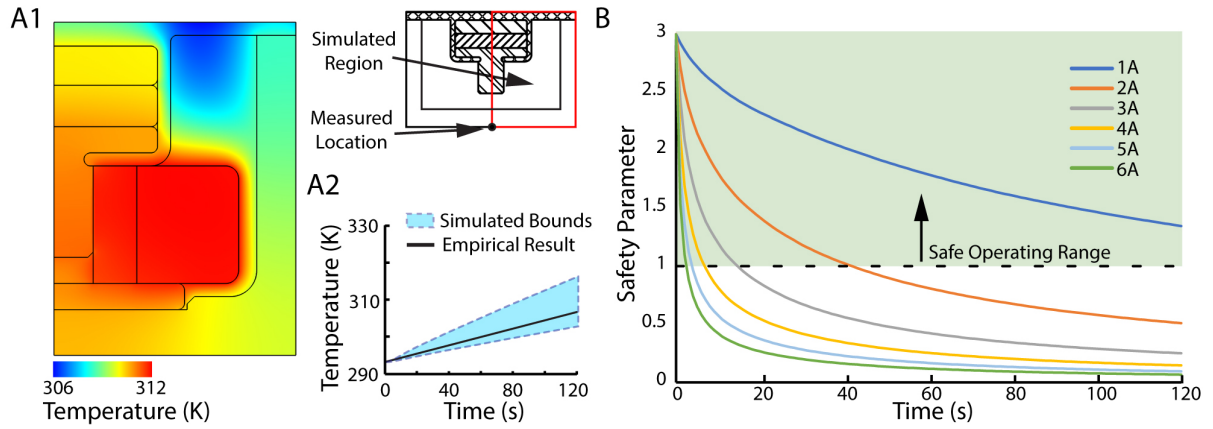
Figure 5.3: Sample results from the numerical models of the actuator's thermal performance. A1) Temperature plot after 120 s of operation of the ferrofluid-filled actuator at I = 1 A. A2) Time evolution of the numerically predicted temperatures in comparison to empirical measurements at the bottom of the canister for I = 1 A. B) Safety parameter at varying input currents plotted after 120 s of continuous operation. The sealed configuration means that the steady-state regime takes hours to set in; a time limit of 120 seconds of continuous use is implemented as a reasonable sustained operational condition in a haptics experimental setting. The results suggests that 1 of current can be driven through the actuator for more than two minutes, and larger current values can be safely used for shorter durations.

further testing on the individual coil to confirm the accuracy of the assumptions made about material properties. The results of our thermal models indicate the device's resilience against thermal failure when operated within the anticipated current range and over limited periods of continuous use.

Material	Heat Capacity ($\frac{J}{kgK}$)		Thermal Conductivity ($\frac{W}{mK}$)		Density ($\frac{kg}{m^3}$)		References
	Maximum	Minimum	Maximum	Minimum	Maximum	Minimum	
Permalloy 80	502.42	494.34	34.61	19.66	9992.45	8740.00	[245] [246]
N50 Neodymium Magnet	502.42	460.55	8.96	6.16	7600.00	7500.00	[247] [248]
Thermal Epoxy	1100	1038.25	5.76	0.17	1150.00	1150.00	[249] [250]
Wire Insulator	2300.00	1090.00	0.35	0.15	1540.00	1380.00	[251]
Ferrofluid	4000.00	1500.00	0.80	0.60	1200.00	1000.00	[252] [253]

Table 5.1: Material properties used in the thermal models of the actuator.

5.6   Fabrication

The materials used for the prototype actuator were all chosen to meet specified require-
ments and optimize the performance, as described below. We then present the steps used for
fabrication of the actuator. All parts are labelled as in Fig 5.2.

5.6.1   Material Selection

Fiber-reinforced silicone membrane (part E): Ecoflex 00-30 platinum cured silicone was
chosen because of its durability and similar softness to human skin [254]. While the silicone
provides a desirable mechanical response, it is capable of many hundreds of percent strain.
With the translation of the moving mass being unconstrained, the force experienced by the
permanent magnet could displace the bearing out of the shaft and even rupture the membrane.
A 4-way stretch knit fabric was added to reinforce the membrane and limit its displacement.
During the assembly process the fabric reinforcing layer is embedded in the silicone matrix as
detailed in section 5.6.2.

Magnetic circuit components (parts D, H, and G): For the metal components that make up
the magnetic circuit, we used a soft nickel alloy composed of 80 percent nickel, 4.4 percent
molybdenum, and 15.6 percent iron (Permalloy 80, ESPI Metals, Ashland, OR), a material
often used for high-performance magnetic applications. These components were machined
from billet stock and then annealed in accordance with ASTM A753 for Type 4 materials.
The equipment available could not produce the 'dry hydrogen' atmosphere specified, however
we were able to heat treat the material at 1150 C and quench at 300C per hour with flow-
ing hydrogen. As a result, the magnetic saturation of the alloy increased by 8% to $\approx$ 0.9 T,
and the magnetic permeability remained approximately unchanged, as measured by a SQUID
magnetometer (MPMS, Quantum Design, San Diego, CA).

Permanent magnets (parts C and J): We chose neodymium magnets sourced from commer-

116

cial vendors (D51-N52, KJMagnetics, Pipersville, PA; and D1058, SuperMagnetMan, Pelham, AL for magnets C and J respectively).

Bearing (part B): A critical alignment and damping feature, the bearing was fabricated from 2024 aluminum. Aluminum was chosen in order to withstand the heat generated by the electromagnet, and minimize the weight of the moving mass.

Fluid displacement feature (part F): As the ferrofluid which we incorporate is an incompressible fluid, the design needs to account for a reservoir that allows for the fluid to displace into it during the motion of the moving mass. For the assembled prototype, we implemented this with a thin tube (Φ_{ID} = 3 mm) which is ported to the side (Fig. 5.6A).

5.6.2   Fabrication

All of the metal components were fabricated from billet stock using traditional machining and turning methods. The nickel alloy parts were subsequently heat treated as described in the previous section. The core (part H) was sent to a coil fabricator to accurately wind the electromagnet coil (part K). The coil winding should be tightly packed to maximize efficiency and minimize volume for space efficient packaging. The manufacturer of the coil attempted to achieve hexagonal packing of the windings, however tolerances on the winding machine resulted in a combination of hexagonal and square packing reducing the field strength from the theoretical maximum. The annular core facilitates the winding operation, gives an alignment feature for the upper magnet in the diaphragm by locating part B, and provides the cylinder feature for the dashpot made from parts B and H.

The fabrication process has four critical steps to ensure effective operation of the actuator as seen in Fig. 5.4:

 (A) Parts D, C, and B are assembled in a stack and added to a mold with the fiber reinforcing fabric laid on top. The assembly is then encapsulated with Ecoflex 00-30.
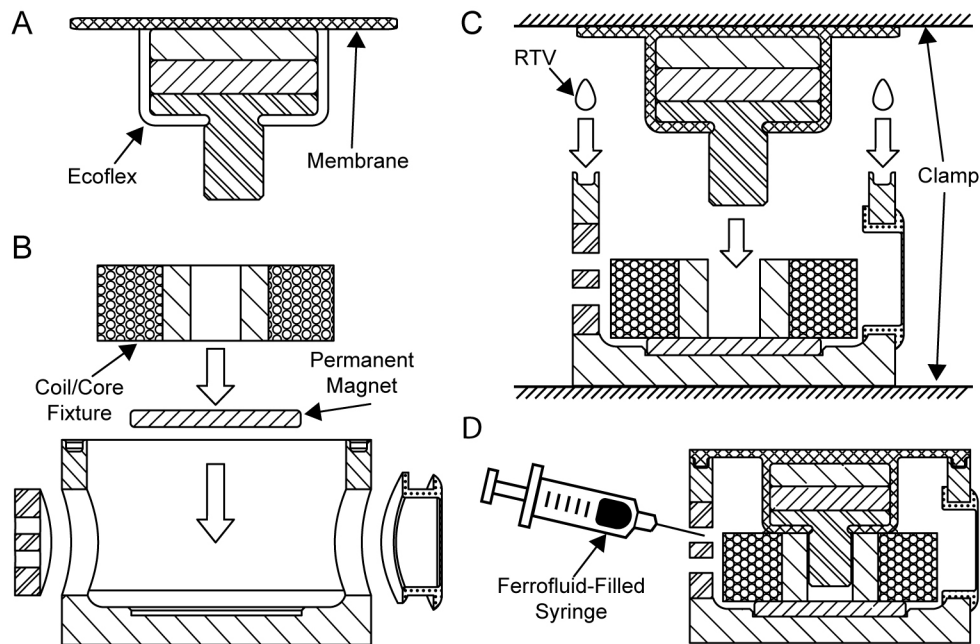
Figure 5.4: The fabrication process as described in section 5.6.2.

(B) The wire and filling port A, and fluid displacement feature F are added to the housing G. The lower permanent magnet J sticks to a shallow cavity in the housing G. The electromagnet coil assembly (parts H and K) is stuck to the top surface of the magnet and roughly centered. The wires from the electromagnet are passed through the wire outlet in A.

(C) Sub-assemblies described in steps (A) and (B) are placed in an alignment fixture, and a bead of room temperature vulcanizing silicone (RTV) is applied to the sealing surface. The fixture then marries and clamps the final assembly. During this process the aluminum piston fits into and concentrically locates the electromagnet core.

(D) Once the RTV is cured, the final assembly is removed and filled with ferrofluid. The tube comprising the fluid displacement feature is finally clamped away from the actuator to seal the system.

5.7   Characterization

To evaluate the performance of the constructed actuator, we performed a combination of dynamic, quasi-static, and thermal characterization. The dynamic performance was studied through transfer function, step response, and discrete sinusoid measurements. Next, the quasi-static forces produced in an isometric configuration were measured in steady state operation. Finally the thermal characteristics of the actuator were measured by recording the increase in temperature during steady state operation.

5.7.1   Apparatus and procedure

The actuator was mounted in a fixture and bolted to an optical table to reduce ambient vibrations. Measurements of the actuators performance were recorded via laser doppler vibrometer and force transducer, which were also mounted to the optical table.

A laboratory amplifier (PA-138, Labworks Inc., Costa Mesa, CA) was used in voltage control mode to drive the actuator, and measurements were taken with a data acquisition system (USB-6211, National Instruments, Austin TX) controlled by a computer. The current through the actuator was measured, and proportional control was used to provide specified input currents. Data was collected from a prototype both with and without ferrofluid.

The unloaded dynamic response of the ferrofluid and air-filled actuators were characterized with a 1-axis non contact laser doppler vibrometer (PDV-100, Polytec Inc., Irvine, CA). A thin piece of retro-reflective tape was attached to the center of the moving mass, which served as the position at which measurements were taken. A linear frequency sweep (1-1000 Hz, 10 sec, 5 repetitions) input signal at different current values (0.1, 0.2, 0.5, 1 A peak) was used to compute the frequency response of the actuator. A square wave (2 Hz, 5 sec, 5 repetitions) was used to estimate the step response of the actuator for the same current values discussed above. Measurements were also taken for sinusoidal signals (20 discrete frequencies logarithmically

spaced between 5 and 1000 Hz, 5 secs, 5 repetitions) at 0.25, 0.5 and 1 A peak currents. This allowed the computation of peak-to-peak displacements (A_{pp}) and total harmonic distortion (THD) values at these discrete frequencies.

To investigate the influence of the fluid displacement feature on the actuator dynamics, the unloaded dynamic responses were measured with the clamp location on the ported tube varied between 2 and 5 cm from the end of the actuator. The minimal length of 2 cm was determined by the structure of our fixture. The clamp location was set to 5 cm for the reminder of the measurements.

After the construction of the actuator, static force measurements between the magnets can no longer be isolated due to the intrinsic interaction with the membrane's restoring force. Rather, the electromagnetic force output F_{em} of the actuator was characterized at different operating displacements, using a 6-axis force transducer (Nano17 F/T Sensor, ATI Industrial Automation, Apex, NC). In order to eliminate any magnetic interactions between the actuator and transducer, and reduce the contact condition to a point load, a 2.5 cm long custom cylindrical probe with a hemispherical tip was 3D-printed from ABS and fitted to the force transducer. A 3-axis spirit level was used to ensure that the transducer was level. A laser displacement sensor (IL-1000, Keyence Corporation, Itasca, IL) was used to measure the relative displacement of the moving mass along its stroke with a resolution of 10 μm.

Once the transducer was positioned and the displacement recorded, the transducer was tared for more accurate measurements. The actuator was then driven with a stepped signal that varied from -1 A to 1 A DC in 0.2 A increments, and the force values were recorded. Each trial was repeated 3 times. A delay of 2 minutes was introduced for thermal reasons, and the procedure was repeated a different position along the actuator's displacement range, with measurements taken along 3 different points between the top and bottom of the stroke, each separated by 0.5 mm.

To characterize the thermal performance, a K-type thermocouple was affixed to the bottom

of the canister with tape, and thermal measurements were taken with a digital thermometer (Fluke 52 II, Fluke Corporation, Everett, WA). This configuration was taken to represent the worst-case scenario for heat buildup, as all the metal surfaces of the actuator were enclosed within the insulating surfaces of the ABS fixture and tape. The actuator was driven with a 1 A DC current for 2 minutes, and the temperatures were recorded with a sampling period of 5 seconds. Two trials of the thermal measurements were conducted for each actuator. The time taken for the actuator to cool down to room temperature was also recorded.

Finally, to test the limits of the actuator when driven with impulsive signals, the actuator was driven with a rectangular 10 ms wide pulse while measuring forces with the force transducer. The intensity was increased from 5 A in steps of 10 A, till we either approached the limitations of the utilized amplifier, or the actuator was driven to failure.

5.7.2   Results

The electrical properties of the actuator are dominated by its resistance and inductance. The resistance was measured to be 2.7 Ω, and its series inductance was measured to be 1 mH. All results are for the ferrofluid actuator, unless otherwise noted. For the R-L electrical load of the inductive coil, this results in a 3 dB point of 500 Hz. Beyond this frequency, the current through the actuator decreases by 20 dB/decade when driven by a fixed voltage.

The unloaded dynamic responses differ greatly for the air-filled and ferrofluid actuators (Fig. 5.5A). The air-filled actuator shows a prominent resonance at 165 Hz (Q = 3.8), with peak-to-peak accelerations of 64 g's for a 0.5 A peak current input (1 g = 9.8 m/s^2). This prototype was strongly non-linear when driven at larger currents. In contrast, no resonance was observed for the ferrofluid actuator within 1000Hz, and the response is essentially flat in the frequency domain beyond 300 Hz. At frequencies up until 40Hz, the ferrofluid actuator has accelerations larger than the air-filled prototype by an average of 6 dB. At low frequencies,

121
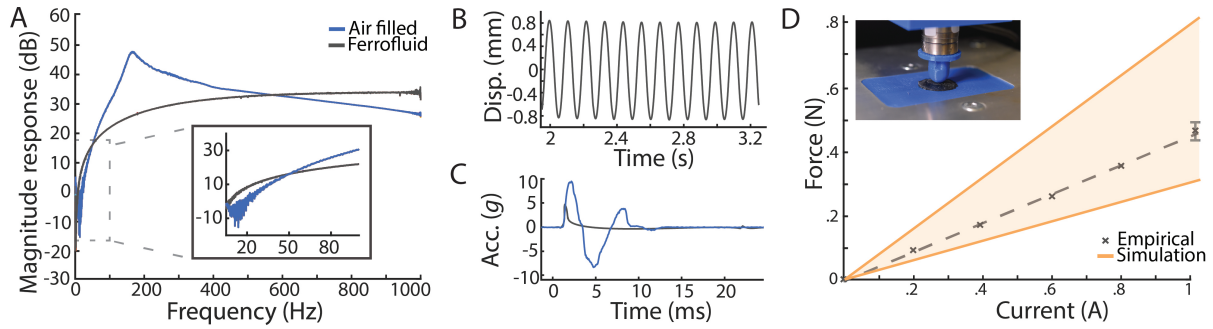
Figure 5.5: Characterization results. A) The dynamic response of the unloaded actuator, computed as the transfer function between the voltage applied to the actuator and the measured acceleration in m/s^2. The air-filled actuator exhibits a resonance at 165 Hz, while the presence of viscous damping makes the ferrofluid actuator an overdamped system with no resonance. At low frequencies under 50 Hz, the ferrofluid actuator also exhibits larger accelerations when compared to the air-filled prototype, due to the increase in magnetic permeability within the actuator. B) Displacements of the moving mass of the ferrofluid actuator for an 8.5 Hz, 1 A amplitude sinusoidal current input. At low frequencies, the accelerations are limited by the displacement limits of the actuator. Peak displacements (800 μm) fall in line with values predicted by the membrane stiffness and force outputs. C) Step response of the actuators, with a 0.5 A stepped current input. The step response of the air filled actuator is dominated by its resonant frequency, and rise times average 12 ms. In contrast, the ferrofluid actuator exhibits a sub-2 ms rise time. D) Quasi-static loaded force measurements of ferrofluid actuator vs direct current (DC). Error bar denotes the standard deviation of the measurement at 1 A. We measure a force output of 0.45 N/A from the actuator in the central region of its stroke. The force values predicted by numerical simulations were highly dependent on the material model used for the permalloy, we therefore present the range of predicted force outputs for varied B-H curves of high-nickel steel alloys. Inset picture - Actuator within the measurement fixture, placed under the force transducer.

the peak accelerations are displacement limited. The responses shown are consistent across different input current levels, with the transfer functions independently computed from the 0.1 A and 0.5 A peak current measurements only differing by 0.2 dB on average.

The measurements for discrete sinusoidal signals show that for the ferrofluid actuator, the peak full scale displacements A_{pp} at low frequencies under 50 Hz approaches 1.6 mm for a 1 A peak input (Fig. 5.5B). At high frequencies, peak-to-peak accelerations of the air-filled and ferrofluid actuators are comparable, at 20 and 23 g's respectively for a 750 Hz 0.5 A peak current input.

The air filled actuator was highly non-linear at a high currents, particularly below reso-

nance. The computed THD values averaged -15 dB when driven with a 0.5 A peak current signal at frequencies below 150 Hz, and averaged -30 dB above the resonance. The ferrofluid actuator was more linear, with THD values averaging -37 dB across the frequency range at identical current input. Even with 1 A peak current inputs, the THD of the ferrofluid actuator never exceeded -23 dB.

The air-filled actuator has its step response dominated by its resonant frequency, with rise times averaging 12 ms, which corresponds to 2 cycles at 165Hz (Fig. 5.5C). Peak-to-peak accelerations averaged 19 g's for a 0.5 A current step. The ferrofluid actuator showed a rise time of 2 ms, just marginally above the rise time of the current pulse (1 ms). Peak accelerations were computed to be 4.7 g's for a 0.5 A current step. The responses for the air filled actuator were highly non-linear at larger current steps. The responses of the ferrofluid actuator were similar over the range of clamp locations considered, with less than 1 dB of difference between them over the frequency bandwidth (Fig. 5.6B).

The peak electromagnetic force measurements when the actuator was measured in the middle of its designed stroke, at 0.45 N/A (ferrofluid) and 0.295 N/A (air filled) (Fig. 5.5D). At the bottom of its stroke, the actuator delivered 0.32 N/A (ferrofluid) and 0.21 N/A (air filled). At the top of the stroke, the specific force outputs were 0.34 N/A (ferrofluid) and 0.23 N/A (air filled). When driven by impulsive 10 ms pulses, peak forces of 12 N were measured from the ferrofluid actuator with a 38 A current pulse, at which point we hit upon the limitations of the employed amplifier.

The temperature of the ferrofluid-filled actuator measured at the base increased by 13.5 °C when driven by 1 A DC for 120 seconds. The air-filled actuator, in contrast, had its temperature rise by 17.6 °C. For both actuators, it took approximately 100 seconds per °C to cool back down to room temperature.
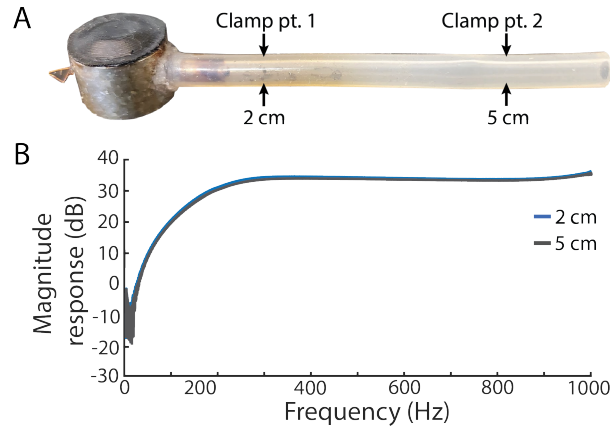
Figure 5.6:   Analysis of fluid displacement feature and impact on device performance. A) To allow for an incompressible fluid to displace during the translation of the moving mass, we ported the ferrofluid-filled actuator with a tube (Φ_{ID} = 3 mm). The tube was clamped tightly to seal the system, with the resulting air column acting primarily as a spring. B) Empirical unloaded dynamic response for different lengths of the air column. The results vary only marginally (< 1dB) for different column lengths (2 vs. 5 cm), suggesting that a minimally compact feature that allows for the ferrofluid volume to displace into it will perform identically.

5.7.3   Discussion

The results show how the actuator can reproduce frequencies from DC (constant forces) to 1000 Hz, with the accelerations achieved through the ferrofluid actuator flat in the frequency domain beyond 300 Hz. The phase response of the system was measured to be linear. The broad frequency response alongside the low harmonic distortion levels allows for the controlled reproduction of various high-fidelity haptic effects using this fluidic actuator.

A comparison of the unloaded responses of the air-filled and ferrofluid actuators shows how the viscosity of the ferrofluid in conjunction with the aluminium dashpot introduces significant damping, which makes it an over-damped system (calculated damping ratio = 4). This minimizes the influence of any mechanical resonance on the dynamics of the system, as evidenced by the unloaded dynamic and step responses.

At low frequencies, the device is dominated by the stiffness and limited by peak displacements; i.e. at a given force output from the electromagnet F_{em}, the membrane does not dis-

place more than F_{em}/k_{eff} from the equilibrium point, limiting the unloaded accelerations. As an example, within the stiffness controlled regime, fixed amplitude sinusoidal displacements $z = c \cdot \sin(2\pi f t)$ result in accelerations which increase with frequency f -

$$a = d^2 z/dt^2 = (2\pi f)^2 z$$

Indeed, at low frequencies below 40 Hz (Fig. 5.5A Inset), the measured accelerations increase with increasing frequency at the expected 40 dB/decade rate. At these frequencies, the generated displacement is a more useful metric for device performance than the acceleration, and the fabricated actuator achieves peak-to-peak displacements of A_{pp} = 1.6 mm for currents $I =$ 1 A.

For signals which cause large displacements of the moving mass along the stroke, such as large current inputs at low frequencies, or around the resonance of the air-filled actuator, we observe non-linearities as evidenced by the THD measurements. These are due to both the hyper-elasticity of the membrane constraining motion at the top of the stroke, and the hard mechanical limit at the bottom of the stroke. The variation of F_{static} with displacement could also play a role. We measured an effective stroke length of 1.25 mm over which linearity can be assumed, with measured THD values below -30 dB over all examined frequencies. This stroke length along with the minimal rise and fall times (Fig. 5.5C) allows a haptics designer to position the actuator with a slight clearance to the fingertip, and deliver sensations of transient or constant contact in addition to vibrations, through the application of impulsive or DC currents.

The only additional dynamics introduced with the fluid displacement feature as implemented is the stiffness introduced by the air column within the tube, which we computed to be negligible in relation to the stiffness of the membrane. To empirically verify this, we repeated the unloaded dynamic responses at varying clamp locations (Fig. 5.6). The results suggest that

for the frequencies of interest for haptic applications, a minimal (≈ 60 mm^3) fluid displacement feature would result in identical performances.

In static equilibrium with zero input currents, we measured representative membrane deflections of $\delta = 1$ mm. Paired with the predicted membrane stiffness value of 1.25 N/mm, this provides an estimate of $F_{static} = 1.25$ N. This is marginally lower than the prediction of 1.45 N made by the numerical models (Fig. 5.2) for an equivalent magnet-magnet distance of $d_{mm} = 7$ mm.

The electromagnetic force outputs of the actuator, while significantly higher than the simplified analytical models and those achieved by comparable commercially available actuators, were lower than that predicted by the numerical models (Fig. 5.5D). On further inspection and with magnetic characterization of the Permalloy-80 samples, we came to the conclusion that the annealing process during the fabrication was unable to fully optimize the magnetic performance of the metal. The properties of the material such as its saturation field strength have large effects on the theoretical performance of the device, as seen by modifying the FEA model to utilize the B-H curves of different high-nickel steel alloys. Our empirical measurements fall within the range of predictions. We hypothesize that the peak forces can be improved by nearly 60 % within the current design by further optimizing the metallurgy of the components.

The performance of the actuator was compared with vibrotactile actuators available from commercial vendors (ERM - Model 310-003, Precision Microdrives, London, UK; Haptuator Mk II, Tactile Labs, Montreal, Canada; C-2 Tactor, Engineering Acoustics, Inc., Casselberry, FL; LRA - Model C10-100, Precision Microdrives; Piezo - Model 2626H023V120, TDK Electronics, Tokyo, Japan) (Table. 5.2) . The constructed actuator is unique among electromagnetic actuators in its ability to generate constant forces, and its wide frequency bandwidth. While piezoelectric actuators can deliver comparable sensations in bipolar operation, their utility is hampered by complex driving requirements, small displacements, and thermal constraints at high frequencies. In contrast, the constructed fluidic actuator can be driven through simple

commodity electronics.

	Constructed Actuator	ERM	Haptuator Mk II	C-2 Tactor	LRA	Piezo
Volume (cm^3)	3.4	0.27	5.2	1.5	0.3	1.6
Weight (gram)	19.5	1.1	8.7	17	2	6.7
Operating / rated frequency (Hz)	DC - 1000	167	90 - 1000	200 - 300	175	DC - 500
Maximum displacement range (mm)	1.25	-	-	1	-	0.025
Static force (N)	0.45	-	-	*	-	4.5
Peak-to-peak accelerations (g)	46 (unloaded)	0.9	8	*	1.5	32
Rated power draw (W)	2.7	0.06	0.3	1	0.046	*

Table 5.2: Comparative table of vibrotactile actuators (* indicates lack of publicly available data)

The thermal behavior of the actuator, as validated through empirical measurements, enables us to generate its sustained force output of 0.45 N for a duration of two minutes or more, while using a power of 2.7 W. However, most haptics applications rarely utilize forces or vibrations over such long durations. More interestingly, the thermal simulations also predicted that currents as high as 6 A could be safely used for 3 seconds without causing the actuator to fail, which predicted the possibility for larger transient force outputs. We verified this by investigating whether the actuator would fail through the application of large amounts of currents, over a short duration of 10 ms. The actuator was still functional at the end of this testing, and we measured peak force outputs of 12 N for 38 A of current. The scaling of the force was sub-linear for currents above 2 A, which we had predicted due to the effects of magnetic saturation. Nevertheless, these measurements showcase a much larger dynamic range of forces can be achieved for short durations.

For applications where the finger firmly applies a load to the actuator, the mechanical system of the actuator is coupled to the dynamics of the skin. Estimates for the stiffness of the skin of the digits range from 0.25 to 1 N/mm [255], which is smaller than the membrane stiffness discussed here, but of the same order of magnitude, which suggests a strong coupling. Therefore, the forces and displacements applied to the skin in a practical setting would require additional analysis, which we aim explore in future work alongside specific haptic evaluations.

5.8   Evaluating Unique Capabilities of the Haptic Actuator

This compact haptic actuator is capable of reproducing mechanical signals in several regimes that cannot be reproduced in a controlled fashion using conventional haptic actuators, particularly those suitable for wearable applications, including sustained forces (near DC frequencies), transient contact, and very low frequency vibrations. The last of these makes it uniquely well suited to reproducing the dynamic spatiotemporal sensations discussed in Chapter 4.

To demonstrate this, we designed a wearable interface and used the same paradigm invented in the research described in chapter 4 to evaluate whether the compact haptic actuator can convincingly reproduce spatiotemporal effects. In comparison with the electrodynamic shaker previously used for the experiments in Chapter 4, the designed haptic actuator is smaller in each linear dimension by one order of magnitude, and in mass by two orders of magnitude, enabling its integration into a wearable form-factor.

5.8.1   Wearable interface design

We designed a wearable interface that allows the actuator to be positioned underneath, and provide normal indentations to, the fingertip. To accomplish this, the actuator is placed in a fixture within a rectangular frame. A lead screw is used to translate the position of the fixture, to accommodate for variations in the size of fingers (Fig. 5.7A). An overhang plate was added to the frame, to allow for reaction forces to be spread throughout the length of the finger when the actuator is reproducing sustained forces. This enables the delivery of simple kinesthetic cues, a challenge for most wearable devices [120]. We 3D printed a prototype made of ABS plastic for the experiment (Fig. 5.7B). Velco straps were used to attach the interface to the finger.
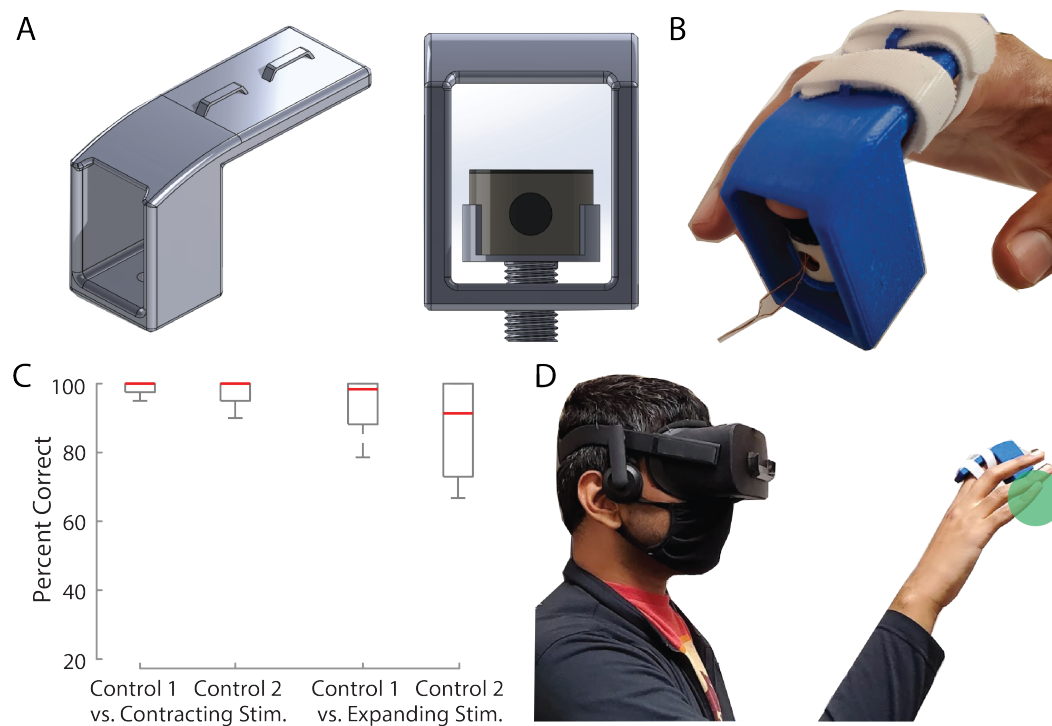
Figure 5.7: Evaluation of the designed actuator in a wearable setting. A) 3D model of the wearable interface to place the actuator on the skin. A rigid plate extends along the length of the finger, and maintains contact with it through the use of velcro straps. A fixture is used to hold the actuator underneath the overhanging plate. A lead screw is used to translate the position of the fixture. B) Image of the actuator and interface worn on the index finger of the hand. C) Results of the perceptual experiment. Participants consistently reported the designed stimuli to be spatiotemporally varying, with this compact, highly portable actuator (median accuracy $> 90\%$). D) In an example interactive application, the ability to generate constant and low-frequency forces can be used to recreate sensations of contact with virtual objects, in addition to vibrotactile feedback.

5.8.2   Perceptual experiment

Four participants volunteered for the experiment. The participants were naïve to the purpose of the experiment, and had not previously experienced the spatiotemporal effects. Participants were seated, and the wearable device was fitted to their index finger of their left hand. The positioning of the lead screw was adjusted to ensure that the finger was held in consistent contact with the moving mass of the actuator. The procedure, stimuli and analysis of the experiment was identical to that employed in the previous chapter (Sec. 4.5). In brief, the

designed "expanding" (EX) or "contracting" (CO) stimuli were presented alongside control stimuli which had no systematic variations in frequency bandwidth over time. For every trial, participants were presented with one designed stimulus (EX or CO) and one control stimulus, an animated visual representation matching the presented designed stimulus, and reported which of the two stimuli resulted in perceptual sensations closest to the visual representation.

5.8.3   Results and discussion

Without prior training, participants consistently associated the designed stimuli with the visual representations of "expanding" or "contracting" (Fig. 5.7C). The designed stimuli were selected with median probability of nearly 100% (CO stimuli: 100%, EX: 92%). The percentage correct scores were substantially greater than a positive effect threshold of 75%, showing how the developed actuator can consistently reproduce complex haptic stimuli in a controlled fashion, in a manner similar to much larger laboratory equipment. Further statistical tests were not performed in light of the limited sample size.

In a post-hoc experiment, participants were asked to repeat a few trials of the experiment with the electrodynamic shaker. Participants were able to clearly identify the directionality of the spatiotemporal effects with both actuators, although some participants reported perceiving marginally smaller variations in the spatial extent with the compact actuator, likely due to smaller displacements achieved at low frequencies.

The results highlight the ability of the developed actuator to generate high-fidelity vibrotactile sensations. We also experimentally verified that the actuator can present forces to the finger, through the application of constant or impulsive signals. We hypothesize that the ability to bring the actuator in and out of contact with the finger can therefore allow it to generate sensations of touching virtual objects (Fig. 5.7D), which we plan to evaluate in future work.

5.9   Conclusions

We present a novel haptic actuator design based on the interaction forces between permanent magnets and an electromagnetic coil, which utilizes an elastic membrane to provide the restoring force to a moving mass that is coupled to the skin. The actuator incorporates fluidic elements to optimize the mechanical response across a large range of frequencies. Through careful and considered design, we obtain large forces (0.4 N sustained, > 10 N transient), which can be utilized to provide indentations and vibrations to the skin. The wide range of reproducible frequencies from DC to 1000 Hz enables the effective delivery of vibrations through the entire tactile range of sensitivity of the skin. The thermal design ensures that actuator can be used to provide sustained stimuli for two minutes or more. This high-fidelity actuator exceeds the comprehensive performance achievable through comparable state-of-the-art actuators, and can reproduce varied and rich tactile stimuli.

Due to its compact size, this actuator can be easily implemented in a wearable form factor. In addition, the ferromagnetic actuator housing constrains most flux lines within it, acting as a form of magnetic shielding. This makes it advantageous for the design of multi-actuator setups, as individual actuators can be brought close together with low cross-interference. This design shows great promise for the development of haptic displays consisting of a spatially dense grid of high-fidelity actuators.

Chapter 6

Design of Distributed Optoelectronic Skin for Haptic Feedback via Light Fields

A longstanding goal in haptic engineering for virtual and augmented reality is to realize practical technologies and devices that furnish touch sensations to the skin – the sense organ of touch. This has proved challenging due to the large spatial extent and substantial spatial resolution of the skin. A further challenge arises from the complex shape and movements of the hands. While electromagnetic actuators, such as those discussed in Chapter 5, are exceedingly versatile, they are difficult to make flexible and to miniaturize for use in simultaneously stimulating extended regions of the skin. This chapter presents new methods for the design of distributed skin-interfaced functional soft devices, and describes the design of a display capable of delivering electrotactile stimulation to multiple locations of the finger on directed exposure to light, enabling the skin to "see" optical patterns. This research facilitates the construction of flexible haptic displays that can provide spatially programmable haptic feedback over large areas of the skin, and are thus tailored to the distributed nature of tactile perception.

At the time of writing, content of this chapter is in preparation for eventual submission to

an interdisciplinary journal with the provisional title:

S. Biswas[*], B. Dandu[*], Y. Shao, D. Goetz and Y. Visell, "Stretchable Optoelectronic Skins for Haptic Feedback via Light Fields".

[*] These authors contributed equally.

Abstract

A longstanding goal in haptic engineering has been to realize electronic displays for stimulating the sense of touch that can mirror the sensing characteristics of the skin, in ways that are analogous to how commodity video displays reflect attributes of the visual system through the reproduction of colors at varying intensities, with a high spatial resolution. Engineering such haptic devices with conventional methods has, however, proved far from feasible within the state of the art, due to the impressive spatial and temporal tactile sensing capabilities of the skin, paired with its complex structure. Here, we address this by proposing a new distributed haptic display technology that allows the skin to "see" by means of stretchable and wearable skin-interfaced electronics that translates programmable light fields into palpable sensations across wide areas of the skin. We describe the device design, fabrication methods, characterization, and physiological considerations that are essential for the development of this haptic display. The fabricated prototype integrates 14 stimulatable locations within a 8×2.5 cm surface, is thin and light (< 1.5 mm, < 8 g), and fully conforms to the fingers. This design is highly scalable, and can be applied over large surface areas of the skin. The characteristics of this device makes it suitable for haptic applications seeking to reproduce whole-hand sensations, such as in tactile augmented reality.

6.1   Introduction

Recent advances in virtual and augmented reality technologies make it possible for large numbers of people to experience the immersion of their visual and auditory senses within computer-generated environments. Although haptic feedback has been shown to improve immersion in VR/AR [256, 257], the sense of touch remains an under-utilized modality in human-computer-interaction when compared with vision and hearing. The reasons for this are varied. One challenge to realizing haptic displays that can stimulate the skin in a manner analogous to video displays is the sensitive, distributed, and multi-modal nature of human touch sensing. With the skin, we gather a wealth of information via touch, including location of contact, pressure, vibrations, and temperature, via the continuum of the skin surface. The spatial and temporal resolutions of touch sensing are high. Thus, it is a major engineering challenge to design haptic interfaces that can reproduce plausibly realistic touch sensations similar to those felt in naturally occurring interactions, and a further challenge to make such a device wearable. While many prior wearable haptic displays have relied on integrating arrays of discrete modular components into garments [122], such approaches can result in a bulky device when designed to deliver sensations over large areas of skin with high resolution. In contrast, thin and lightweight skin-integrated haptic interfaces hold promise for their ability to furnish haptic feedback without need for the use of encumbering devices or interfaces [99, 258].

Here, we present a new wearable skin-interfaced programmable haptic display technology for furnishing tactile patterns to the skin. This technology enables the skin to "see" projected optical patterns by translating patterns of light to electrotactile patterns that can be felt via the skin. We achieve this via modular (scalable) optoelectronic circuits formed on soft and stretchable polymer substrates that interface with the skin. The arrays of circuit elements transduce incident light to localized electrical current that is delivered to the skin. When combined with commodity optical projectors, they enable the skin to feel optically delivered patterns. Figure

134
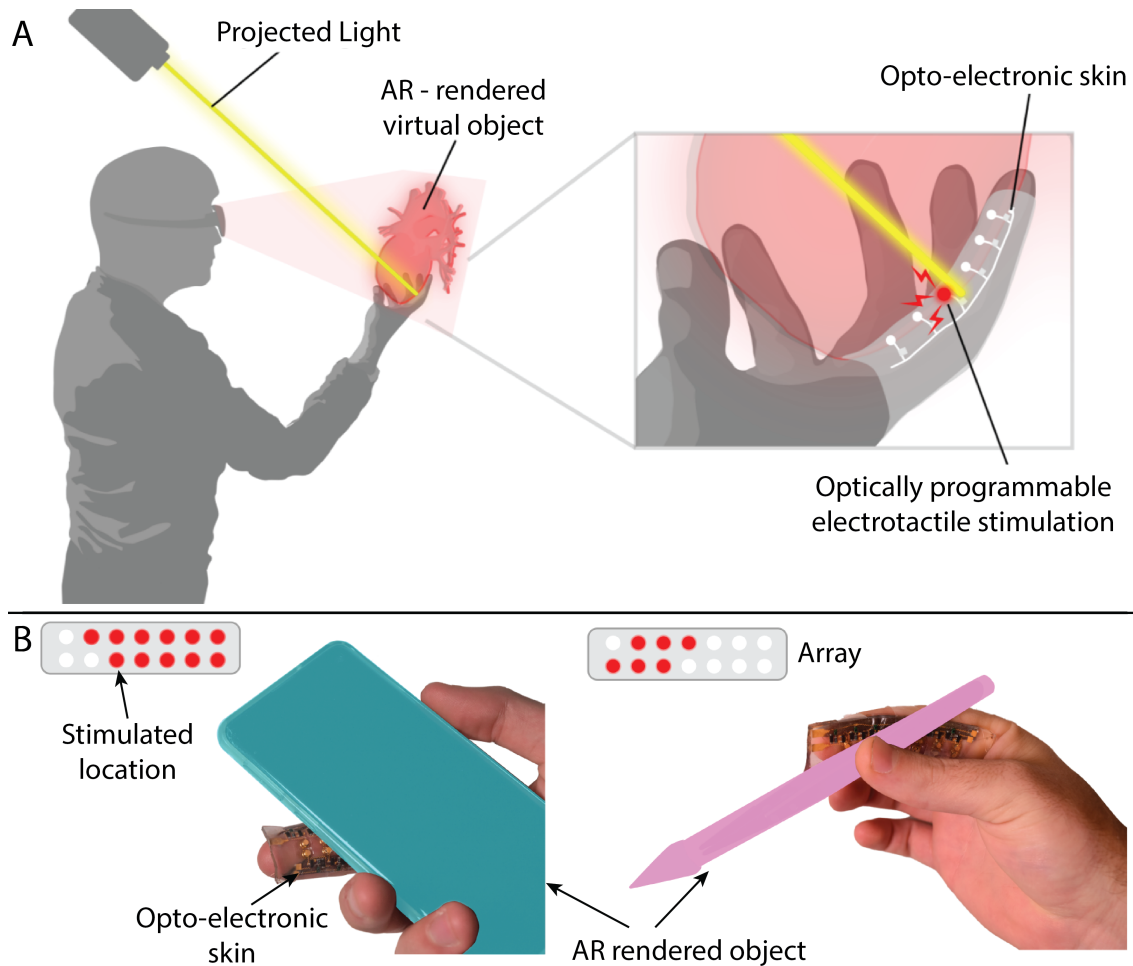
Figure 6.1: Illustrative application of the novel opto-electronic haptic display being proposed. A) The haptic display conforms to the fingers, and is optically controlled, allowing for a user to perceive virtual objects rendered by an augmented reality headset. B) The haptic display consists of an array of electrodes. Through careful alignment and programming of light fields, electrotactile stimulation is applied at the rendered contact locations (shown in red), allowing for the tactile identification of the geometry of virtual objects.

6.1 presents a schematic illustration of a potential application of this haptic display in augmented reality. This system can enable users to use their hands to feel 3D virtual objects in mid air, and may thus be integrated with three-dimensional visual displays such as augmented reality headsets. The location and intensity of haptic stimulation is programmable via media (images or video) presented from commodity video projectors. The design of this circuit facilitates the delivery of perceptually localized tactile sensations. We present new manufacturing

methods that make it possible to efficiently fabricate these highly functional artificial skins using standard processes. This research paves the way for the development of soft and wearable haptic displays that can deliver programmable tactile sensations with millimeter scale detail.

6.1.1   Background and proposed approach

While several methods for delivering touch sensations to the skin have been investigated, including vibromechanical actuation using electromagnetic, piezoelectric, and pneumatic transducers [86], electrotactile stimulation approaches provide several advantages that make them particularly well suited for delivering high-resolution spatially distributed tactile patterns to the skin. Electrotactile stimulation uses skin-interfaced electrodes to transmit currents into the skin to set up potential gradients, depolarizing the haptic sensory nerves and exciting action potentials that travel to the central nervous system [93, 259], resulting in perceptual sensations. The stimulation parameters can be chosen to preferentially excite various classes of nerves, and to optimize the quality of the sensations [96, 98]. Some of the advantages of electrotactile stimulation include the greater integration densities and flexibility achievable due to the lack of mechanically moving parts, and lower power draws when compared with equivalent vibro-tactile methods. A further discussion of different haptic feedback methods and their relative mertits is provided in section 2.4.1 of the dissertation.

Although there have been several proposed wearable haptic displays utilizing arrays of electrotactile stimulation electrodes for haptic actuation at the fingers [260, 261] and forearms [262, 263, 264, 265, 146], these approaches are limited in their scalability. In other words, it is a challenge to greatly increase the number of addressable electrodes of such approaches, as would be required to stimulate large areas of skin with high resolution. The capability to provide currents to multiple skin locations simultaneously also remains a challenge. These issues primarily arise from the multiplexing mechanism which is used to electronically control

the electrode to which the low intensity currents are directed. The complexity of this control method scales with the number of addressable electrodes within the display. Further, multiplexing requires a large number of control line traces to be routed through the substrate, which remains a challenging problem for flexible electronics even with state-of-the-art manufacturing methods. Simple multiplexing methods also only select a single electrode at a time, and significant overhead and complexity is required for each additional simultaneously addressable electrode.

To combat these issues and develop a highly scalable device architecture, we sought to design a new topology and control method. The key insight enabling the effective realization of this display in the present work is that a modular construction with an appropriately designed control mechanism would only require a small number of connections to an external current source, and therefore a constant complexity irrespective of the total number of electrodes in the system. Such a modular device can also provide currents to any number of electrodes simultaneously. For the design of the control method, we were inspired by ideas from the sensory substitution literature [266], namely, approaches to "see" light with our skin. Instead of programming the stimulation location with electrical signals, we utilize optical sensing components within each modular element which independently gate the delivery of current. Current regulating components are used to limit the peak currents delivered to each module and its corresponding electrode. The programming of the array is therefore achieved with applied light fields, which generates tactile patterns over the applied regions of skin.

6.2   Design

We present the design of an optically programmable skin-interfaced device that is capable of simultaneously delivering electrotactile stimulation over wide areas of the skin. The device is implemented using an external driving circuit which provides pulsed voltage signals to a

wearable interface which consists of a modular array of tactile pixels ("taxels"). The taxels, in the presence of incident light, applies the pulsed signals to the skin through means of skin interfaced electrodes.

6.2.1   Electrical design of taxels

The skin-worn interface consists of a distributed array of taxels which individually detect the presence of incident light on them and excite the contacted region of skin with electrotactile stimulation. We designed each sub-unit (taxel) of our array to be functionally independent, with the capability to deliver currents through multiple taxels at arbitrary locations simultaneously. As a consequence, programmed optical patterns presented on the array can result in corresponding haptic sensations.

The design objectives for the taxel element were to optimize the layout size, energy efficiency, comfort and safety, while allowing for the specification of the light sensitivity. The designed electrical circuit of the taxel (Fig. 6.2A) was optimized through the use of SPICE circuit simulations.

The taxel consists of a phototransistor (PT; TEMT6200FX01, Vishay Intertechnology Inc, Malvern, PA) that detects the presence of incident light and outputs a photocurrent. This current sets up a voltage across a bias resistor connected between the base-emitter junction of a high-voltage transistor, controlling the free current flow through the collector-emitter junction. This combination of the phototransistor and transistor functions as a light controlled switch. To minimize the amount of latent power draw of the system, we used a high voltage PNP transistor (HT; CMPTA94, Central Semiconductor Corp., Hauppauge, NY) in our design. This circuit only draws current when light is shined upon the taxel, and is completely off otherwise. A high voltage line is connected to the emitter of the transistor, and the skin-interfaced electrode is connected to the collector. Therefore, the presence of light of high illuminance impinging

on the phototransistor connects the high voltage line through to the skin resistance, causing the injection of sub-dermal currents.

A monophasic pulsed signal (200 V nominal amplitude, 200 μs pulse width, 50 Hz frequency) is provided to the high voltage line by means of an external driving circuit (described below). The pulse width was specified during pre-testing, and 200 μs widths were previously reported to generate electrotactile sensations [93, 267]. The taxel is designed to deliver positive currents into the skin (anodic stimulation), which had previously been reported to preferentially stimulate the rapidly adapting nerves and Meissner corpuscle mechanoreceptors [268]. This influenced our choice to target the Meissners specifically with the 50 Hz repetition frequency. We use a voltage source connected differentially between the high voltage line and the phototransistor to power the phototransistor within its specified operating voltage. Each electrical component was chosen to be the smallest commercially available surface mount device (SMD) which met our required specifications.

The resistance of the bias resistor R (27 kΩ) was empirically chosen to ensure that the transistor turns on with the photocurrent generated at 1000 lux of incident white light. This light level was chosen to be well above typical ambient levels measured in well lit indoor environments (600-800 lx) as measured by a commercial light meter, thus preventing stimulation of the skin unless specifically excited by an external light source. The optical sensitivity of the device can be easily manipulated by changing the value of the bias resistor. Reducing R will decrease the optical sensitivity, requiring higher illuminance levels to turn the device on, and vice versa.

The electrical safety of the device was given paramount consideration to prevent uncomfortable shocks when worn on the skin. During the fabrication process, all circuit traces were coated with 100 μm of insulating material at a minimum, ensuring that only the electrodes are in contact with the skin at any point. As previously discussed, the PNP transistor ensures that the electrode is disconnected from the high voltage line in the absence of light. To

introduce over-current regulation, each taxel also includes a current regulating diode (CRD; S-202T, Semitec USA Corp., Torrance, CA) which limits the current being injected into the skin per taxel to 2 mA. Although the CRD physically occupies a large area (3.5 mm × 1.6 mm, the largest SMD in the circuit) which reduces the integration density of the system, we incorporated it due to the greatly improved safety it provides.

The current limit of the CRD was chosen to exceed the reported sensation thresholds for 200 μs pulses by a factor of two, which is within the commonly reported dynamic range of electrotactile stimulations [93]. This minimizes the possibility of painful sensations, while still ensuring the stimulation can be perceived across multiple locations. As our design allows for multiple taxels to be turned on simultaneously, the per-taxel current regulation also facilitates more constant perceptual sensations throughout the surface of the device, in comparison to a design with current regulation purely at the source. With the aforementioned pulse parameters, a peak energy of 0.16 mJ was delivered per pulse, which is within the limits specified by IEC 601-2-10, the international standard for electrical nerve stimulators [269].

6.2.2   External driving electronics

The pulsed signals used for electrotactile stimulation were generated through a compact external electrical circuit (Fig. 6.2B). A 555 timer IC (LM555N, Harris Corporation, Melbourne, FL) was used to operate an astable multivibrator that generates square waves, with the pulse width and repetition frequency of the signal (200 μs, 50 Hz) controlled by the values of the resistances in the circuit.

This pulsed signal was connected with a sensing resistor to the input of a high voltage (HV) relay (PLA160, IXYS Corporation, Milpitas, CA). A voltage controlled HV source (Trek 2210, Advanced Energy Inc., Denver, CO) was connected to the supply voltage pin of the relay, and the electrotactile array was connected as the load. The pulsed input signals served to close the
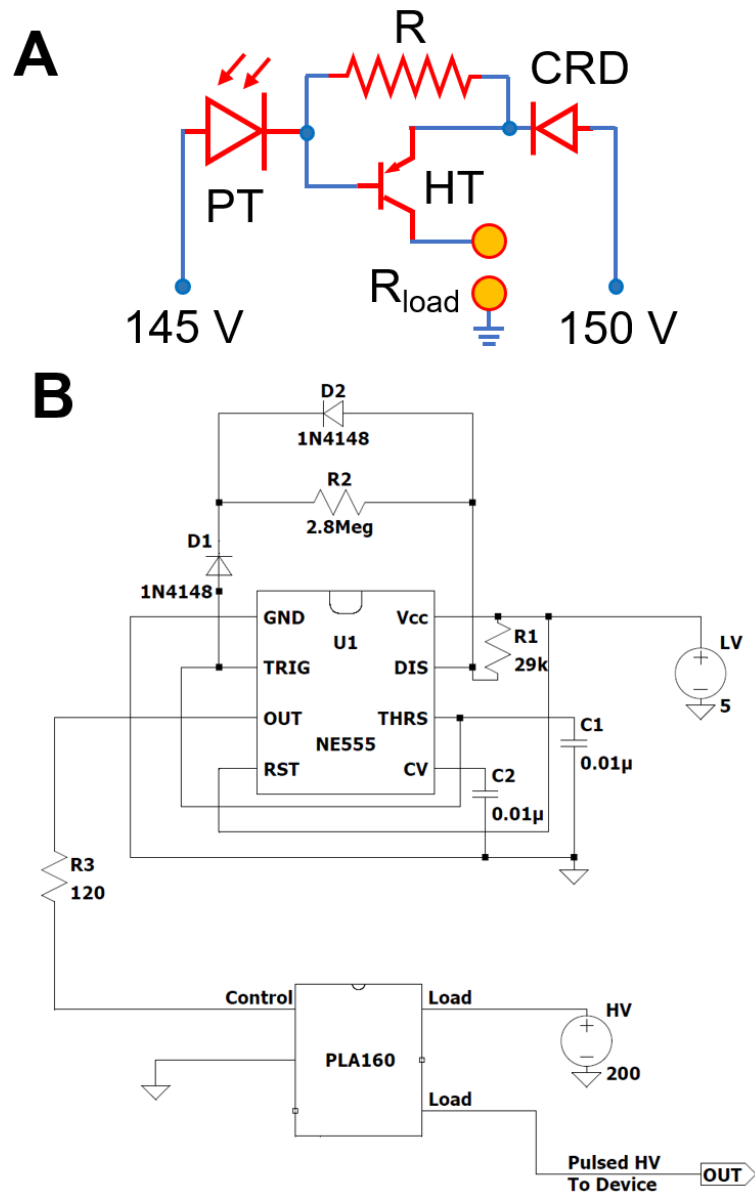
Figure 6.2: Designed electrical circuits. A) Circuit diagram of a taxel. The presence of light beyond a certain threshold value causes the photocurrent to turn the high voltage transistor (HT) on, delivering voltage pulses to the load resistance. A current regulating diode (CRD) limits the peak currents delivered to the load. B) Compact driving circuit employed to generate pulsed high voltage signals delivered to the skin-interfaced opto-electrotactile device. A pulse generator controls the operation of a relay which connects the high voltage source to the load.

supply side electrical circuit during the active phase of the signal, thus delivering a pulsed HV

signal to the load. The value of the sensing resistor was chosen to optimize the rise and fall

times of the pulsed high voltage signal. The electrical components of the driving circuit were powered through a 6 V battery. A second 5 V battery is used to provide the differential voltage to power the phototransistor. In total, there are only two wires which connect the device to the driving electronics (high voltage, differential voltage lines), independent of the number of taxels in the array.

The average power consumption of the driving electronics was calculated to be under 0.1 W. For each taxel actively delivering currents to the skin, we estimate an average power draw of 8 mW for a representative skin resistance of 200 kΩ, making this an extremely efficient method of haptic actuation.

6.2.3   Electrode design

It is a challenging mechanical problem to design electrodes for wearable devices that maintain consistent electrical contact with the skin, particularly as the act of wearing the device may require the substrate to be bent to varying degrees. One prior approach has utilized microsprings to push the electrode towards the skin [261].

To address this challenge, we integrated conductive, spherical, beads as the active electrodes. This raises the profile of the electrodes above the rest of the device. The soft substrate surrounding the beads acts as an elastic membrane, with the restoring force ensuring that the electrode provides consistent and firm contact with the skin. For the fabricated device, we used spherical (3 mm diameter) beads. On the surface of the skin, we found that this typically resulted in a circular contact patch with a diameter of 2 mm. In preliminary testing, we found that using electrodes with smaller contact patches resulted in painful sensations due to the larger current densities, which guided the design choice of using wide, spherical beads.

The active electrodes (with one electrode per taxel) are positioned in an array, with the layout determined by the desired application location on the skin. We were able to achieve

integration densities as dense as 1 taxel/cm^2 using our fabrication method discussed below. For desired applications on the finger, we could configure this as either a 14×1 or a 7×2 array.

To provide a return path for the currents injected into the skin, we used two 3 mm wide rectangular strips of electrically conductive tape (Tape 9712, 3M, Saint Paul, MN) as the ground electrodes. The tape was cut to the length of the array, and placed on the skin 4 mm away from the nearest electrode, and flanking both long ends of the array. The use of conductive tape enabled the placement of a physically large ground electrode near all the taxels, in a manner analogous to prior research [265], while still allowing for the kinematic movement of the joints of the hands and fingers. Using an external component for the current return path also allowed us to increase the integration density of the electrotactile device.

During the design of electrotactile stimulation systems, referred sensations have previously been reported in some cases, where it is thought that currents penetrate to deeper nerve bundles, resulting in sensations over a wider, or more distant area [270, 271, 272]. In preliminary testing, we observed that the proposed electrode configuration drastically limited the occurrence of referred sensations, as compared to other layouts which we considered.

The design of the electrode layout was further guided by numerical simulations as described below.

6.2.4   Numerical modelling of in-vivo currents

Electrotactile stimulation is usually understood to arise from currents from skin-interfaced electrodes propagating into epidermal regions to directly stimulate the nerve interfaces of the mechanoreceptors, which the brain interprets as mechanical sensations (Fig. 6.3A) [95, 97]. The perceived intensity of sensations has previously reported to be strongly correlated with the current density [273, 274], and thus we decided to investigate the current densities within the skin for our electrode configuration, particularly at the typical depths of mechanoreceptors

[275], by using a simplified electrical model.

We used COMSOL Multiphysics (COMSOL AB, Stockholm, Sweden) to perform three dimensional finite element analysis simulations to examine the steady state electrical currents. The skin was modelled as a two layer plate with surface dimensions $2\,\text{cm} \times 8\,\text{cm}$. The topmost layer was chosen to model the stratum corneum, the outermost layer of the epidermis of the skin, which is the most electrically resistive. The second layer was chosen to model viable skin which consists of the remainder of the epidermis and the dermis. The thickness and electrical conductivity of each layer were selected to be the representative values reported in literature [276, 277] (parameters are listed in Table. 6.1). The properties of each medium were set to be uniform within its dimensions. The effective skin resistances computed by the model are slightly larger (300 kΩ) than prior empirical measurements of resistance of the glabrous skin of finger by a factor of 1.5. We hypothesize that this difference is due the existence of sweat glands and skin hydration, which reduce the effective resistance in-vivo on electrical stimulation, the effects of which are not fully captured by our simulated model. Nevertheless, the model enabled us to better understand the effects of modifying the electrode configuration on the current density within the skin.

Skin layer	Thickness (mm)	Electrical Resistivity (Ω.m)	Relative Permittivity (ϵ_r)
Stratum Corneum	0.02	8×10^4	10^4
Viable skin	1.2	4.6	10^6

Table 6.1: Parameters used in the numerical model of electrical currents in the skin

Circular gold electrodes of diameter 2 mm were positioned in a 3×2 array, with the columns separated by a center-to-center spacing of 4 mm, and adjacent rows separated by 1 cm, and electrical contact was established with the skin. Two rectangular, 3 mm wide ground electrodes extend throughout the length of the skin, and placed 4 mm away from the array on either side. A constant current of 2 mA was injected into each of the active electrodes, and we measured the current densities at all points of the skin model.
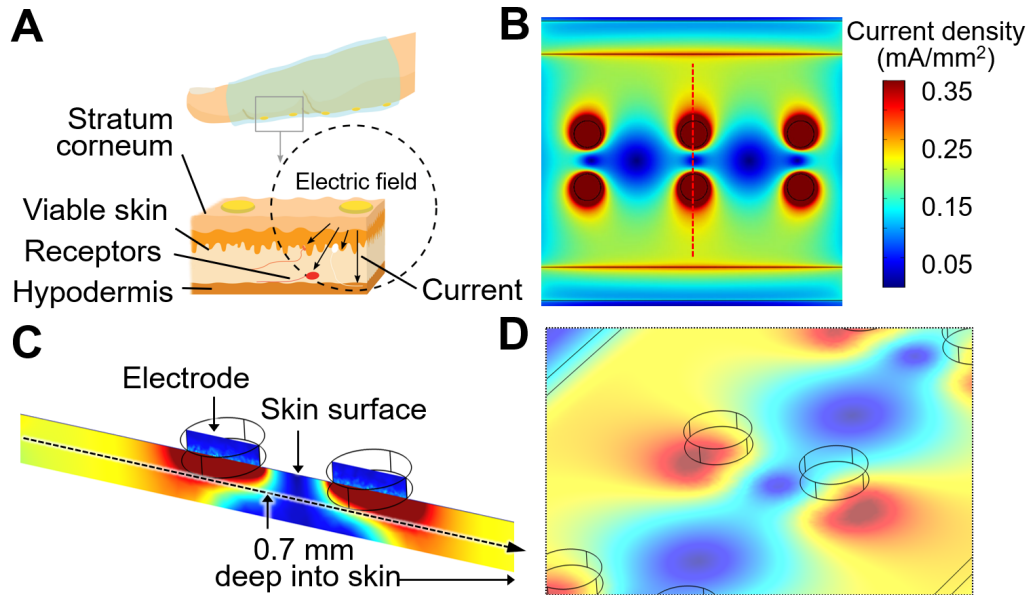
Figure 6.3: Results of numerical modeling of the in-vivo currents with the proposed tactile array. A) Schematic diagram of operation. The voltage applied to the skin results in currents penetrating through to the dermis of the skin, where they stimulate the afferent nerves of the tactile system, resulting in sensations. B) Results of a finite element simulation of the skin with six activated electrodes, showing current density at a plane 20 μm below the surface of the skin. C) Cross-sectional view of the current density. Peak densities occur directly underneath the electrodes. D) Enlarged view of the current density 700 μm into the skin, the depth at which a relevant class of tactile mechanoreceptors are located. The asymmetric electrode layout, with the physically larger area of ground electrodes, ensures that sensations are perceived close to the locations of the electrodes.

When all six electrodes are active, the current density at a plane 20 μm into the surface of the skin highlights some interesting findings (Fig. 6.3B). The asymmetrical layout of the active and ground electrodes (with physically larger grounds) ensures that peak current densities occur primarily near the active electrodes, with the densities at the ground being less pronounced. Further, densities are far more diffuse in the dermal regions between the active and ground electrodes. Studying the cross sectional view across two electrodes and the skin, shows how peak densities (of 0.35 mA/mm^2) occur almost directly under the active electrodes (Fig. 6.3C). This is the case even at plane 700 μm into the skin, the typical depth at which

145

the Meissner corpuscles are located (Fig. 6.3D). These results suggest that with this designed electrode layout, users of the device can localize sensations directly underneath an active electrode, enabling the development of dense, high resolution spatial grids by scaling the number and density of taxels.

6.3   Fabrication

The optoelectronic skin was envisioned to be worn on the skin, in a manner that can be programmed remotely using optical methods. However, such a wearable device requires the electrodes to make direct contact with the body, while the phototransistors must be capable of receiving optical signals from an external source. This requires components to face opposite directions, while being electrically connected on the same plane. Further, these circuits need to be physically stretchable, and embedded within a flexible and soft substrate, to allow for the the device to conform to the skin.

A primary challenge in the development of highly integrated electronics within soft materials is the less mature manufacturing process. To provide an example, polydimethylsiloxane (PDMS) is one of the most commonly used polymers in stretchable devices. However, this material is not compatible with micro-fabrication techniques such as thin-film deposition or high-resolution lithography due to thermal expansion that results in cracks within the substrate. Further, the assembly of SMDs using pick-and-place tools is highly challenging on soft substrates. We overcome these challenges by engineering a hybrid manufacturing method utilizing a heterogeneous integration of materials.

We use lithography methods to deposit circuit traces (Au; 10 μm thick) with inherent strain management features [278, 279] onto a rigid carrier, which consists of a Si wafer with a thin coating of polymethyl methacrylate (PMMA) and poly-imide (PI). We then assemble all the active and passive electrical components onto the circuit by using solder-based interconnects

and standard pick-and-place techniques. A relatively thick substrate layer ($\approx$1 mm) of silicone polymer is coated onto the carrier, and once it has cured, is peeled off from the Si wafer at the sacrificial PI layer. The remaining PI is then removed through dry etching. The electrical components remain embedded within the silicone, and the back of the circuit is now exposed, which allows for more electrical components to be assembled. Here, we solder spherical (3 mm diameter) gold-coated beads onto the electrode contacts, and wires to connect to the external driving circuit. We finally encapsulate the back surface with a 100 μm thin silicone layer, which provides insulation from the circuit traces (Fig. 6.4 A,C,D), and additional mechanical stability to the spherical electrodes.

A key feature of this hybrid manufacturing method is the introduction of the stretchable substrate material at the end of the processing sequence, leveraging the full benefits of microfabrication techniques on a rigid carrier. The process is compatible with a wide range of moldable elastomers. For our fabricated device, we used a silicone polymer which is soft, stretchable, and transparent (Sylgard 182, Dow Corning) (Fig. 6.4B).

We designed the device to be wearable with high conformity, which is essential for seamless and uninterrupted electrical contact with the body during active movement of the hand. However, the conformity of wearable devices largely depends on its thickness and flexibility. On the other hand, these parameters modify the mechanical stability of the device, which influences its ability to be used in a repeatable and consistent manner. The SMD components of the circuit also contribute to the overall thickness of the device. Based on these considerations and several design iterations, we selected a thickness of our current prototypes within the range of 1.2 mm to 1.5 mm (Fig. 6.4C Inset). We fabricated arrays with two different configurations, each with 14 taxels within a 8×2.5 cm area (Fig. 6.4B), and with minimum center-to-center spacing between electrodes being as low as 4 mm apart. Each fabricated array weighed 7.4 g. Fig. 6.4E shows a photograph of devices with different layouts applied on the fingers. While the finger has a small radius of curvature ($\approx$ 2 cm), making it a challenging region for the
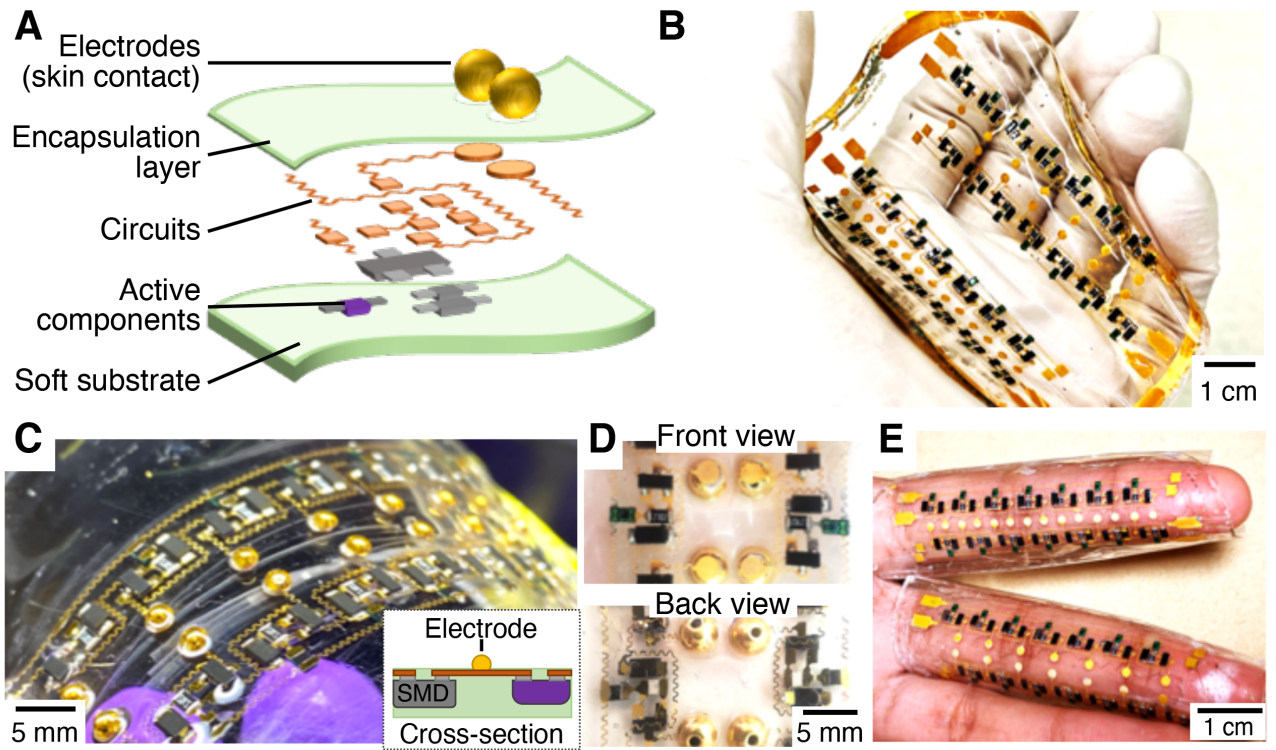
Figure 6.4:   Design and fabrication of the stretchable opto-electrotactile skin. A) Circuit traces and active electronic components are embedded within layers of a soft, stretchable substrate (PDMS). Three dimensional electrodes (spheres) extend through the encapsulation to make contact with the skin. B) The device partially through the fabrication process, showcasing the assembled electronic components, and two grid layouts which we considered. C) Assembled device, Inset figure showcases the cross-section. D) Front and back views of one functional unit ('taxel') of the device. E) Images showing the opto-electronic skins conforming to and contacting the finger.

placement of stretchable devices, our mm-thin optoelectronic skin uniformly conforms to it. In preliminary testing, we identified that the 7×2 array functions better for most haptic applications, likely in part due to the additional resolution along the width of the finger.

6.4   Characterization

To verify the functionality of the taxels, namely that controlling illuminance provides control over the delivered current and thus the stimulus intensity, we first performed electrical

characterization with a fixed load resistance. We then followed it up with in-vivo measure-

ments to study variations in skin resistance at different locations, so as to identify ways to

optimize the device for haptic applications.

6.4.1   Opto-Electrical Characterization

To verify that controlling the illuminance modifies the current delivered to the load resis-

tance in a controllable manner, we placed the array in a dark enclosure (measured illuminance

< 20 lx) at a fixed distance of 10 cm from controllable light source array consisting of white

LEDs. A commercial light meter placed at an identical distance was used to measure the inci-

dent illuminance level for each light step. A 100 kΩ load resistor R_{load} was soldered between

the active electrode of one taxel and the ground, and the voltage signal $v(t)$ across the load was

measured through a digital oscilloscope for each light level. The value of the load was chosen

be within the previously reported ranges of bio-impedance at the fingertip for analogous pulsed

inputs (30 - 200 kΩ) [280, 281, 282]. We measured the current pulses generated at different

illuminance levels, and different source voltages.
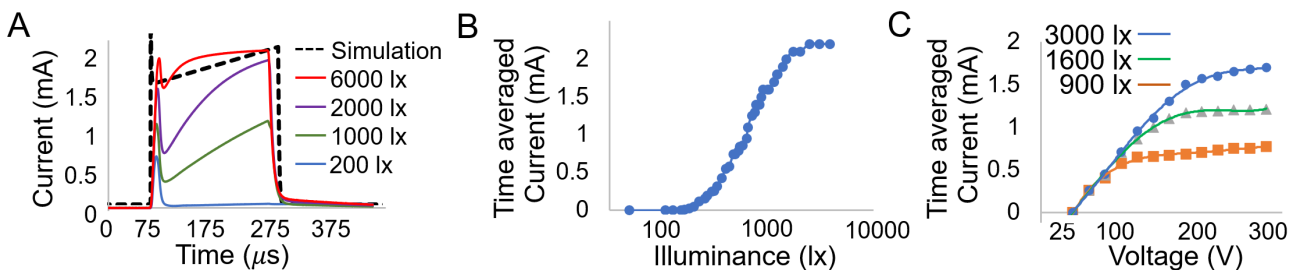
Figure 6.5:   Results of the characterization of a taxel with a fixed 100 kΩ load resistor. A) Time resolved current through the load, for different illuminance values. Beyond 1000 lx, currents exceed levels reported to cause perceptual sensations (1 mA). At large light intensities, the empirical measurements are in good agreement with the simulation results. B) The time averaged current as a function of illuminance follows a logistic function between 0 and 2.2 mA, with it exceeding 1 mA at 1200 lx, a level that is above typical indoor lighting. C) The time averaged current as a function of input voltage, for various illuminance levels. The input voltage can be a useful control parameter to modify the intensity of sensations at a given illuminance level.

A representative measurement of a single current pulse $i_p(t)$ delivered to the load at various light levels is shown in Fig. 6.5A. We computed and plotted a summary metric, the time averaged current $\bar{i}$ delivered to the load by integrating the area under the curve per pulse, for various light levels (Fig. 6.5B). The pulse width T_p was specified to be 200 μs. For square pulses, the total electrical energy delivered per pulse can be easily computed from this metric, $E_{elec} = \bar{i}^2 R_{load} T_p$.

$$\bar{i} = \frac{\int i_p(t)dt}{T_p}$$

The results show that the delivered current $\bar{i}$ increases monotonically with the illuminance E_l, and can be modelled as a log-sigmoid function $\bar{i} = \log(1/(0.126 + exp(-0.0012 * E_l)))$, with an excellent fit ($R^2 = .991$). The taxel is fully off below 160 lx of incident illumination. Small amounts of current ($< .8$ mA) are delivered to the skin for light levels between 200 and 1000 lx. These levels of current are below the previously reported sensation thresholds of electrotactile stimulation for 200 μs pulses [93]. For a 100 kΩ load, the taxel delivers 1 mA of current at 1200 lx, which consistently triggers electrotactile sensations. The time averaged current levels off at 2.1 mA at an illumination level of 6000 lx, with further light intensities not increasing the current. These results show that the circuit only allows peak currents of 2 mA, ensuring safe operation. In subsequent testing, we also measured currents of 2 mA from four taxels at the same time, showcasing the simultaneous operation capabilities of the device. When attempting to drive a larger number of taxels, we hit upon the internal current limiter of our high voltage source.

For any given illumination level, the time averaged current also varies monotonically with the source voltage, before levelling off. (Fig. 6.5C). Therefore, in addition to the intensity of incident light, modification of the source voltage can serve as another method to control the intensity of electrotactile stimulation. This is important since in practical applications, the load resistance R_{load} of the skin can vary significantly from person to person, or potentially

even with changes in contact conditions [273]. In these cases, adjusting the source voltage can serve as a convenient way to modulate the delivered currents across the entire array, without necessitating a modification of the optical signals used for programming the device.

6.4.2   In-vivo characterization

The resistance of human skin varies over its surface, and depends on its local thickness, geometry and the skin humidity, among others variables [280, 283, 284]. Although, the palm and the fingers are tremendously important for tactile sensation, the spatial variation of in-vivo skin resistances at those locations is not comprehensively understood, with prior work generally focusing on a single location such as the fingertip. As our device was designed to be patterned over large areas of the skin, and applies a fixed voltage to the skin across all taxel locations, the currents, and therefore the intensity of sensations, depends on the local skin resistance. Therefore, it was critical to study the in-vivo skin resistance at various locations of interest on the hand. To evaluate this, we measured in-vivo currents at varied stimulation locations of the hand and the fingers of a single participant (the author S.B.) using our device.

The in-vivo current was estimated by measuring the voltage drop across a 2 kΩ shunt resistor connected in series at the high voltage source. We measured the current at 9 distinct locations of interest on the hand (Fig. 6.6A). Namely, these are numbered as follows - 1 - tip of the index finger (digit 2); 2 - 4 - centers of the distal, intermediate and proximal phalanx of the palmar surface of the index finger ; 5 - base of the middle finger (digit 3) on the palm; 6 - thenar eminence on the palm; 7 - center of the wrist on the palmar surface; 8 - center of the intermediate phalanx of digit 2 on the dorsal surface; 9 - base of digit 3 on the dorsal surface. For each location, we fixed the illuminance level at 3000 lx, and measured the time resolved currents, with the source voltage level varied in steps of 20 V from 20 V to 300 V. An estimate of skin resistance was computed by dividing the provided source voltage by the time

averaged current. For each measurement, the participant was also asked whether the sensation was perceivable, and whether it was uncomfortable or painful.
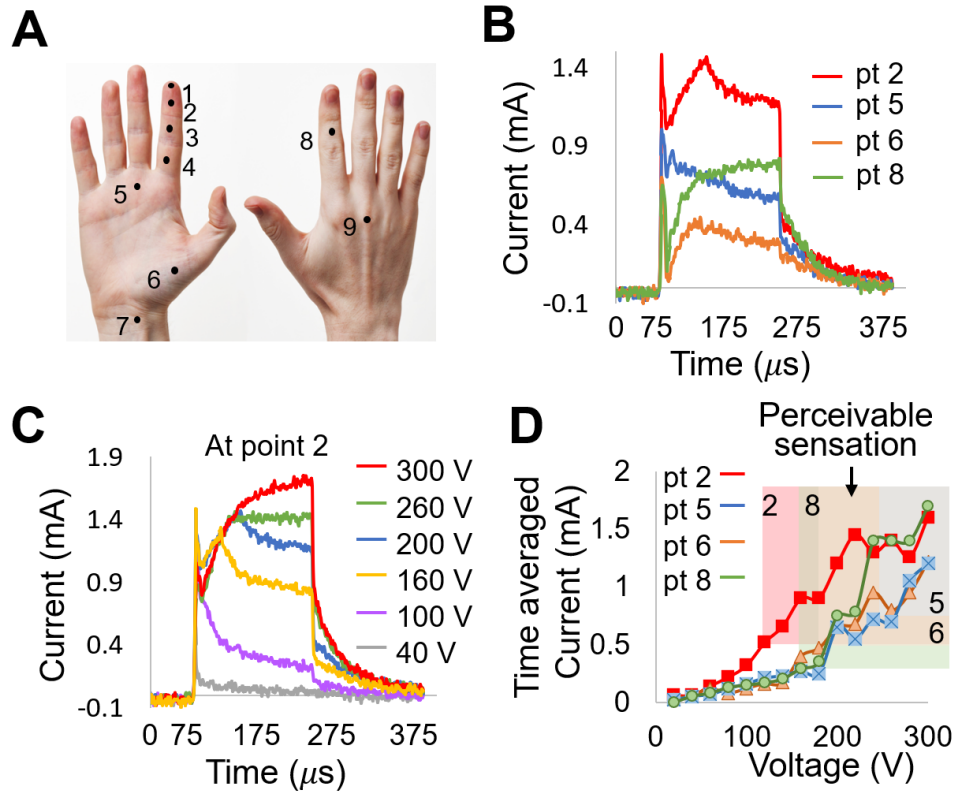
Figure 6.6: An examination of the in-vivo performance of the device. A) The numbered locations of the skin at which in-vivo current measurements where taken. We attempted to obtain data from a wide range of positions along the finger, the palm, wrist, and the dorsal surface of the hand. B) Time resolved currents at various locations on the skin, for a fixed illuminance level (3000 lx) and input voltage (200 V). Results indicate that there is variability within the resistance of the skin at various locations. C) Time resolved current at a single location (Pt 2), for various input voltage levels. Currents increase to perceptual levels above 160 V. D) Variation of the time averaged current as a function of the voltage, for varying stimulation locations. Shaded areas denote the levels of in-vivo current and input voltage required for the sensations to be perceivable. As all taxels of the array are driven with a single voltage level, the driving voltage can be adjusted based on the positioning of the array to ensure that all taxels are perceivable, without being uncomfortably intense.

For a fixed source voltage level, the skin resistance varied dramatically across locations, which could be identified from the time-resolved measurements (Fig. 6.6B). For example, at 200 V, we measured resistances as high as 1.5 MΩ at the tip of the index finger. On the other

hand, at locations along the segments of the finger (location 2 - 4), resistances were similar, varying between 180 - 240 kΩ, with the lowest resistances at the distal segment. Resistances at the other locations were typically measured at 300 - 400 kΩ. The results indicate that for a whole-hand array, the perceived intensity might vary based on the location, if additional optical control of the intensity is not employed.

We observed that at any specific location, the current increased super-linearly with source voltage, indicating that the skin resistance drops at larger voltage levels, echoing prior findings [285]. For example, at the center of the distal segment of the finger (location 2), computed skin resistances of 430 kΩ were measured at 60 V, but this reduced to 280 kΩ at 120 V, and 170 kΩ at 200 V (Fig. 6.6C).

As all taxels in the array are controlled with the same source voltage, the minimum level required to obtain sensations through the entirety of the hand can be identified through studying the voltage and current required to obtain perceivable sensations (Fig. 6.6D) at various locations. The results also suggest that the variation of current with source voltage is generally not monotonic. We hypothesize that this occurred due to temporal variations in skin resistance arising from sweat and skin motion [286].

Measured time-averaged currents across all locations were never larger than 1.7 mA. At the palmar locations, the participant reported perceived sensations for in-vivo currents beyond 0.7 mA, and that it felt uncomfortable when currents exceeded 1.5 mA. However, on the dorsal surface, the corresponding sensation and pain thresholds were lower, at 0.3 and 1 mA respectively. These results suggest that electrotactile devices intended to be used primarily on hairy skin should be modified with reduced optical sensitivity, alongside more conservative current limits. The variation in sensation and pain thresholds for different locations also indicates that delivering identical currents across all the taxels of the distributed whole-hand electrotactile array by modifying the circuit to be current-controlled (in contrast to the voltage control with current limiters as implemented) would not resolve the issue of differing perceived intensi-

ties across locations. Rather, for future work, we propose using optical control to modify the intensities at each taxel location, following a calibration step.

6.5   Discussion and conclusion

In this work, we present a new type of conformable and scalable haptic display that provides electrotactile sensations to the skin with a high spatial resolution. Unlike conventional methods to realize electrotactile arrays, our designed device utilizes a number of repeating, self contained functional sub-assemblies, allowing for safe, simultaneous activation at multiple locations. We constructed the array to be optically programmable, enabling the skin to "see", with control of haptic sensations achieved with simple, off-the-shelf hardware such as projectors displaying optical patterns. The fabricated device was designed to be applied to the fingers, and was manufactured on a stretchable substrate, allowing for it to freely conform to the skin. The layout of the electrodes was guided in part by numerical simulations of electrical current densities in skin. Through opto-electrical and in-vivo characterization, we verified that the device works as intended, delivering perceivable sensations in the presence of incident light beyond a specified threshold. Finally, we examined the spatial variability of skin resistances, to further guide the design of future versions of whole-hand opto-electrotactile arrays. This device design shows promise for achieving efficient, high resolution stimulation of the skin. Further, the light-weight and flexible nature of the device allows for it to be applied to the hands and fingers while preserving their natural range of motion, and the controllable reproduction of tactile patterns makes it particularly suitable for applications such as virtual object detection in augmented reality.

The in-vivo characterization, while extremely informative, was limited by its sample size. A more rigorous study with more participants can be considered to better identify spatial variations in electrotactile sensations over populations.

In future work, we aim to perform a comprehensive evaluation of the fabricated device for haptic applications, exploring the construction of programmable light field patterns that result in effective wide-area haptic sensations. In future iterations, we also intend to miniaturize the driving electronics, and eliminate the need for a desk-top voltage supply by utilizing DC-DC converters that can generate high voltage, low current signals from batteries, enabling a fully portable and wearable device.

Chapter 7

Conclusion

This PhD research was motivated by the engineering challenges of developing efficient technologies, including compact, wearable devices, for stimulating the sense of touch in manners that are analogous to what can be achieved via commodity visual and audio displays. This has been a goal that is still far out of reach even after decades of research. There are several reasons for this, such as the distributed nature of human touch sensation and perception, the complex physical phenomena involved in touch sensing, and the multiple haptic sub-modalities involved, aspects of which are still not fully understood today.

Haptics is a highly multi-disciplinary domain, integrating research on varied topics of physiology, biomechanics, perception, and engineering. In a similar vein, this dissertation contributes to the knowledge in several different areas in an attempt to serve longstanding goals, by presenting studies addressing proprioceptive sensing and the influence of visual information; presenting studies evaluating the mechanical basis of touch that inform new efficient rendering methods for spatiotemporal stimulation; and informed by these, presenting the design and engineering of new wearable haptic actuators and displays.

One aspect of the haptics research conducted during this PhD was motivated by the active, integrative nature of perception, which encompasses the body's capacities for both touch

sensing and for perceiving the position and movements of the body. While prior research has elucidated human abilities of perceiving the spatial location of the limb, less is known about our ability to perceive the complex spatial configurations of the fingers of the hand during different hand poses or manual grasps. Such questions are particularly relevant for emerging virtual reality technologies, in which electronic sensing, in tandem with visual or haptic displays, are used to provide embodied experiences of interacting manually within virtual environments. Chapter 3 presents the first direct investigation of human abilities of proprioceptively localizing multiple fingers of the hand via haptics or multimodally, using both haptic and visual cues. The results highlighted a surprising finding - the localization errors were large relative to the size of the hand, of the order of several centimeters, unless visual cues of adjacent finger positions were provided. Further, the observed errors were finger-dependent, with the localization of the thumb and index finger the most accurate, suggesting how human capabilities have adapted to better support the tasks which these fingers perform. These results prove informative for haptic applications that rely on the sensing of finger positions.

The development of efficient ways to stimulate the skin has been a great challenge in haptic engineering research. Recent research findings elucidate how the biomechanics of the skin greatly contributes to haptic sensation and perception, but such effects have scarcely been investigated for their potential to facilitate the design of haptic devices. Chapter 4 presents new research including studies of the physical transmission of mechanical stimuli delivered to the skin, including the propensity of the latter to excite spatially propagating mechanical signals traveling large distances along the skin. This research highlighted for the first time the important role played by frequency dependent damping of propagating mechanical waves in the skin. I utilized these findings to develop a method, described here for the first time, that can, with as few as one single actuator, elicit dynamic, spatially varying haptic sensations moving across the skin. This research shows how physically-informed feedback methods can efficiently generate immersive, spatiotemporal haptic feedback for interactions within virtual

reality. These results show how even a single actuator can be used to generate evocative, spatial haptic effects, and suggests how haptic designers can use these methods to achieve extensive control of spatial sensations on the hand by using a small number of actuators.

Motivated by the dearth of compact actuators that can reproduce complex haptic stimuli such as those proposed in the preceding chapter, and the new opportunities revealed in that research, Chapter 5 presents the engineering design and characterization of a compact, wearable actuator that can deliver high fidelity haptic sensations. This device is built to effectively stimulate with skin over a wide range of frequencies, as well as to provide constant and transient forces. This actuator operates based on the interaction forces between a coil with currents flowing through it, and a suspended permanent magnet. A ferrofluid was incorporated within the cavities of the actuator to improve the magnetic and thermal performance, as well as to introduce damping to the system and control for the mechanical resonance that typically affects such electromagnetic actuators. The constructed actuator exceeds the comprehensive performance achievable from current state-of-the-art compact haptic actuators and can render rich sensations such as those described in Chapter 4. It therefore shows great promise for implementations in wearable and handheld devices.

Finally, motivated by the challenges of stimulating the skin with high spatial resolution in a programmable fashion, Chapter 6 presents work on the design of a new haptic display that can provide tactile patterns to wide areas of the skin in an optically programmable manner, thus allowing the skin to "see". By utilizing recent improvements in the field of flexible electronics, the display is implemented as an arbitrarily scalable array of electrical components and electrodes, fabricated on a stretchable substrate that can be patterned onto the skin. The application of directed light beams to an array element delivers low-intensity currents into the sub-dermal regions of the skin in a controlled manner, which stimulates sensory nerves to generate tactile sensations. The findings of this chapter also describe physiological considerations that can guide the design of technologies based on this novel haptic display technique. This

proposed method is highly scalable and allows for the optically controlled delivery of localized haptic sensations across large surface areas with high resolution, and with small amounts of power used. The design makes it particularly attractive for use in conformable haptic devices for augmented reality that can allow for the identification of the three-dimensional structure of virtual objects.

7.1   Future research directions

This dissertation contributes to the body of knowledge of human perception and biomechanics, and presents effective approaches to obtain high fidelity haptic effects from wearable devices. These methods have a great potential for implementation in haptic technologies for virtual and augmented reality. However, there remain several open questions related to the results of this dissertation which are worth considering, and which need further research to fully address.

Although the results of Chapter 3 provide information on the inherent ability of humans to localize their fingers, the impact of visuo-proprioceptive mismatches arising from errors in electronic sensing of the hand, on the immersion within virtual environments was not directly addressed. Such a question would have to be evaluated with a different experiment, which utilizes the findings of Chapter 3 within its design.

The haptic rendering methods discussed in Chapters 4 present specially designed stimuli that generate spatiotemporal haptic effects of expansion and contraction. More investigation is necessary to identify systematic ways to construct and modify these stimuli to allow a haptic designer to specify the spatial extent and duration of the effect.

While Chapter 6 showcases the design and characterization of a haptic display consisting of an electrotactile array that can be patterned onto the skin, more research is needed to optimize the form factor and evaluate the functionality of the display for haptic applications. Further,

within the current design, all the electrodes, in the presence of light deliver identical voltage signals to the skin, with the currents influenced by local skin resistance. Potential improvements to the design include implementing a closed loop control system to modify the intensity of the controlling optical patterns. Further, the impact of self-occlusion that arises from natural hand motion needs to be considered in the design and positioning of the optical source.

The research also suggests several avenues for future investigation that may contribute to the overarching challenge of developing efficient technologies to stimulate the skin, some of which are being pursued by me and my colleagues.

- The findings from Chapter 4 describe how vibrations applied to the skin propagate to far away distances in a frequency dependent manner. This biomechanical behavior can potentially be used to achieve wave-field focusing at distant locations of the hand, using computational data-driven techniques such as time-reversal focusing and inverse filtering. This could, for example, allow a device on the wrist to generate clearly perceivable haptic sensations localized at arbitrary locations on the palm, while leaving the hand unencumbered for regular interactions. Further research is needed to shape the mechanical waves within the skin, and the associated perceptual sensations.

- The results from Chapter 4 raise interesting questions regarding the perceptual relevance of tactile waves. The mechanoreceptors that detect high-frequency stimuli (Pacinian corpuscles) have been reported in literature to have extremely large receptive fields, which can be explained in part by the biomechanical properties of skin. However, the receptors are distributed at densities that suggest that the brain receives information from several hundred afferent nerves situated over large spatial regions for many contact events and applied vibrations. The extent to which spatial encoding is utilized within neural processing is currently an open question. To investigate this, we are utilizing the full-field vibrometry dataset I collected, in conjunction with a computational toolbox that pre-

dicts the spiking response of the sensory nerves, to better understand the information contained within the population responses. This research shows promise for elucidating more efficient methods to stimulate the skin.

- The rendering methods discussed in Chapters 4 and 5 present the designed stimuli to the fingertip, a region of the hand that is actively used within exploration tasks to touch objects. However, the generality of the underlying physical phenomena suggest that similar methods could be used at other body locations, which we have empirically confirmed through several demonstrations. Therefore, rendering algorithms that utilize the physics of waves in the skin can be developed for use with wearable, multi-actuator configurations.

- The haptic actuator and display proposed in Chapters 5 and 6 stimulate the skin with high temporal and spatial resolutions respectively. However, it remains a challenge to design a single, practical device which can accomplish both these goals. Conceptually, such a device would take the form of a dense array of actuators conforming to the skin, where each actuator can present arbitrary stimuli to the contacted region. However, electromagnetic actuators face significant challenges in miniaturization, and in designing for flexibility; while electrotactile stimulation is often constrained to use short electrical pulses to optimize the comfort of sensations, limiting the variety of haptic effects that can be generated. More research is needed to overcome these limitations or to identify effective new approaches.

The various findings presented in this thesis can be utilized in the development of new, efficient, high-fidelity haptic displays for use in virtual and augmented reality, enabling users to *feel* the virtual objects that they can see, resulting in several new applications being discovered for these nascent but rapidly growing industries. The comprehensive realization of this goal would require further advancements in the understanding of touch perception, the design and

miniaturization of haptic actuators, and construction of effective haptic rendering techniques; which this research contributes towards. The findings can also enhance the immersion and collaborative aspects of virtual workspaces that utilize these devices, thus spurring societal and economic advancement.

Bibliography

[1] A. Zimmerman, L. Bai, and D. D. Ginty, *The gentle touch receptors of mammalian skin*, *Science* **346** (2014), no. 6212 950–954.

[2] F. McGlone, A. B. Vallbo, H. Olausson, L. Loken, and J. Wessberg, *Discriminative touch and emotional touch.*, *Canadian Journal of Experimental Psychology/Revue canadienne de psychologie expérimentale* **61** (2007), no. 3 173.

[3] S. J. Bolanowski, G. A. Gescheider, and R. T. Verrillo, *Hairy skin: psychophysical channels and their physiological substrates*, *Somatosensory & motor research* **11** (1994), no. 3 279–290.

[4] U. Proske and S. C. Gandevia, *The proprioceptive senses: their roles in signaling body shape, body position and movement, and muscle force*, *Physiological reviews* (2012).

[5] A. Israr and I. Poupyrev, *Tactile brush: drawing on skin with a tactile grid display*, in *Proceedings of the SIGCHI Conference on Human Factors in Computing Systems*, pp. 2019–2028, ACM, 2011.

[6] D. Wang, K. Ohnishi, and W. Xu, *Multimodal haptic display for virtual reality: A survey*, *IEEE Transactions on Industrial Electronics* **67** (2019), no. 1 610–623.

[7] G. Corniani and H. P. Saal, *Tactile innervation densities across the whole body*, *Journal of Neurophysiology* **124** (2020), no. 4 1229–1240.

[8] R. S. Johansson, *Sensory input and control of grip*, *Sensory guidance of movement* **218** (1998) 45–63.

[9] F. R. Sarlegna and R. L. Sainburg, *The roles of vision and proprioception in the planning of reaching movements*, *Progress in motor control* (2009) 317–335.

[10] A. M. Kappers and W. M. Bergmann Tiest, *Haptic perception*, *Wiley Interdisciplinary Reviews: Cognitive Science* **4** (2013), no. 4 357–374.

[11] B. Dandu, I. A. Kuling, and Y. Visell, *Proprioceptive localization of the fingers: Coarse, biased, and context-sensitive*, *IEEE Transactions on Haptics* **13** (2020), no. 2 259–269.

[12] B. Dandu, Y. Shao, and Y. Visell, *Rendering spatiotemporal haptic effects via the physics of waves in the skin*, IEEE Transactions on Haptics **14** (2020), no. 2 347–358.

[13] B. Dandu, Y. Shao, A. Stanley, and Y. Visell, *Spatiotemporal haptic effects from a single actuator via spectral control of cutaneous wave propagation*, in *2019 IEEE World Haptics Conference (WHC)*, pp. 425–430, 2019.

[14] B. Hannaford and A. M. Okamura, *Haptics*, in *Springer Handbook of Robotics*, pp. 1063–1084. Springer, 2016.

[15] M. Zyda, *From visual simulation to virtual reality to games*, Computer **38** (2005), no. 9 25–32.

[16] L. Jensen and F. Konradsen, *A review of the use of virtual reality head-mounted displays in education and training*, Education and Information Technologies **23** (2018), no. 4 1515–1529.

[17] J. Wolfartsberger, *Analyzing the potential of virtual reality for engineering design review*, Automation in Construction **104** (2019) 27–37.

[18] R. Palmarini, J. A. Erkoyuncu, R. Roy, and H. Torabmostaedi, *A systematic review of augmented reality applications in maintenance*, Robotics and Computer-Integrated Manufacturing **49** (2018) 215–228.

[19] E. Z. Barsom, M. Graafland, and M. P. Schijven, *Systematic review on the effectiveness of augmented reality applications in medical training*, Surgical endoscopy **30** (2016), no. 10 4174–4183.

[20] G. C. Burdea, *Haptic feedback for virtual reality*, in *Virtual reality and prototyping workshop*, vol. 2, pp. 17–29, Citeseer, 1999.

[21] R. W. Lindeman, Y. Yanagida, H. Noma, and K. Hosaka, *Wearable vibrotactile systems for virtual contact and information display*, Virtual Reality **9** (2006), no. 2 203–213.

[22] L. A. Jones, *Haptics*. MIT Press Essential Knowledge series, 2018.

[23] M. A. Srinivasan, *What is haptics?*, Laboratory for Human and Machine Haptics: The Touch Lab, Massachusetts Institute of Technology (1995) 1–11.

[24] J. J. Gibson, *Observations on active touch.*, Psychological review **69** (1962), no. 6 477.

[25] S. J. Lederman and R. L. Klatzky, *Hand movements: A window into haptic object recognition*, Cognitive psychology **19** (1987), no. 3 342–368.

[26] H. P. Saal and S. J. Bensmaia, *Touch is a team effort: interplay of submodalities in cutaneous sensibility*, Trends in neurosciences **37** (2014), no. 12 689–697.

[27] R. Brasselet, R. S. Johansson, A. Arleo, Y. Bengio, D. Schuurmans, J. Lafferty, C. Williams, and A. Culotta, *Optimal context separation of spiking haptic signals by second-order somatosensory neurons.*, in *NIPS*, pp. 180–188, Citeseer, 2009.

[28] E. L. Mackevicius, M. D. Best, H. P. Saal, and S. J. Bensmaia, *Millisecond precision spike timing shapes tactile perception*, *Journal of Neuroscience* **32** (2012), no. 44 15309–15317.

[29] H. P. Saal, X. Wang, and S. J. Bensmaia, *Importance of spike timing in touch: an analogy with hearing?*, *Current opinion in neurobiology* **40** (2016) 142–149.

[30] R. S. Johansson and I. Birznieks, *First spikes in ensembles of human tactile afferents code complex spatial fingertip events*, *Nature neuroscience* **7** (2004), no. 2 170–177.

[31] J. Phillips, R. Johansson, and K. Johnson, *Representation of braille characters in human nerve fibres*, *Experimental Brain Research* **81** (1990), no. 3 589–592.

[32] K. Johnson, *Reconstruction of population response to a vibratory stimulus in quickly adapting mechanoreceptive afferent fiber population innervating glabrous skin of the monkey.*, *Journal of Neurophysiology* **37** (1974), no. 1 48–72.

[33] M. A. Muniak, S. Ray, S. S. Hsiao, J. F. Dammann, and S. J. Bensmaia, *The neural coding of stimulus intensity: linking the population response of mechanoreceptive afferents with psychophysical behavior*, *Journal of Neuroscience* **27** (2007), no. 43 11687–11699.

[34] T. Callier, A. K. Suresh, and S. J. Bensmaia, *Neural coding of contact events in somatosensory cortex*, *Cerebral Cortex* **29** (2019), no. 11 4613–4627.

[35] M. Liu, A. Batista, S. Bensmaia, and D. J. Weber, *Information about contact force and surface texture is mixed in the firing rates of cutaneous afferent neurons*, *Journal of Neurophysiology* **125** (2021), no. 2 496–508.

[36] A. Vallbo, R. S. Johansson, *et. al.*, *Properties of cutaneous mechanoreceptors in the human hand related to touch sensation*, *Hum Neurobiol* **3** (1984), no. 1 3–14.

[37] R. S. Johansson and J. R. Flanagan, *Coding and use of tactile signals from the fingertips in object manipulation tasks*, *Nature reviews. Neuroscience* **10** (2009), no. 5 345.

[38] J. Bell, S. Bolanowski, and M. H. Holmes, *The structure and function of pacinian corpuscles: a review*, *Progress in neurobiology* **42** (1994), no. 1 79–128.

[39] M. S. Fleming and W. Luo, *The anatomy, function, and development of mammalian aβ low-threshold mechanoreceptors*, *Frontiers in biology* **8** (2013), no. 4 408–420.

[40] L. S. Löken, J. Wessberg, F. McGlone, and H. Olausson, *Coding of pleasant touch by unmyelinated afferents in humans*, *Nature neuroscience* **12** (2009), no. 5 547–548.

[41] A. G. Marshall and F. P. McGlone, *Affective touch: the enigmatic spinal pathway of the c-tactile afferent*, *Neuroscience insights* **15** (2020) 2633105520925072.

[42] J. Lo, R. S. Johansson, *et. al.*, *Regional differences and interindividual variability in sensitivity to vibration in the glabrous skin of the human hand*, *Brain research* **301** (1984), no. 1 65–72.

[43] R. T. Verrillo and S. J. Bolanowski Jr, *The effects of skin temperature on the psychophysical responses to vibration on glabrous and hairy skin*, *The Journal of the Acoustical Society of America* **80** (1986), no. 2 528–532.

[44] G. A. Gescheider, A. Capraro, R. D. Frisina, R. D. Hamer, and R. T. Verrillo, *The effects of a surround on vibrotactile thresholds.*, *Sensory Processes* **2** (1978), no. 2 99–115.

[45] N. D. Strzalkowski, J. J. Triano, C. K. Lam, C. A. Templeton, and L. R. Bent, *Thresholds of skin sensitivity are partially influenced by mechanical properties of the skin on the foot sole*, *Physiological reports* **3** (2015), no. 6 e12425.

[46] M. Stuart, A. B. Turman, J. Shaw, N. Walsh, and V. Nguyen, *Effects of aging on vibration detection thresholds at various body regions*, *BMC geriatrics* **3** (2003), no. 1 1–10.

[47] P. Burgess, J. Y. Wei, F. Clark, and J. Simon, *Signaling of kinesthetic information by peripheral sensory receptors*, *Annual review of neuroscience* **5** (1982), no. 1 171–188.

[48] B. B. Edin, *Quantitative analyses of dynamic strain sensitivity in human skin mechanoreceptors*, *Journal of neurophysiology* **92** (2004), no. 6 3233–3243.

[49] U. B. Rongala, A. Seyfarth, V. Hayward, and H. Jorntell, *The dynamics of touch sensing studied in a mass-spring-damper model of the skin*, *bioRxiv* (2021).

[50] L. R. Manfredi, A. T. Baker, D. O. Elias, J. F. Dammann III, M. C. Zielinski, V. S. Polashock, and S. J. Bensmaia, *The effect of surface wave propagation on neural responses to vibration in primate glabrous skin*, *PLoS One* **7** (2012), no. 2 e31203.

[51] Y. Shao, V. Hayward, and Y. Visell, *Spatial patterns of cutaneous vibration during whole-hand haptic interactions*, *Proceedings of the National Academy of Sciences* **113** (2016), no. 15 4188–4193.

[52] Y. Shao, V. Hayward, and Y. Visell, *Compression of dynamic tactile information in the human hand*, *Science advances* **6** (2020), no. 16 eaaz1158.

[53] X. Libouton, O. Barbier, Y. Berger, L. Plaghki, and J.-L. Thonnard, *Tactile roughness discrimination of the finger pad relies primarily on vibration sensitive afferents not necessarily located in the hand*, *Behavioural brain research* **229** (2012), no. 1 273–279.

[54] J. Andrews, M. Adams, and T. Montenegro-Johnson, *A universal scaling law of mammalian touch*, *Science advances* **6** (2020), no. 41 eabb6912.

[55] K. O. Sofia and L. Jones, *Mechanical and psychophysical studies of surface wave propagation during vibrotactile stimulation*, *IEEE Transactions on Haptics* **6** (2013), no. 3 320–329.

[56] F. H. Silver, J. W. Freeman, and D. DeVore, *Viscoelastic properties of human skin and processed dermis*, *Skin research and technology* **7** (2001), no. 1 18–23.

[57] R. B. Groves, S. A. Coulman, J. C. Birchall, and S. L. Evans, *An anisotropic, hyperelastic model for skin: experimental measurements, finite element modelling and identification of parameters for human and murine skin*, *Journal of the mechanical behavior of biomedical materials* **18** (2013) 167–180.

[58] F. Khatyr, C. Imberdis, P. Vescovo, D. Varchon, and J.-M. Lagarde, *Model of the viscoelastic behaviour of skin in vivo and study of anisotropy*, *Skin research and technology* **10** (2004), no. 2 96–103.

[59] W. F. Larrabee Jr, *A finite element model of skin deformation. i. biomechanics of skin and soft tissue: a review*, *The Laryngoscope* **96** (1986), no. 4 399–405.

[60] J. Z. Wu, K. Krajnak, D. E. Welcome, and R. G. Dong, *Three-dimensional finite element simulations of the dynamic response of a fingertip to vibration*, .

[61] B. Khojasteh, M. Janko, and Y. Visell, *Complexity, rate, and scale in sliding friction dynamics between a finger and textured surface*, *Scientific reports* **8** (2018), no. 1 1–10.

[62] V. Hayward, *Tactile illusions*, in *Scholarpedia of Touch*, pp. 327–342. Springer, 2016.

[63] V. Hayward, *A brief taxonomy of tactile illusions and demonstrations that can be done in a hardware store*, *Brain research bulletin* **75** (2008), no. 6 742–752.

[64] S. J. Lederman and L. A. Jones, *Tactile and haptic illusions*, *IEEE Transactions on Haptics* **4** (2011), no. 4 273–294.

[65] D. Goldreich, *A bayesian perceptual model replicates the cutaneous rabbit and other tactile spatiotemporal illusions*, *PloS one* **2** (2007), no. 3 e333.

[66] D. E. Angelaki, Y. Gu, and G. C. DeAngelis, *Multisensory integration: psychophysics, neurophysiology, and computation*, *Current opinion in neurobiology* **19** (2009), no. 4 452–458.

[67] L. C. van Dam, C. V. Parise, and M. O. Ernst, *10 modeling multisensory integration*, *Sensory integration and the unity of consciousness* (2014) 209.

[68] M. Samad, A. J. Chung, and L. Shams, *Perception of body ownership is driven by bayesian sensory inference*, *PloS one* **10** (2015), no. 2 e0117178.

[69] D. Goldreich and J. Tong, *Prediction, postdiction, and perceptual length contraction: a bayesian low-speed prior captures the cutaneous rabbit and related illusions*, *Frontiers in psychology* **4** (2013) 221.

[70] P. Litwin, *Extending bayesian models of the rubber hand illusion*, *Multisensory research* **33** (2020), no. 2 127–160.

[71] J. R. Flanagan, J. P. Bittner, and R. S. Johansson, *Experience can change distinct size-weight priors engaged in lifting objects and judging their weights*, *Current Biology* **18** (2008), no. 22 1742–1747.

[72] J. H. Kirman, *Tactile apparent movement: The effects of interstimulus onset interval and stimulus duration*, *Perception & Psychophysics* **15** (1974), no. 1 1–6.

[73] G. Von Békésy, *Neural funneling along the skin and between the inner and outer hair cells of the cochlea*, *The Journal of the Acoustical Society of America* **31** (1959), no. 9 1236–1249.

[74] H. Elsayed, M. Weigel, F. Müller, M. Schmitz, K. Marky, S. Günther, J. Riemann, and M. Mühlhäuser, *Vibromap: Understanding the spacing of vibrotactile actuators across the body*, *Proceedings of the ACM on Interactive, Mobile, Wearable and Ubiquitous Technologies* **4** (2020), no. 4 1–16.

[75] F. A. Geldard and C. E. Sherrick, *The cutaneous" rabbit": a perceptual illusion*, *Science* **178** (1972), no. 4057 178–179.

[76] H. Kato, Y. Hashimoto, and H. Kajimoto, *Basic properties of phantom sensation for practical haptic applications*, in *International Conference on Human Haptic Sensing and Touch Enabled Computer Applications*, pp. 271–278, Springer, 2010.

[77] J. Seiler, N. Schäfer, B. Latsch, R. Chadda, M. Hessinger, P. Beckerle, and M. Kupnik, *Wearable vibrotactile interface using phantom tactile sensation for human-robot interaction*, in *International Conference on Human Haptic Sensing and Touch Enabled Computer Applications*, pp. 380–388, Springer, 2020.

[78] G. Park and S. Choi, *Tactile information transmission by 2d stationary phantom sensations*, in *Proceedings of the 2018 CHI Conference on Human Factors in Computing Systems*, pp. 1–12, 2018.

[79] G. Yun, S. Oh, and S. Choi, *Seamless phantom sensation moving across a wide range of body*, in *2019 IEEE World Haptics Conference (WHC)*, pp. 616–621, IEEE, 2019.

[80] J. Kim, S. Oh, C. Park, and S. Choi, *Body-penetrating tactile phantom sensations*, in *Proceedings of the 2020 CHI Conference on Human Factors in Computing Systems*, pp. 1–13, 2020.

[81] S. Tawa, H. Nagano, Y. Tazaki, and Y. Yokokohji, *Extended phantom sensation: vibrotactile-based movement sensation in the area outside the inter-stimulus*, *Advanced Robotics* **35** (2021), no. 5 268–280.

[82] C. Hatzfeld and T. A. Kern, *Engineering haptic devices*. Springer, 2016.

[83] T. H. Massie, J. K. Salisbury, *et. al.*, *The phantom haptic interface: A device for probing virtual objects*, in *Proceedings of the ASME winter annual meeting, symposium on haptic interfaces for virtual environment and teleoperator systems*, vol. 55 (1), pp. 295–300, Chicago, IL, 1994.

[84] "Force dimension: Omega." https://www.forcedimension.com/products. Online; accessed 25-October-2021.

[85] H. Culbertson, S. B. Schorr, and A. M. Okamura, *Haptics: The present and future of artificial touch sensation*, *Annual Review of Control, Robotics, and Autonomous Systems* **1** (2018) 385–409.

[86] S. Choi and K. J. Kuchenbecker, *Vibrotactile display: Perception, technology, and applications*, *Proceedings of the IEEE* **101** (2012), no. 9 2093–2104.

[87] "Engineering acoustics, inc: C2 tactor." https://www.eaiinfo.com/product/c2/. Online; accessed 01-November-2021.

[88] "Tactile labs: Hapcoil-one." http://tactilelabs.com/products/haptics/haptuator-mark-ii-v2/. Online; accessed 01-November-2021.

[89] "Precision microdrives: Linear resonant actuators." https://www.precisionmicrodrives.com/linear-resonant-actuators-lras. Online; accessed 01-November-2021.

[90] "Piezo.com: Piezoelectric actuators." https://piezo.com/collections/piezoelectric-actuators-motors. Online; accessed 01-November-2021.

[91] "Tdk coorporation: Piezohapt actuators." https://product.tdk.com/en/products/sw_piezo/haptic/piezohapt/index.html. Online; accessed 01-November-2021.

[92] R. Butikofer and P. D. Lawrence, *Electrocutaneous nerve stimulation-i: Model and experiment*, *IEEE transactions on biomedical engineering* (1978), no. 6 526–531.

[93] K. A. Kaczmarek, J. G. Webster, P. Bach-y Rita, and W. J. Tompkins, *Electrotactile and vibrotactile displays for sensory substitution systems*, *IEEE transactions on biomedical engineering* **38** (1991), no. 1 1–16.

[94] P. Kourtesis, F. Argelaguet, S. Vizcay, M. Marchal, and C. Pacchierotti, *Electrotactile feedback for hand interactions: A systematic review, meta-analysis, and future directions*, *arXiv preprint arXiv:2105.05343* (2021).

[95] H. Kajimoto, *Electro-tactile display: principle and hardware*, in *Pervasive Haptics*, pp. 79–96. Springer, 2016.

[96] H. Kajimoto, N. Kawakami, T. Maeda, and S. Tachi, *Electro-tactile display with tactile primary color approach*, *Graduate School of Information and Technology, The University of Tokyo* (2004).

[97] V. Yem and H. Kajimoto, *Comparative evaluation of tactile sensation by electrical and mechanical stimulation*, *IEEE transactions on haptics* **10** (2016), no. 1 130–134.

[98] K. A. Kaczmarek, J. G. Webster, and R. G. Radwin, *Maximal dynamic range electrotactile stimulation waveforms*, *IEEE transactions on biomedical engineering* **39** (1992), no. 7 701–715.

[99] Y. H. Jung, J.-H. Kim, and J. A. Rogers, *Skin-integrated vibrohaptic interfaces for virtual and augmented reality*, *Advanced Functional Materials* **31** (2021), no. 39 2008805.

[100] W. Dangxiao, G. Yuan, L. Shiyi, Y. Zhang, X. Weiliang, and X. Jing, *Haptic display for virtual reality: progress and challenges*, *Virtual Reality & Intelligent Hardware* **1** (2019), no. 2 136–162.

[101] C. Wee, K. M. Yap, and W. N. Lim, *Haptic interfaces for virtual reality: Challenges and research directions*, *IEEE Access* **9** (2021) 112145–112162.

[102] J. Yin, R. Hinchet, H. Shea, and C. Majidi, *Wearable soft technologies for haptic sensing and feedback*, *Advanced Functional Materials* **31** (2021), no. 39 2007428.

[103] X. Chen, P. Sun, and D. Liao, *A patient-specific haptic drilling simulator based on virtual reality for dental implant surgery*, *International journal of computer assisted radiology and surgery* **13** (2018), no. 11 1861–1870.

[104] E. M. Overtoom, T. Horeman, F.-W. Jansen, J. Dankelman, and H. W. Schreuder, *Haptic feedback, force feedback, and force-sensing in simulation training for laparoscopy: A systematic overview*, *Journal of surgical education* **76** (2019), no. 1 242–261.

[105] J. Chen, M. Glover, C. Yang, C. Li, Z. Li, and A. Cangelosi, *Development of an immersive interface for robot teleoperation*, in *Annual Conference Towards Autonomous Robotic Systems*, pp. 1–15, Springer, 2017.

[106] D. Prattichizzo, C. Pacchierotti, and G. Rosati, *Cutaneous force feedback as a sensory subtraction technique in haptics*, *IEEE Transactions on Haptics* **5** (2012), no. 4 289–300.

[107] C. Pacchierotti, *Cutaneous haptic feedback in robotic teleoperation*. Springer, 2015.

[108] J. Perret and E. Vander Poorten, *Touching virtual reality: a review of haptic gloves*, in *ACTUATOR 2018; 16th International Conference on New Actuators*, pp. 1–5, VDE, 2018.

[109] X. Gu, Y. Zhang, W. Sun, Y. Bian, D. Zhou, and P. O. Kristensson, *Dexmo: An inexpensive and lightweight mechanical exoskeleton for motion capture and force feedback in vr*, in *Proceedings of the 2016 CHI Conference on Human Factors in Computing Systems*, pp. 1991–1995, 2016.

[110] E. L. Secco and A. M. Tadesse, *A wearable exoskeleton for hand kinesthetic feedback in virtual reality*, in *International Conference on Wireless Mobile Communication and Healthcare*, pp. 186–200, Springer, 2019.

[111] H.-R. Tsai and J. Rekimoto, *Elasticvr: Providing multi-level active and passive force feedback in virtual reality using elasticity*, in *Extended Abstracts of the 2018 CHI Conference on Human Factors in Computing Systems*, pp. 1–4, 2018.

[112] Y. Park, I. Jo, J. Lee, and J. Bae, *A dual-cable hand exoskeleton system for virtual reality*, *Mechatronics* **49** (2018) 177–186.

[113] D. T. G. Le and L. Nguyen, *An efficient force-feedback hand exoskeleton for haptic applications*, *International Journal of Intelligent Robotics and Applications* **5** (2021), no. 3 395–409.

[114] I. Choi, H. Culbertson, M. R. Miller, A. Olwal, and S. Follmer, *Grabity: A wearable haptic interface for simulating weight and grasping in virtual reality*, in *Proceedings of the 30th Annual ACM Symposium on User Interface Software and Technology*, pp. 119–130, 2017.

[115] I. Choi, E. Ofek, H. Benko, M. Sinclair, and C. Holz, *Claw: A multifunctional handheld haptic controller for grasping, touching, and triggering in virtual reality*, in *Proceedings of the 2018 CHI Conference on Human Factors in Computing Systems*, pp. 1–13, 2018.

[116] R. Hinchet, V. Vechev, H. Shea, and O. Hilliges, *Dextres: Wearable haptic feedback for grasping in vr via a thin form-factor electrostatic brake*, in *Proceedings of the 31st Annual ACM Symposium on User Interface Software and Technology*, pp. 901–912, 2018.

[117] C. Fang, Y. Zhang, M. Dworman, and C. Harrison, *Wireality: Enabling complex tangible geometries in virtual reality with worn multi-string haptics*, in *Proceedings of the 2020 CHI Conference on Human Factors in Computing Systems*, pp. 1–10, 2020.

[118] P. Lopes, A. Ion, and P. Baudisch, *Impacto: Simulating physical impact by combining tactile stimulation with electrical muscle stimulation*, in *Proceedings of the 28th Annual ACM Symposium on User Interface Software & Technology*, pp. 11–19, 2015.

[119] P. Lopes, S. You, L.-P. Cheng, S. Marwecki, and P. Baudisch, *Providing haptics to walls & heavy objects in virtual reality by means of electrical muscle stimulation*, in *Proceedings of the 2017 CHI Conference on Human Factors in Computing Systems*, pp. 1471–1482, 2017.

[120] C. Pacchierotti, S. Sinclair, M. Solazzi, A. Frisoli, V. Hayward, and D. Prattichizzo, *Wearable haptic systems for the fingertip and the hand: taxonomy, review, and perspectives*, *IEEE transactions on haptics* **10** (2017), no. 4 580–600.

[121] S. Pabon, E. Sotgiu, R. Leonardi, C. Brancolini, O. Portillo-Rodriguez, A. Frisoli, and M. Bergamasco, *A data-glove with vibro-tactile stimulators for virtual social interaction and rehabilitation*, in *10th Annual Intl Workshop on Presence*, pp. 345–348, 2007.

[122] U. Gollner, T. Bieling, and G. Joost, *Mobile lorm glove: introducing a communication device for deaf-blind people*, in *Proceedings of the sixth international conference on tangible, embedded and embodied interaction*, pp. 127–130, ACM, 2012.

[123] F. Sanfilippo, L. I. Hatledal, and K. Pettersen, *A fully–immersive hapto–audio–visual framework for remote touch*, in *Proc. of the 11th IEEE International Conference on Innovations in Information Technology (IIT'15), Dubai, United Arab Emirates*, 2015.

[124] C.-M. Wu, C.-W. Hsu, T.-K. Lee, and S. Smith, *A virtual reality keyboard with realistic haptic feedback in a fully immersive virtual environment*, *Virtual Reality* **21** (2017), no. 1 19–29.

[125] E. F. Borja, D. A. Lara, W. X. Quevedo, and V. H. Andaluz, *Haptic stimulation glove for fine motor rehabilitation in virtual reality environments*, in *International Conference on Augmented Reality, Virtual Reality and Computer Graphics*, pp. 211–229, Springer, 2018.

[126] E. Pezent, A. Israr, M. Samad, S. Robinson, P. Agarwal, H. Benko, and N. Colonnese, *Tasbi: Multisensory squeeze and vibrotactile wrist haptics for augmented and virtual reality*, in *2019 IEEE World Haptics Conference (WHC)*, pp. 1–6, IEEE, 2019.

[127] J. Hong, L. Stearns, J. Froehlich, D. Ross, and L. Findlater, *Evaluating angular accuracy of wrist-based haptic directional guidance for hand movement.*, in *Graphics Interface*, pp. 195–200, 2016.

[128] J. Hong, A. Pradhan, J. E. Froehlich, and L. Findlater, *Evaluating wrist-based haptic feedback for non-visual target finding and path tracing on a 2d surface*, in *Proceedings of the 19th International ACM SIGACCESS Conference on Computers and Accessibility*, pp. 210–219, 2017.

[129] K. A. Aziz, H. Luo, L. Asma, W. Xu, Y. Zhang, and D. Wang, *Haptic handshank–a handheld multimodal haptic feedback controller for virtual reality*, in *2020 IEEE International Symposium on Mixed and Augmented Reality (ISMAR)*, pp. 239–250, IEEE, 2020.

[130] I. Choi, E. Zhao, E. J. Gonzalez, and S. Follmer, *Augmenting perceived softness of haptic proxy objects through transient vibration and visuo-haptic illusion in virtual reality*, *IEEE Transactions on Visualization and Computer Graphics* (2020).

[131] M. Solazzi, A. Frisoli, and M. Bergamasco, *Design of a novel finger haptic interface for contact and orientation display*, in *2010 IEEE Haptics Symposium*, pp. 129–132, IEEE, 2010.

[132] C. Pacchierotti, A. Tirmizi, and D. Prattichizzo, *Improving transparency in teleoperation by means of cutaneous tactile force feedback*, *ACM Transactions on Applied Perception (TAP)* **11** (2014), no. 1 1–16.

[133] H. Benko, C. Holz, M. Sinclair, and E. Ofek, *Normaltouch and texturetouch: High-fidelity 3d haptic shape rendering on handheld virtual reality controllers*, in *Proceedings of the 29th Annual Symposium on User Interface Software and Technology*, pp. 717–728, 2016.

[134] S.-Y. Teng, P. Li, R. Nith, J. Fonseca, and P. Lopes, *Touch&fold: A foldable haptic actuator for rendering touch in mixed reality*, in *Proceedings of the 2021 CHI Conference on Human Factors in Computing Systems*, pp. 1–14, 2021.

[135] S.-C. Kim, C.-H. Kim, G.-H. Yang, T.-H. Yang, B.-K. Han, S.-C. Kang, and D.-S. Kwon, *Small and lightweight tactile display (salt) and its application*, in *World Haptics 2009-Third Joint EuroHaptics conference and Symposium on Haptic Interfaces for Virtual Environment and Teleoperator Systems*, pp. 69–74, IEEE, 2009.

[136] V. Vechev, J. Zarate, D. Lindlbauer, R. Hinchet, H. Shea, and O. Hilliges, *Tactiles: Dual-mode low-power electromagnetic actuators for rendering continuous contact and spatial haptic patterns in vr*, in *2019 IEEE Conference on Virtual Reality and 3D User Interfaces (VR)*, pp. 312–320, IEEE, 2019.

[137] S. Yoshida, Y. Sun, and H. Kuzuoka, *Pocopo: Handheld pin-based shape display for haptic rendering in virtual reality*, in *Proceedings of the 2020 CHI Conference on Human Factors in Computing Systems*, pp. 1–13, 2020.

[138] B. T. Gleeson, S. K. Horschel, and W. R. Provancher, *Design of a fingertip-mounted tactile display with tangential skin displacement feedback*, *IEEE Transactions on Haptics* **3** (2010), no. 4 297–301.

[139] M. Solazzi, W. R. Provancher, A. Frisoli, and M. Bergamasco, *Design of a sma actuated 2-dof tactile device for displaying tangential skin displacement*, in *2011 IEEE World Haptics Conference*, pp. 31–36, IEEE, 2011.

[140] A. Girard, M. Marchal, F. Gosselin, A. Chabrier, F. Louveau, and A. Lécuyer, *Haptip: Displaying haptic shear forces at the fingertips for multi-finger interaction in virtual environments*, *Frontiers in ICT* **3** (2016) 6.

[141] E. Whitmire, H. Benko, C. Holz, E. Ofek, and M. Sinclair, *Haptic revolver: Touch, shear, texture, and shape rendering on a reconfigurable virtual reality controller*, in *Proceedings of the 2018 CHI Conference on Human Factors in Computing Systems*, pp. 1–12, 2018.

[142] M. Zhu, A. H. Memar, A. Gupta, M. Samad, P. Agarwal, Y. Visell, S. J. Keller, and N. Colonnese, *Pneusleeve: In-fabric multimodal actuation and sensing in a soft, compact, and expressive haptic sleeve*, in *Proceedings of the 2020 CHI Conference on Human Factors in Computing Systems*, pp. 1–12, 2020.

[143] D. Pamungkas and K. Ward, *Electro-tactile feedback system to enhance virtual reality experience*, *International Journal of Computer Theory and Engineering* **8** (2016), no. 6.

[144] J. Hummel, J. Dodiya, G. A. Center, L. Eckardt, R. Wolff, A. Gerndt, and T. W. Kuhlen, *A lightweight electrotactile feedback device for grasp improvement in immersive virtual environments*, in *2016 IEEE Virtual Reality (VR)*, pp. 39–48, IEEE, 2016.

[145] S. Vizcay, P. Kourtesis, F. Argelaguet, C. Pacchierotti, and M. Marchal, *Electrotactile feedback for enhancing contact information in virtual reality*, in *ICAT-EGVE 2021-International Conference on Artificial Reality and Telexistence and Eurographics Symposium on Virtual Environments*, 2021.

[146] Y. Shi, F. Wang, J. Tian, S. Li, E. Fu, J. Nie, R. Lei, Y. Ding, X. Chen, and Z. L. Wang, *Self-powered electro-tactile system for virtual tactile experiences*, *Science Advances* **7** (2021), no. 6 eabe2943.

[147] S. Scheggi, L. Meli, C. Pacchierotti, and D. Prattichizzo, *Touch the virtual reality: Using the leap motion controller for hand tracking and wearable tactile devices for immersive haptic rendering*, in *ACM SIGGRAPH 2015 Posters*, SIGGRAPH '15, (New York, NY, USA), Association for Computing Machinery, 2015.

[148] F. Argelaguet, L. Hoyet, M. Trico, and A. Lécuyer, *The role of interaction in virtual embodiment: Effects of the virtual hand representation*, in *Virtual Reality (VR), 2016 IEEE*, pp. 3–10, IEEE, 2016.

[149] A. Aristidou, *Hand tracking with physiological constraints*, *The Visual Computer* **34** (2018), no. 2 213–228.

[150] C. Mizera, T. Delrieu, V. Weistroffer, C. Andriot, A. Decatoire, and J.-P. Gazeau, *Evaluation of hand-tracking systems in teleoperation and virtual dexterous manipulation*, *IEEE Sensors Journal* **20** (2019), no. 3 1642–1655.

[151] "Cyberglove systems." https://www.sensoryx.com/products/vrfree/. Online; accessed 31-October-2021.

[152] A. F. Da Silva, A. F. Gonçalves, P. M. Mendes, and J. H. Correia, *Fbg sensing glove for monitoring hand posture*, *IEEE Sensors Journal* **11** (2011), no. 10 2442–2448.

[153] A. H. Moreira, S. Queirós, J. Fonseca, P. L. Rodrigues, N. F. Rodrigues, and J. L. Vilaça, *Real-time hand tracking for rehabilitation and character animation*, in *2014 IEEE 3nd International Conference on Serious Games and Applications for Health (SeGAH)*, pp. 1–8, IEEE, 2014.

[154] "Vrfree gloves." http://www.cyberglovesystems.com/cyberglove-iii. Online; accessed 31-October-2021.

[155] R. Y. Wang and J. Popović, *Real-time hand-tracking with a color glove*, *ACM transactions on graphics (TOG)* **28** (2009), no. 3 1–8.

[156] Z. Pan, Y. Li, M. Zhang, C. Sun, K. Guo, X. Tang, and S. Z. Zhou, *A real-time multi-cue hand tracking algorithm based on computer vision*, in *2010 IEEE Virtual Reality Conference (VR)*, pp. 219–222, Ieee, 2010.

[157] S. Han, B. Liu, R. Cabezas, C. D. Twigg, P. Zhang, J. Petkau, T.-H. Yu, C.-J. Tai, M. Akbay, Z. Wang, *et. al.*, *Megatrack: monochrome egocentric articulated hand-tracking for virtual reality*, *ACM Transactions on Graphics (TOG)* **39** (2020), no. 4 87–1.

[158] "Leap motion controller." https://www.ultraleap.com/product/leap-motion-controller/. Online; accessed 31-October-2021.

[159] "Oculus quest hand tracking." `https://www.oculus.com/blog/how-researchers-cracked-hand-tracking-technology-on-quest/`. Online; accessed 31-October-2021.

[160] A. Maravita, C. Spence, and J. Driver, *Multisensory integration and the body schema: close to hand and within reach*, *Current biology* **13** (2003), no. 13 R531–R539.

[161] C. Blanchard, R. Roll, J.-P. Roll, and A. Kavounoudias, *Differential contributions of vision, touch and muscle proprioception to the coding of hand movements*, *PLoS One* **8** (2013), no. 4 e62475.

[162] R. J. van Beers, A. C. Sittig, and J. J. D. van Der Gon, *Integration of proprioceptive and visual position-information: An experimentally supported model*, *Journal of neurophysiology* **81** (1999), no. 3 1355–1364.

[163] L. E. Brown, M. C. Marlin, and S. Morrow, *On the contributions of vision and proprioception to the representation of hand-near targets*, *Journal of neurophysiology* **113** (2015), no. 2 409–419.

[164] R. Van Beers, A. C. Sittig, and J. J. D. van der Gon, *The precision of proprioceptive position sense*, *Experimental Brain Research* **122** (1998), no. 4 367–377.

[165] L. Rincon-Gonzalez, C. A. Buneo, and S. I. H. Tillery, *The proprioceptive map of the arm is systematic and stable, but idiosyncratic*, *PloS one* **6** (2011), no. 11 e25214.

[166] A. Crowe, W. Keessen, W. Kuus, R. Van Vliet, and A. Zegeling, *Proprioceptive accuracy in two dimensions*, *Perceptual and motor skills* **64** (1987), no. 3 831–846.

[167] I. A. Kuling, M. C. van der Graaff, E. Brenner, and J. B. Smeets, *Proprioceptive biases in different experimental designs*, in *International Conference on Human Haptic Sensing and Touch Enabled Computer Applications*, pp. 18–24, Springer, 2014.

[168] Y. Laufer, S. Hocherman, and R. Dickstein, *Accuracy of reproducing hand position when using active compared with passive movement*, *Physiotherapy Research International* **6** (2001), no. 2 65–75.

[169] I. A. Kuling, E. Brenner, and J. B. J. Smeets, *Proprioceptive localization of the hand changes when skin stretch around the elbow is manipulated*, *Frontiers in Psychology* **7** (2016) 1620.

[170] S. Mueller and K. Fiehler, *Mixed body-and gaze-centered coding of proprioceptive reach targets after effector movement*, *Neuropsychologia* **87** (2016) 63–73.

[171] I. A. Kuling, E. Brenner, and J. B. Smeets, *Errors in visuo-haptic and haptic-haptic location matching are stable over long periods of time*, *Acta psychologica* **166** (2016) 31–36.

[172] S. A. Jones, E. K. Cressman, and D. Y. Henriques, *Proprioceptive localization of the left and right hands*, *Experimental brain research* **204** (2010), no. 3 373–383.

[173] I. A. Kuling, M. C. van der Graaff, E. Brenner, and J. B. Smeets, *Matching locations is not just matching sensory representations*, *Experimental brain research* **235** (2017), no. 2 533–545.

[174] S. J. Sober and P. N. Sabes, *Multisensory integration during motor planning*, *Journal of Neuroscience* **23** (2003), no. 18 6982–6992.

[175] M. S. Graziano, *Where is my arm? the relative role of vision and proprioception in the neuronal representation of limb position*, *Proceedings of the National Academy of Sciences* **96** (1999), no. 18 10418–10421.

[176] C. Ghez, J. Gordon, M. G. Felice, and R. Sainburg, *Contributions of vision and proprioception to accuracy in limb movements*, in *The Cognitive Neurosciences* (M. S. Gazzaniga, ed.), ch. 35, pp. 549—-564. Massachusetts Institute of Technology, Boston, Mass, 1995.

[177] J. T. Shenton, J. Schwoebel, and H. B. Coslett, *Mental motor imagery and the body schema: evidence for proprioceptive dominance*, *Neuroscience letters* **370** (2004), no. 1 19–24.

[178] S. Monaco, G. Króliczak, D. J. Quinlan, P. Fattori, C. Galletti, M. A. Goodale, and J. C. Culham, *Contribution of visual and proprioceptive information to the precision of reaching movements*, *Experimental brain research* **202** (2010), no. 1 15–32.

[179] M. Kammers, F. de Vignemont, L. Verhagen, and H. C. Dijkerman, *The rubber hand illusion in action*, *Neuropsychologia* **47** (2009), no. 1 204–211.

[180] M. Tsakiris and P. Haggard, *The rubber hand illusion revisited: visuotactile integration and self-attribution.*, *Journal of Experimental Psychology: Human Perception and Performance* **31** (2005), no. 1 80.

[181] J. Soechting and M. Flanders, *Moving in three-dimensional space: frames of reference, vectors, and coordinate systems*, *Annual review of neuroscience* **15** (1992), no. 1 167–191.

[182] C. Armbrüster, M. Wolter, T. Kuhlen, W. Spijkers, and B. Fimm, *Depth perception in virtual reality: distance estimations in peri-and extrapersonal space*, *Cyberpsychology & Behavior* **11** (2008), no. 1 9–15.

[183] E. K. Cressman and D. Y. Henriques, *Sensory recalibration of hand position following visuomotor adaptation*, *Journal of neurophysiology* **102** (2009), no. 6 3505–3518.

[184] E. K. Cressman and D. Y. Henriques, *Reach adaptation and proprioceptive recalibration following exposure to misaligned sensory input*, *Journal of neurophysiology* **103** (2010), no. 4 1888–1895.

[185] M. Tagliabue and J. McIntyre, *A modular theory of multisensory integration for motor control*, *Frontiers in computational neuroscience* **8** (2014) 1.

[186] M. R. Longo and P. Haggard, *An implicit body representation underlying human position sense*, *Proceedings of the National Academy of Sciences* **107** (2010), no. 26 11727–11732.

[187] T. J. Moore, *A survey of the mechanical characteristics of skin and tissue in response to vibratory stimulation*, *IEEE Transactions on Man-Machine Systems* **11** (1970), no. 1 79–84.

[188] R. S. Johansson and Å. B. Vallbo, *Tactile sensory coding in the glabrous skin of the human hand*, *Trends in neurosciences* **6** (1983) 27–32.

[189] K. O. Johnson, *The roles and functions of cutaneous mechanoreceptors*, *Current Opinion in Neurobiology* **11** (2001), no. 4 455 – 461.

[190] L. R. Manfredi, H. P. Saal, K. J. Brown, M. C. Zielinski, J. F. Dammann, V. S. Polashock, and S. J. Bensmaia, *Natural scenes in tactile texture*, *J. Neurophysiol.* **111** (2014), no. 9 1792–1802.

[191] B. Delhaye, V. Hayward, P. Lefèvre, and J.-L. Thonnard, *Texture-induced vibrations in the forearm during tactile exploration*, *Frontiers in behavioral neuroscience* **6** (2012).

[192] Y. Visell and Y. Shao, *Learning constituent parts of touch stimuli from whole hand vibrations*, in *Proc. IEEE Haptics Symposium*, pp. 253–258, IEEE, 2016.

[193] C. Fradet, L. R. Manfredi, S. Bensmaia, and V. Hayward, *Fingertip skin as a linear medium for wave propagation*, in *Proc. IEEE World Haptics Conf.*, pp. 507–510, IEEE, 2017.

[194] X. S. Xu, D. E. Welcome, T. W. McDowell, J. Z. Wu, B. Wimer, C. Warren, and R. G. Dong, *The vibration transmissibility and driving-point biodynamic response of the hand exposed to vibration normal to the palm*, *International Journal of Industrial Ergonomics* **41** (2011), no. 5 418–427.

[195] H. Schäfer, Z. Wells, Y. Shao, and Y. Visell, *Transfer properties of touch elicited waves: Effect of posture and contact conditions*, in *Proc. IEEE World Haptics Conf.*, pp. 546–551, IEEE, 2017.

[196] T. Iwamoto and H. Shinoda, *Finger ring tactile interface based on propagating elastic waves on human fingers*, in *Proceedings of the Second Joint EuroHaptics Conference and Symposium on Haptic Interfaces for Virtual Environment and Teleoperator Systems*, pp. 145–150, IEEE Computer Society, 2007.

[197] T. Hachisu and K. Suzuki, *Tactile apparent motion through human-human physical touch*, in *International Conference on Human Haptic Sensing and Touch Enabled Computer Applications*, pp. 163–174, Springer, 2018.

[198] Y. Kim, J. Cha, J. Ryu, and I. Oakley, *A tactile glove design and authoring system for immersive multimedia*, *IEEE MultiMedia* **17** (2010), no. 3 34–45.

[199] J. Seo and S. Choi, *Perceptual analysis of vibrotactile flows on a mobile device*, *IEEE transactions on haptics* **6** (2013), no. 4 522–527.

[200] A. Marquardt, J. Maiero, E. Kruijff, C. Trepkowski, A. Schwandt, A. Hinkenjann, J. Schöning, and W. Stuerzlinger, *Tactile hand motion and pose guidance for 3d interaction*, in *Proceedings of the 24th ACM Symposium on Virtual Reality Software and Technology*, p. 3, ACM, 2018.

[201] S. Je, M. Lee, Y. Kim, L. Chan, X.-D. Yang, and A. Bianchi, *Pokering: Notifications by poking around the finger*, in *Proceedings of the 2018 CHI Conference on Human Factors in Computing Systems*, p. 542, ACM, 2018.

[202] H. E. Burtt, *Tactual illusions of movement.*, *Journal of Experimental Psychology* **2** (1917), no. 5 371.

[203] A. K. Whitchurch, *The illusory perception of movement on the skin*, *Am. J. of Psychology* **32** (1921), no. 4 472–489.

[204] C. E. Sherrick and R. Rogers, *Apparent haptic movement*, *Perception & Psychophysics* **1** (1966), no. 3 175–180.

[205] J. Seo and S. Choi, *Initial study for creating linearly moving vibrotactile sensation on mobile device*, in *2010 IEEE Haptics Symposium*, pp. 67–70, IEEE, 2010.

[206] O. S. Schneider, A. Israr, and K. E. MacLean, *Tactile animation by direct manipulation of grid displays*, in *Proceedings of the 28th Annual ACM Symposium on User Interface Software & Technology*, pp. 21–30, ACM, 2015.

[207] D. Pittera, M. Obrist, and A. Israr, *Hand-to-hand: an intermanual illusion of movement*, in *Proceedings of the 19th ACM International Conference on Multimodal Interaction*, pp. 73–81, ACM, 2017.

[208] G. Von Békésy, *Experiments in hearing*. McGraw-Hill, 1960.

[209] R. D. Blandford and K. S. Thorne, *Applications of Classical Physics*. California Institute of Technology, 2003.

[210] H. Azhari, *Basics of biomedical ultrasound for engineers*. John Wiley & Sons, 2010.

[211] J. Achenbach, *Wave propagation in elastic solids*. Elsevier, 2012.

[212] J. Pereira, J. Mansour, and B. Davis, *Dynamic measurement of the viscoelastic properties of skin*, *Journal of biomechanics* **24** (1991), no. 2 157–162.

[213] R. T. Verrillo, *Psychophysics of vibrotactile stimulation*, *The Journal of the Acoustical Society of America* **77** (1985), no. 1 225–232.

[214] G. A. Gescheider, S. Bolanowski Jr, and R. T. Verrillo, *Vibrotactile masking: Effects of stimulus onset asynchrony and stimulus frequency*, *The Journal of the Acoustical Society of America* **85** (1989), no. 5 2059–2064.

[215] M. Enriquez and K. E. MacLean, *Backward and common-onset masking of vibrotactile stimuli*, *Brain research bulletin* **75** (2008), no. 6 761–769.

[216] J. M. Yau, J. B. Olenczak, J. F. Dammann, and S. J. Bensmaia, *Temporal frequency channels are linked across audition and touch*, *Current biology* **19** (2009), no. 7 561–566.

[217] F. Sorgini, R. Caliò, M. C. Carrozza, and C. M. Oddo, *Haptic-assistive technologies for audition and vision sensory disabilities*, *Disability and Rehabilitation: Assistive Technology* **13** (2018), no. 4 394–421.

[218] S. Biswas and Y. Visell, *Emerging material technologies for haptics*, *Advanced Materials Technologies* **4** (2019), no. 4 1900042.

[219] S. Biswas and Y. Visell, *Haptic perception, mechanics, and material technologies for virtual reality*, *Advanced Functional Materials* (2021) 2008186.

[220] D. W. Weir, M. A. Peshkin, J. E. Colgate, and P. Buttolo, *Design and performance of a high fidelity, low mass, linear haptic display*, in *First Joint Eurohaptics Conference and Symposium on Haptic Interfaces for Virtual Environment and Teleoperator Systems. World Haptics Conference*, pp. 177–182, IEEE, 2005.

[221] W. McMahan and K. J. Kuchenbecker, *Dynamic modeling and control of voice-coil actuators for high-fidelity display of haptic vibrations*, in *2014 IEEE Haptics Symposium (HAPTICS)*, pp. 115–122, IEEE, 2014.

[222] G. Korres and M. Eid, *Design of low-profile tactile actuator with rich vibrotactile stimulation for wearable applications*, in *2019 IEEE International Symposium on Haptic, Audio and Visual Environments and Games (HAVE)*, pp. 1–6, IEEE, 2019.

[223] P. Preechayasomboon, A. Israr, and M. Samad, *Chasm: A screw based expressive compact haptic actuator*, in *Proceedings of the 2020 CHI Conference on Human Factors in Computing Systems*, pp. 1–13, 2020.

[224] H.-Y. Yao and V. Hayward, *Design and analysis of a recoil-type vibrotactile transducer*, *The Journal of the Acoustical Society of America* **128** (2010), no. 2 619–627.

[225] V. Hayward and K. E. MacLean, *Do it yourself haptics: part i*, *IEEE Robotics & Automation Magazine* **14** (2007), no. 4 88–104.

[226] J. J. Zárate and H. Shea, *Using pot-magnets to enable stable and scalable electromagnetic tactile displays*, *IEEE transactions on haptics* **10** (2016), no. 1 106–112.

[227] F. Pece, J. J. Zarate, V. Vechev, N. Besse, O. Gudozhnik, H. Shea, and O. Hilliges, *Magtics: Flexible and thin form factor magnetic actuators for dynamic and wearable haptic feedback*, in *Proceedings of the 30th annual ACM symposium on User interface software and technology*, pp. 143–154, 2017.

[228] H. Boys, G. Frediani, S. Poslad, J. Busfield, and F. Carpi, *A dielectric elastomer actuator-based tactile display for multiple fingertip interaction with virtual soft bodies*, in *Electroactive Polymer Actuators and Devices (EAPAD) 2017*, vol. 10163, p. 101632D, International Society for Optics and Photonics, 2017.

[229] J.-H. Youn, H. Mun, and K.-U. Kyung, *A wearable soft tactile actuator with high output force for fingertip interaction*, *IEEE Access* **9** (2021) 30206–30215.

[230] P. Strohmeier and K. Hornbæk, *Generating haptic textures with a vibrotactile actuator*, in *Proceedings of the 2017 CHI Conference on Human Factors in Computing Systems*, pp. 4994–5005, 2017.

[231] A. Israr, S. Zhao, K. Schwalje, R. Klatzky, and J. Lehman, *Feel effects: enriching storytelling with haptic feedback*, *ACM Transactions on Applied Perception (TAP)* **11** (2014), no. 3 1–17.

[232] S. A. Macdonald, S. Brewster, and F. Pollick, *Eliciting emotion with vibrotactile stimuli evocative of real-world sensations*, in *Proceedings of the 2020 International Conference on Multimodal Interaction*, pp. 125–133, 2020.

[233] A. Kawazoe, G. Reardon, E. Woo, M. Di Luca, and Y. Visell, *Tactile echoes: Multisensory augmented reality for the hand*, *IEEE Transactions on Haptics* (2021).

[234] A. Ghosh and B. Corves, *Introduction to micromechanisms and microactuators*. Springer, 2015.

[235] K. Raj and R. Moskowitz, *Commercial applications of ferrofluids*, *Journal of Magnetism and Magnetic Materials* **85** (1990), no. 1-3 233–245.

[236] R. E. Rosensweig, Y. Hirota, S. Tsuda, and K. Raj, *Study of audio speakers containing ferrofluid*, *Journal of Physics: Condensed Matter* **20** (2008), no. 20 204147.

[237] L. Vaidman, *Torque and force on a magnetic dipole*, *American Journal of Physics* **58** (1990), no. 10 978–983.

[238] J. J. Zárate, G. Tosolini, S. Petroni, M. De Vittorio, and H. Shea, *Optimization of the force and power consumption of a microfabricated magnetic actuator*, *Sensors and Actuators A: Physical* **234** (2015) 57–64.

[239] D. Vokoun, M. Beleggia, L. Heller, and P. Šittner, *Magnetostatic interactions and forces between cylindrical permanent magnets*, *Journal of magnetism and Magnetic Materials* **321** (2009), no. 22 3758–3763.

[240] M. Kwon, J. Jung, T. Jang, and S. Sohn, *Magnetic forces between a magnet and a solenoid*, *The Physics Teacher* **58** (2020), no. 5 330–334.

[241] D. Giovanni, *Flat and corrugated diaphragm design handbook*. Routledge, 2017.

[242] Y. Visell and J. R. Cooperstock, *Design of a vibrotactile display via a rigid surface*, in *2010 IEEE haptics symposium*, pp. 133–140, IEEE, 2010.

[243] A. Zeaiter, M. Fénot, and D. Saury, *Numerical approach to determining windings' thermal conductivity*, in *2018 XIII International Conference on Electrical Machines (ICEM)*, pp. 1291–1296, 2018.

[244] W. Zhao, X. Wang, S. Wu, S. Cui, C. Gerada, and H. Yan, *Eddy current losses analysis and optimization design of litz-wire windings for air-core compulsators*, *IEEE Transactions on Plasma Science* **47** (2019), no. 5 2532–2538.

[245] *Permalloy 80 Technical Data*, 1999.

[246] *Carpenter HyMu 80 Data-sheet*, 2015.

[247] *NdFeB Magnets/Neodymium Iron Boron Magnets Data-sheet*, 2021.

[248] *Sintered Neodymium-Iron-Boron Magnets Data-sheet*, 2017.

[249] *Thermally Conductive Epoxy Encapsulating and Potting Compound 832TC Technical Data Sheet*, 2016.

[250] *Duralco Thermally Conductive Epoxy Data-sheet*, 2021.

[251] *Thermal Properties of Plastic Materials*, 2021.

[252] M. Higano, A. Miyagawa, K. Saigou, H. Masuda, and H. Miyashita, *Measuring the specific heat capacity of magnetic fluids using a differential scanning calorimeter*, *International Journal of Thermophysics* **20** (1999), no. 1 207–215.

[253] M. Goharkhah, S. Gharehkhani, S. Fallah, and M. Ashjaee, *Dynamic measurement of ferrofluid thermal conductivity under an external magnetic fieldr*, *Heat and Mass Transfer* **55** (2019) 1583–1592.

[254] M. Amjadi, Y. J. Yoon, and I. Park, *Ultra-stretchable and skin-mountable strain sensors using carbon nanotubes–ecoflex nanocomposites*, *Nanotechnology* **26** (2015), no. 37 375501.

[255] J. Park, N. Pažin, J. Friedman, V. M. Zatsiorsky, and M. L. Latash, *Mechanical properties of the human hand digits: Age-related differences*, *Clinical Biomechanics* **29** (2014), no. 2 129–137.

[256] D. A. Bowman and R. P. McMahan, *Virtual reality: how much immersion is enough?*, *Computer* **40** (2007), no. 7 36–43.

[257] S. D. Laycock and A. Day, *Recent developments and applications of haptic devices*, in *Computer Graphics Forum*, vol. 22 (2), pp. 117–132, Wiley Online Library, 2003.

[258] W. Guo, Y. Hu, Z. Yin, and H. Wu, *On-skin stimulation devices for haptic feedback and human–machine interfaces*, *Advanced Materials Technologies* (2021) 2100452.

[259] G. B. Rollman, *Electrocutaneous stimulation: Psychometric functions and temporal integration*, *Perception & Psychophysics* **5** (1969), no. 5 289–293.

[260] M. Ying, A. P. Bonifas, N. Lu, Y. Su, R. Li, H. Cheng, A. Ameen, Y. Huang, and J. A. Rogers, *Silicon nanomembranes for fingertip electronics*, *Nanotechnology* **23** (2012), no. 34 344004.

[261] A. Withana, D. Groeger, and J. Steimle, *Tacttoo: A thin and feel-through tattoo for on-skin tactile output*, in *Proceedings of the 31st Annual ACM Symposium on User Interface Software and Technology*, pp. 365–378, 2018.

[262] S. Lim, D. Son, J. Kim, Y. B. Lee, J.-K. Song, S. Choi, D. J. Lee, J. H. Kim, M. Lee, T. Hyeon, *et. al.*, *Transparent and stretchable interactive human machine interface based on patterned graphene heterostructures*, *Advanced Functional Materials* **25** (2015), no. 3 375–383.

[263] M. Franceschi, L. Seminara, S. Dosen, M. Strbac, M. Valle, and D. Farina, *A system for electrotactile feedback using electronic skin and flexible matrix electrodes: experimental evaluation*, *IEEE transactions on haptics* **10** (2016), no. 2 162–172.

[264] M. Isaković, M. Belić, M. Štrbac, I. Popović, S. Došen, D. Farina, and T. Keller, *Electrotactile feedback improves performance and facilitates learning in the routine grasping task*, *European journal of translational myology* **26** (2016), no. 3.

[265] M. Štrbac, M. Belić, M. Isaković, V. Kojić, G. Bijelić, I. Popović, M. Radotić, S. Došen, M. Marković, D. Farina, *et. al.*, *Integrated and flexible multichannel interface for electrotactile stimulation*, *Journal of neural engineering* **13** (2016), no. 4 046014.

[266] P. Bach-y Rita and S. W. Kercel, *Sensory substitution and the human–machine interface*, *Trends in cognitive sciences* **7** (2003), no. 12 541–546.

[267] Y. Alotaibi, J. H. Williamson, and S. Brewster, *Investigating electrotactile feedback on the hand*, in *2020 IEEE Haptics Symposium (HAPTICS)*, pp. 637–642, IEEE, 2020.

[268] H. Kajimoto, N. Kawakami, T. Maeda, and S. Tachi, *Tactile feeling display using functional electrical stimulation*, in *Proc. 1999 ICAT*, p. 133, 1999.

[269] "Iec 60601-2-10:2012." `https://webstore.iec.ch/publication/2617`. Online; accessed 26-October-2021.

[270] B. Geng, K. Yoshida, L. Petrini, and W. Jensen, *Evaluation of sensation evoked by electrocutaneous stimulation on forearm in nondisabled subjects*, *J Rehabil Res Dev* **49** (2012), no. 2 297–308.

[271] M. D'Alonzo, S. Dosen, C. Cipriani, and D. Farina, *Hyve—hybrid vibro-electrotactile stimulation—is an efficient approach to multi-channel sensory feedback*, *IEEE transactions on haptics* **7** (2013), no. 2 181–190.

[272] M. D'Alonzo, S. Dosen, C. Cipriani, and D. Farina, *Hyve: hybrid vibro-electrotactile stimulation for sensory feedback and substitution in rehabilitation*, *IEEE Transactions on Neural Systems and Rehabilitation Engineering* **22** (2013), no. 2 290–301.

[273] A. Akhtar, J. Sombeck, B. Boyce, and T. Bretl, *Controlling sensation intensity for electrotactile stimulation in human-machine interfaces*, *Science robotics* **3** (2018), no. 17.

[274] K. A. Kaczmarek, M. E. Tyler, U. O. Okpara, and S. J. Haase, *Interaction of perceived frequency and intensity in fingertip electrotactile stimulation: dissimilarity ratings and multidimensional scaling*, *IEEE Transactions on Neural Systems and Rehabilitation Engineering* **25** (2017), no. 11 2067–2074.

[275] T. Maeno, K. Kobayashi, and N. Yamazaki, *Relationship between the structure of human finger tissue and the location of tactile receptors*, *JSME International Journal Series C Mechanical Systems, Machine Elements and Manufacturing* **41** (1998), no. 1 94–100.

[276] U. Birgersson, E. Birgersson, I. Nicander, and S. Ollmar, *A methodology for extracting the electrical properties of human skin*, *Physiological measurement* **34** (2013), no. 6 723.

[277] S. Grimnes and O. G. Martinsen, *Bioimpedance and bioelectricity basics*. Academic press, 2011.

[278] S. Biswas, A. Schoeberl, Y. Hao, J. Reiprich, T. Stauden, J. Pezoldt, and H. O. Jacobs, *Integrated multilayer stretchable printed circuit boards paving the way for deformable active matrix*, *Nature communications* **10** (2019), no. 1 1–8.

[279] S. Biswas, Y. Shao, T. Hachisu, T. Nguyen-Dang, and Y. Visell, *Integrated soft optoelectronics for wearable health monitoring*, *Advanced Materials Technologies* **5** (2020), no. 8 2000347.

[280] H. Kajimoto, *Electrotactile display with real-time impedance feedback using pulse width modulation*, *IEEE Transactions on Haptics* **5** (2011), no. 2 184–188.

[281] J. Gregory, S. Tang, Y. Luo, and Y. Shen, *Bio-impedance identification of fingertip skin for enhancement of electro-tactile-based preference*, *International Journal of Intelligent Robotics and Applications* **1** (2017), no. 3 327–341.

[282] Y. Shen, J. Gregory, and C. E. Shelton, *Dynamically characterizing bioimpedance of fingertip skin through a developed cvd based electrotactile rendering system*, in *2011 Annual International Conference of the IEEE Engineering in Medicine and Biology Society*, pp. 2941–2944, IEEE, 2011.

[283] S. Parsnejad, E. Ashoori, and A. J. Mason, *Multi-electrode electrotactile stimulation to combat skin dependency in machine-to-human feedback*, in *2021 IEEE International Midwest Symposium on Circuits and Systems (MWSCAS)*, pp. 626–629, IEEE, 2021.

[284] A. Jayaraman, K. A. Kaczmarek, M. E. Tyler, and U. O. Okpara, *Effect of localized ambient humidity on electrotactile skin resistance*, in *2007 IEEE 33rd Annual Northeast Bioengineering Conference*, pp. 110–111, IEEE, 2007.

[285] K. A. Kaczmarek and J. G. Webster, *Voltage-current characteristics of the electrotactile skin-electrode interface*, in *Images of the Twenty-First Century. Proceedings of the Annual International Engineering in Medicine and Biology Society,*, pp. 1526–1527, IEEE, 1989.

[286] H. Kajimoto, *Design of cylindrical whole-hand haptic interface using electrocutaneous display*, in *International Conference on Human Haptic Sensing and Touch Enabled Computer Applications*, pp. 67–72, Springer, 2012.